Department of Physics and Astronomy
Heidelberg University

Master Thesis in Physics
submitted by

Kevin Lukas Ackermann

born in Mainz (Germany)

2023

Electron Spin Resonance and *Ab-Initio* Multiplet Ligand Field Theory Studies on the Trigonal Trinuclear Complexes $NMe_4[TM_3(\mu_3\text{-}F)(TFA)_6(Py)_3]$ (TM = Co, Cu)

This Master Thesis has been carried out by Kevin Lukas Ackermann
at the
Kirchoff Institute for Physics and the Institute for Theoretical Physics in Heidelberg
under the supervision of
Prof. Dr. Rüdiger Klingeler and Prof. Dr. Maurits W. Haverkort

Electron Spin Resonance and *Ab-Initio* Multiplet Ligand Field Theory Studies on the Trigonal Trinuclear Complexes $NMe_4[TM_3(\mu_3\text{-}F)(TFA)_6(Py)_3]$ (TM = Co, Cu)

This work presents High-field/High-frequency electron spin resonance (HF-ESR) studies of the novel trigonal trinuclear transition metal complexes $NMe_4[Co_3(\mu_3\text{-}F)(TFA)_6(Py)_3]$ (CoΔ) and $NMe_4[Cu_3(\mu_3\text{-}F)(TFA)_6(Py)_3]$ (CuΔ). Additionally density functional theory (DFT) based *ab initio* multiplet ligand-field theory (MLFT) calculations are performed for CuΔ. For CoΔ isothermal magnetization and static susceptibility studies reveal antiferromagnetically coupled spins and a changing ground state at $B_c \approx 8.3\,\mathrm{T}$. Fixed powder HF-ESR measurements show several bend resonance branches arising from transitions, that change their initial states from an exited to the groundstate for an increasing external magnetic fields, supporting the existence of a ground state transition at B_c. Magnetometry data reveal ferromagnetic spin-spin exchange, that is dominated by anisotropic exchange in CuΔ. Complementary X-band ESR measurements show an axial-type anisotropy of the local g-factors. Fitting of a spin-Hamiltonian reveals that the magnitude of the Kitaev-interaction is approximately four times larger than the isotropic exchange. Loose powder HF-ESR studies reveal six resonance branches, of which three exhibit significant downwards bending, showing the signature of anti-level crossings and therefore indicating spin state mixing. DFT calculations yield strong antiferromagnetic coupling for CuΔ, which is to be expected following the standard Goodenough-Kanamori-Anderson rules. However post-DFT MLFT calculations show, that the ferromagnetic exchange is mediated by correlations of the μ_3-bridging fluorine ion. The experimental results could be qualitatively reproduced and strategies for improving quantitative agreement are discussed.

Elektronenspinresonanz und *Ab-Initio* Multiplett-Liganden-Feldtheorie-Untersuchngen an den trigonalen dreikernigen Komplexen $NMe_4[TM_3(\mu_3\text{-}F)(TFA)_6(Py)_3]$ (TM = Co, Cu)

In dieser Arbeit werden Hochfeld-/Hochfrequenz-Elektronenspinresonanz Messungen (HF-ESR) der neuen trigonalen dreikernigen Übergangsmetallkomplexe $NMe_4[Co_3(\mu_3\text{-}F)(TFA)_6(Py)_3]$ (CoΔ) und $NMe_4[Cu_3(\mu_3\text{-}F)(TFA)_6(Py)_3]$ (CuΔ) vorgestellt. Zusätzlich wurden Post-Dichtefunktionaltheorie (DFT) *ab initio* Multiplett-Ligandenfeldtheorie (MLFT) Simulationen für CuΔdurchgeführt. Für CoΔ zeigen isothermische Magnetisierungs- und statische Suszeptibilitätskuven antiferromagnetisch gekoppelte Spins und einen Grundzustandsübergang bei $B_c \approx 8.3\,\mathrm{T}$. HF-ESR Messungen an fixiertem Pulver zeigen mehrere gekrümmte Resonanzzweige, die von übergängen stammen, die ihren Ausgangszustand bei zunehmenden Resonanzfeldern von einem erregten Zustand in den Grundzustand ändern. Dies deutet ebenfalls auf die Existenz eines Grundzustandsübergangs bei B_c hin. Magnetometrische Daten implizieren eine ferromagnetische Spin-Spin-Wechelwirkung, die von anisotropen Wechelswirkungen in CuΔ dominiert wird. Ergänzende X-Band-ESR Messungen zeigen eine axiale Anisotropie der lokalen g-Faktoren. Die Anpassung eines Spin-Hamiltonians zeigt, dass die Stärke der Kitaev-Wechselwirkung etwa viermal so groß ist wie die der isotropen Wecheslwirkung. HF-ESR-Untersuchungen an losem Pulver ergaben sechs Resonanzzweige, von denen drei eine signifikante Abwärtskrümmung aufweisen, die auf Anti-Niveauübergänge und damit auf eine Mischung der Spinzustände hinweisen. DFT-Berechnungen ergeben eine starke antiferromagnetische Kopplung für CuΔ, was auch nach den Standardregeln von Goodenough-Kanamori-Anderson zu erwarten wäre. Post-DFT MLFT-Rechnungen zeigen jedoch, dass die ferromagnetische Kopplung durch Korrelationen auf dem μ_3-überbrückenden Fluor-Ionen vermittelt wird. Die experimentellen Ergebnisse konnten qualitativ reproduziert werden und es werden Strategien zur Verbesserung der quantitativen übereinstimmung diskutiert.

Contents

1 Introduction **1**

2 Experimental Methods **3**

2.1 Magnetometry . . . 3

2.2 High-Field/High-Frequency Electron Spin Resonance . . . 4

2.3 X-Band Electron Spin Resonance . . . 5

3 Numerical and Theoretical Methods **7**

3.1 Spin Hamiltonian Formalism: An Effective Theory . . . 7

3.1.1 Local g-factors and Single-Ion Anisotropy . . . 7

3.1.2 Spin-Spin Exchange Interaction . . . 8

3.1.3 Higher Order Terms . . . 9

3.1.4 Construction of an Effective Spin Hamiltonian . . . 9

3.2 Density-Functional-Theory . . . 11

4 Experimental Results **13**

4.1 Cobalt Triangle: $NMe_4[Co_3(\mu_3\text{-}F)(TFA)_6(Py)_3]$ . . . 13

4.1.1 Structure . . . 13

4.1.2 Static Magnetic Properties . . . 16

4.1.3 High-Field/High-Frequency ESR Studies . . . 20

4.2 Copper Triangle: $NMe_4[Cu_3(\mu_3\text{-}F)(TFA)_6(Py)_3]$ . . . 31

4.2.1 Structure . . . 31

4.2.2 Room Temperature X-Band ESR Studies . . . 33

4.2.3 Static Magnetic Properties . . . 35

4.2.4 High-Field/High-Frequency ESR Studies . . . 41

5 *Ab-Initio* Calculations on $NMe_4[Cu_3(\mu_3\text{-}F)(TFA)_6(Py)_3]$ **51**

5.1 Density-Functional Theory Calculations . . . 52

5.1.1 Choice of Functional and Basis Set . . . 52

5.1.2 Broken-Symmetry DFT 54
5.1.3 DFT of Isolated Copper and Fluorine Atoms 55
5.1.4 Partial Density of States and Molecular Orbitals 56
5.2 From a Mean-Field Hamiltonian to a Ligand-Field Theory Model 59
5.2.1 Reduction of Hilberspace size 59
5.2.2 Calculation of Slater-Integrals for the Coulomb Interaction 61
5.2.3 Coulomb Screening and Charge Transfer Energy 61
5.3 Full Many-Body Calculation of the Low Lying Multiplets 64
5.3.1 Double-Counting and Self-Interaction Correction 65
5.3.2 Influence of Correlations of μ_3−F 66
5.3.3 Influence of the Charge Transfer Energy Δ_{CT} and Hubbard U_{H} 67
5.4 Projection of the Many-Body Results to an Effective Spin Hamiltonian 71
5.4.1 Calculation of Static Magnetic Properties and Resonance-Fields 71
5.4.2 Construction of a Spin-Hamiltonian 75
5.5 Conclusion 79

6 Summary **81**

A Appendix **83**

Chapter 1

Introduction

In everyday life one usually perceives the impact of magnetism in the form of magnetic bulk materials, which contain among others iron, magnetite [1] or the powerful rare-earth magnets, such as Nd_2Fe_4B [2, 3]. Their three dimensional bulk nature makes them ideal for macroscopic technological applications, for example as fridge magnets or in electric motors [4]. However interesting and useful magnetic properties can also occur at lower dimensions, such as magnetic order in the two-dimensional van der Waals crystals $Cr_2Ge_2Te_6$ [5] and $FePS_3$ [6]. In one dimension one deals with spin chains, including $[C_2NH_8]_3[Fe(SO_4)_3]$ [7] and β-$VOSO_4$ [8]. Reducing the dimensionality further, one arrives at effectively zero-dimensional systems, these include the topic of this work: single-molecule magnets (SMMs) [3, 1]. The first SMM to be successfully synthesized, $[Mn_{12}(CH_3COO)_{16}(H_2O)_4O_{12}]\cdot 2CH_3COOH\cdot 4H_2O$ (Mn_{12}-ac), was reported in 1980 by Lis *et al.* [9]. The existence of such manganese dodeca-nuclear acetate complexes was already theorized in 1921 by Weinland and Fischer [9, 3]. The discovery of ferrimagnetism in Mn_{12}-ac and the confirmation of the zero-dimensional magnetic order by ac susceptibility measurements, lead to some excitement, since it is possible to store information in a single molecule [1].

The two compounds investigated in this thesis belong to the class of SMMs containing half-integer spin trinuclear complexes with trigonal symmetry. This class of materials has attracted a diverse range of interest [10]: Among other things they can serve as model systems for biological processes [11], such as trigonal Cu^{2+} complexes resembling the active sites in ascorbate oxidases, catalyzing the reduction of O_2 to H_2O [12, 13]. Additionally trigonal complexes have been shown to exhibit magneto-electric coupling [14, 15, 16], as well as chiral spin ordering [17, 16]. This makes them attractive candidates for technological applications, for example in quantum computing [18]. The most important feature of trinuclear transition metal complexes, with regards to this thesis, is that they are on the one hand complex enough to offer a wide range of interesting physical properties. These include, for example geometric frustration in the case of antiferromagnetically coupled spins [19, 20] or anisotropic exchange, as demonstrated in the present work. On the other hand is the number of magnetically active sites small enough, so that *ab-initio* calculations, including exact diagonalization, are possibly feasible. Their treatment however remains highly non-trivial, due to limitations placed by the system size on the computational cost [21, 10]. This makes such systems a good test-bed for theoretical and numerical approaches for understanding the electronic properties of molecules or solids.

The two compounds investigated in the present work $NMe_4[Co_3(\mu_3\text{-}F)(TFA)_6(Py)_3]$ and $NMe_4[Cu_3(\mu_3\text{-}F)(TFA)_6(Py)_3]$ were both newly synthesized in the research group of *A. Vassiliev* [22, 23]. The two materials will be abbreviated as CoΔ and CuΔ respectively in this thesis. Both complexes contain three transition metal ions each, either Co^{2+} in the case of CoΔ or Cu^{2+} in CuΔ, and exhibit trigonal

symmetry. The transition metal ions are bridged by a central μ_3-bridging fluorine, which is designated as μ_3-F. Magnetic properties of the compounds under investigation were measured using the technique of high-field/high-frequency electron spin resonance (HF-ESR) spectroscopy. HF-ESR relies on the lifting of SU(2)-degeneracies by means of an applied magnetic field and inducing m1-transitions between split states [24], allowing direct probing of a part of the system's eigenstates. This provides information about the interaction between spin and anisotropies of the interactions or in the surrounding crystal fields. Combined with varying the temperature, phenomena such as changing the groundstate as a function of the applied magnetic field can be observed. To elucidate the experimental results phenomenological spin-Hamiltonian models are employed alongside *ab-initio* calculations (for CuΔ). The *ab-initio* method applied in the present work is the so called multiplet ligand-field theory (MLFT) approach [25]. The MLFT is based on a mean-field Hamiltonian, which is obtained through density functional theory (DFT). Said Hamiltonian is extended to a true many-body calculation by explicitly including Coulomb repulsion on relevant orbitals, such as open-shell 3d orbitals. This allows for reducing the required Hilbert space substantially. Combined with the one-shot nature of MLFT this can lead to a significant reduction of computational cost [25].

Following this first introductory chapter, the second chapter gives a short introduction of the employed measurement techniques, such as high-field/high-frequency electron spin resonance. In the third chapter theoretical concepts and methods, that are important for understanding of the *ab-initio* calculations, are explained. The fourth chapter presents the experimental results obtained for the two compounds under investigation in this thesis and is therefore split between sections on CoΔ and CuΔ. Additionally basic spin-Hamiltonian modeling is performed on the experimental magnetometry data. The fifth chapter gives a step-by-step description of the multiplet ligand-field theory (MLFT) method employed as a *ab-initio* method to understand the magnetic properties measured in chapter four. A MLFT model is explicitly constructed for CuΔ and the results are discussed. Finally a summary of this work's findings is provided in the sixth chapter.

Chapter 2

Experimental Methods

2.1 Magnetometry

Measurements of the static magnetic properties were performed using two distinct devices: a *Magnetic Properties Measurement System* (MPMS3) and a *Physical Properties Measurement System* (PPMS) both from *Quantum Design*. The MPMS3 supports magnetic fields of up to 7 T and DC and VSM modes for measuring. The PPMS only supports the VSM option, but fields of up to 14 T. The magnetic moment is measured by means of an induced voltage in the device's pickup coils. In DC mode this is realized by moving the sample along a large scan range. The sample is vibrated in the VSM mode which induce the signal in the pick-up coil geometry. Another difference between the two devices is their method of reading out the induced signal: While the PPMS reads out the induced voltage directly, the MPMS employs a SQUID[1] for detection to which the induced flux is transferred.

For preparation the powdered sample was inserted into a cylindrical PPE[2] sample holder and fixed by mechanical pressure. This is achieved by tightly closing the two halfs of the sample holder. To determine the mass of the sample, the empty and full capsule was weighed. This process was performed in a glove-box under an argon atmosphere to prevent degradation of the sample by exposure to air. A prepared CuΔ powder sample can be seen in figure 2.1. The sample-containing PPE capsule is then attached to a brass holder and mounted to the sample rod.

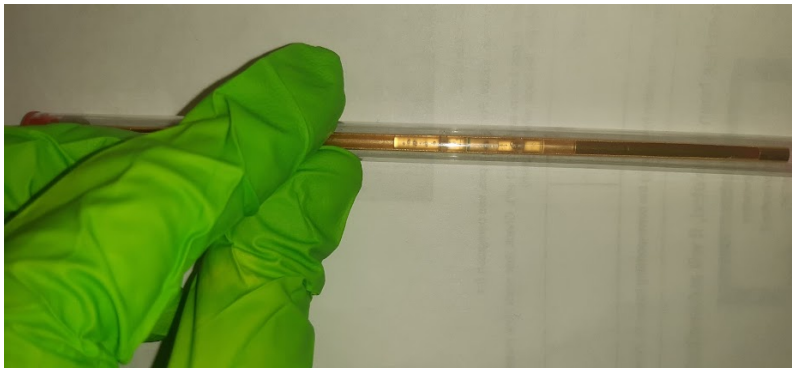


Figure 2.1: A prepared powder sample of (CuΔ) (for measurements in the PPMS) with a mass of $m \approx 1.1$mg. The brass holder is contained in an additional sealed glass tube to prevent exposure to air.

[1] Superconducting Quantum Interference Device
[2] Poly(p-phenylene ether)

To correct the measured magnetization for putative background effects, the experimentally determined contribution of the empty sample holder (PPE and brass holder) is subtracted. For later fitting of models the inherent diamagnetic susceptibility associated to the paired electrons is subtracted as well. This diamagnetic contribution is estimated using the Pascal's constants listen in reference [26]. For CuΔ and CoΔ this yields

$$\begin{aligned}\chi_{\mathrm{D}}(\mathrm{Cu}\Delta) &= \chi_{\mathrm{D}}(\mathrm{F}^-) + 3\chi_{\mathrm{D}}(\mathrm{Py}) + 6\chi_D(\mathrm{TFA}) + \chi_D(\mathrm{NMe_4}) + 3\chi_{\mathrm{D}}(\mathrm{Cu}^{2+}) \\ &= -496.08 \cdot 10^{-6}\mathrm{emu/mol}\,, \qquad (2.1)\\ \chi_{\mathrm{D}}(\mathrm{Co}\Delta) &= \chi_{\mathrm{D}}(\mathrm{F}^-) + 3\chi_{\mathrm{D}}(\mathrm{Py}) + 6\chi_D(\mathrm{TFA}) + \chi_{\mathrm{D}}(\mathrm{NMe_4}) + 3\chi_D(\mathrm{Co}^{2+}) \\ &= -499.08 \cdot 10^{-6}\mathrm{emu/mol}\,, \qquad (2.2)\end{aligned}$$

with χ_{D} being the diamagnetic contribution of the atoms/groups. $\chi_{\mathrm{D}}(\mathrm{TFA})$ and $\chi_{\mathrm{D}}(\mathrm{NMe_4})$ are given by

$$\begin{aligned}\chi_{\mathrm{D}}(\mathrm{TFA}) &= \chi_{\mathrm{D}}(\mathrm{CF_3OOH}) - \chi_{\mathrm{D}}(\mathrm{H}) - \lambda(\mathrm{OH}) = -40.37 \cdot 10^{-6}\mathrm{emu/mol}\,, \qquad (2.3)\\ \chi_{\mathrm{D}}(\mathrm{NMe_4}) &= \chi_{\mathrm{D}}(\mathrm{N}) + 4\chi_{\mathrm{D}}(\mathrm{C}) + 12\chi_{\mathrm{D}}(\mathrm{H}) + 12\lambda(\mathrm{OH}) = -64.76 \cdot 10^{-6}\mathrm{emu/mol}\,, \qquad (2.4)\end{aligned}$$

where λ denotes the contribution of certain bonds. The corrected magnetization M_{corr} and susceptibility χ_{corr} are given by

$$\begin{aligned}M_{\mathrm{corr}}(B) &= M_{\mathrm{measured}}(B) - \mu_0\chi_{\mathrm{D}}B - M_{\text{empty sample holder}}(B)\,, \qquad (2.5)\\ \chi_{\mathrm{corr}}(T) &= \chi_{\mathrm{measured}}(T) - \chi_{\mathrm{D}} - \chi_{\text{empty sample holder}}(T)\,. \qquad (2.6)\end{aligned}$$

2.2 High-Field/High-Frequency Electron Spin Resonance

High-frequency/high-field electron spin resonance measurements were performed using a home-build spectrometer as described, for example in sections 3.1 of [27] and [28]. The typically used field-sweep rate is $\dot{B} = \pm 1\,\mathrm{T/min}$ sweeping up to $B = 16\,\mathrm{T}$. The Lock-In-Amplifier is capable of simultaneously measuring the amplitude and phase-shift of the transmitted microwave signal, allowing for phase corrections to be applied to the measured absorption spectra. This is needed, because the received signal possibly contains contributions from of absorption and dispersion [29]. For correction the measured phase ϕ_{m} is scaled by a factor c and added to the measured spectrum A_{m} to calculate the pure absorption spectrum A_{corr} [30]:

$$A_{\mathrm{corr}} = A_{\mathrm{m}} + \mathrm{c} \cdot \phi_{\mathrm{m}}\,. \qquad (2.7)$$

The scaling factor c is chosen by hand in such a fashion, that the resulting resonance features exhibit a flat baseline and lorentzian line shape as closely as possible. An example of this can be seen in figure 2.2, where phase mixing around the features at $B_1 \approx 5.25\,\mathrm{T}$ and $B_2 \approx 8.43\,\mathrm{T}$ (fig. 2.2(a)) can be observed in the measured amplitude. Equation 2.7 is then applied for several values of c (fig. 2.2(b)). In the end $\mathrm{c} = 0.11$ is chosen, due to the horizontal baseline created by this value for the first and largest feature.

There are two distinct variants of the sample preparation used in this thesis. The sample was either ground to a fine powder before being loosely inserted into a PEEK[3]-container or fixed in said PEEK container using high vacuum grease. The first method was used for measurements on loose powder while the second variant was used to prepare measurements on fixed powder. The difference between these two modes is that using fixed powder only solid angle averaged spectra can be recorded, while loose powder allows for the reduction of examined spatial directions. The PEEK-container is then sealed air-tight with the assistance of Teflon tape (figure 2.3). This entire process was performed in a glove-box under argon atmosphere. The sample installation process is described in section 3.1 of [27] as well.

[3]Polyether ether ketone

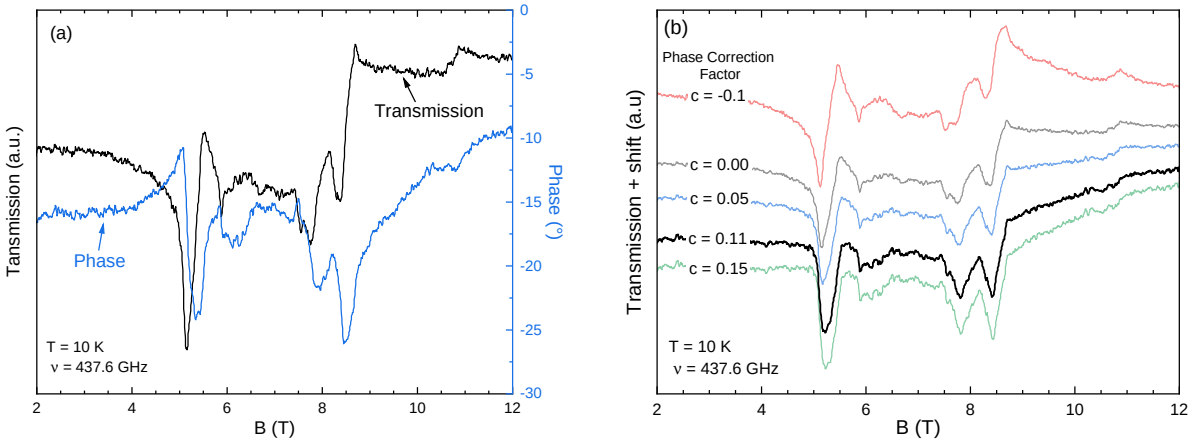


Figure 2.2: Example of how phase correction is applied for a exemplary spectrum of CoΔ at $T = 10\,\mathrm{K}$ and a microwave frequency of $\nu = 437.6\,\mathrm{GHz}$: (a) uncorrected amplitude and phase of transmitted microwaves; and (b) transmission spectrum with different values of the scaling factor c applied.



Figure 2.3: PEEK container containing a fixed powder sample of CoΔ. Sealed with Teflon tape.

2.3 X-Band Electron Spin Resonance

The X-Band ESR measurements on CuΔ were performed with the assistance of Dr. Markus Kurth at the Institute for Molecular Systems Engineering and Advanced Materials (IMSEAM) in Heidelberg. The employed measurement device is an EMXmicro™-6/1/P/L with an ER 070 magnet by *Bruker*. The external magnetic field can be swept up to $B = 0.645\,\mathrm{T}$ and it is modulated, such that the derivative of the transmission spectrum is measured.

The sample for the X-Band measurement was previously used for magnetization measurements in the PPMS and still contained in its PPE sample holder. The PPE container was inserted into an *Wildman*® Quartz EPR Sample Tube and subsequently into the spectrometer. Additionally the ESR spectrum of an empty sample holder contained in a quartz tube was measured, to correct the spectra for putative background effects. All measurements were carried out at room temperature and at a microwave frequency of $\nu \approx 9.81\,\mathrm{GHz}$.

Chapter 3

Numerical and Theoretical Methods

3.1 Spin Hamiltonian Formalism: An Effective Theory

It is often desirable to construct effective theories for physical problems in order to make them traceable and appropriate for the question that should be answered. In the case of this thesis the spin Hamiltonian (SH) formalism provides such a framework to understand magnetic properties of unpaired electrons. It yields a reduction in complexity from interacting electrons to fictitious spins, so that needed Hilbertspace is usually orders of magnitude smaller.

This is possible due to the difference in energy scale of magnetic and competing excitations in CoΔ and CuΔ:

- Magnetic excitations (Zeeman-splitting at a g-factor of 2): $\Delta E = 1\mathrm{T}{\cdot}2 \cdot \mu_\mathrm{B} \approx 0.1\,\mathrm{meV}$
- Spin orbit coupling (SOC constants) [31]: $\xi_{\mathrm{Co}^{2+}} \approx 62\,\mathrm{meV}$ and $\xi_{\mathrm{Cu}^{2+}} \approx 100\,\mathrm{meV}$
- Crystal field splitting for Cu^{2+} in CuΔ which is in the order of 1 eV (see chapter 5)

These lead to a large separation between the first spin multiplet of magnetic excitations and higher lying states characterized by orbital or crystal-field excitations.

3.1.1 Local g-factors and Single-Ion Anisotropy

To introduce the spin Hamiltonian formalism the first contributions to be discussed are the Zeeman-splitting and Spin-Orbit Coupling (SOC). Both of these terms locally act on the spins in a system. The Zeeman contribution describes the braking of SU(2) symmetry by applying an external magnetic field. SOC on the other hand couples the spin degrees of freedom to the spatial degrees of freedom (the orbital momentum). The Zeeman and SOC Operators are given by:

$$\hat{H}_{\mathrm{Zeeman}} := \mu_B \vec{B}^T (\hat{\vec{L}} + g_e \hat{\vec{S}}), \tag{3.1}$$

$$\hat{H}_{\mathrm{SOC}} := \lambda \hat{\vec{L}}^\dagger \hat{\vec{S}}, \tag{3.2}$$

where $\hat{\vec{L}}$ and $\hat{\vec{S}}$ denote the angular momentum and spin operators respectively and $g_e \approx 2$ is the free electron g-factor. The SOC-coupling constant is given by λ. The derivation for the spin Hamiltonian from the Zeeman and SOC Hamiltonian follow the modified perturbation procedure introduced by Pryce [32]. Eigenstates $|k\rangle$ of the unperturbed Hamiltonian $\hat{H}_0$ are characterized by some Quantum number k,

for example their orbital configuration. $\hat{H}_0$ is assumed to have a non-degenerate ground state $|0\rangle$ (apart from the usual $2S+1$-fold spin degeneracy). This ground state $|0\rangle$ is then perturbed to second order by

$$\hat{H}_1 = \hat{H}_{\mathrm{SOC}} + \hat{H}_{\mathrm{Zeeman}} = \lambda \hat{\vec{L}}^{\dagger} \hat{\vec{S}} + \mu_B \vec{B}^T (\hat{\vec{L}} + g_e \hat{\vec{S}}) \,. \tag{3.3}$$

The perturbation procedure then yields the effective spin Hamiltonian

$$\begin{aligned} \hat{H}_{\mathrm{SH}} &= \mu_B \vec{B}^T (g_e \underline{\underline{\mathbb{1}}} + 2\lambda \underline{\underline{\Lambda}}) \hat{\vec{S}}_{\mathrm{SH}} + \lambda^2 \hat{\vec{S}}^{\dagger}_{\mathrm{SH}} \underline{\underline{\Lambda}} \hat{\vec{S}}_{\mathrm{SH}} & (3.4) \\ &= \mu_B \vec{B}^T \underline{\underline{g}} \hat{\vec{S}}_{\mathrm{SH}} + \hat{\vec{S}}^{\dagger}_{\mathrm{SH}} \underline{\underline{D}} \hat{\vec{S}}_{\mathrm{SH}} \,, & (3.5) \end{aligned}$$

where $\hat{\vec{S}}_{\mathrm{SH}}$ denotes the spin operators acting within the spin Hamiltonian's Hilbert space and

$$\begin{aligned} \underline{\underline{g}} &:= g_e \underline{\underline{\mathbb{1}}} + 2\lambda \underline{\underline{\Lambda}} & (3.6) \\ \underline{\underline{D}} &:= \lambda^2 \underline{\underline{\Lambda}} \,, & (3.7) \end{aligned}$$

with $\underline{\underline{\Lambda}}$ given as:

$$\left(\underline{\underline{\Lambda}}\right)_{i,j} := -\sum_{k \neq 0} \frac{\langle 0 | \hat{\vec{L}}_i | k \rangle \langle k | \hat{\vec{L}}_j | 0 \rangle}{E_k^0 - E_0^0} \,. \tag{3.8}$$

Here E_k^0 is the unperturbed energy of the k-th exited state. $\underline{\underline{D}}$ is usually called the single ion anisotroy (SIA) term and only contributes to the Hamiltonian's spectrum if $S > 1/2$ and $\nexists c \in \mathbb{C}$ such that $\underline{\underline{D}} = c \cdot \underline{\underline{\mathbb{1}}}$. The intrinsic connection between the anisotropy of the g-tensor and the SIA should be noted to be:

$$\underline{\underline{g}} - g_e \underline{\underline{\mathbb{1}}} = 2\underline{\underline{D}}/\lambda \,. \tag{3.9}$$

From these two contributions (Zeeman and SOC) all possible 1-Spin and local 2-Spin operators have been described.

3.1.2 Spin-Spin Exchange Interaction

The next step in characterizing the spin Hamiltonian is to consider the interaction between spins at two different sites i and j. This interaction is described by the generalized Heisenberg Hamiltonian for N_{s} sites [33]

$$H_{\mathrm{SS}} = \sum_{i=1, j>i}^{N_{\mathrm{s}}} \hat{\vec{S}}^{\dagger}_{\mathrm{SH,i}} \underline{\underline{J}}^{i,j} \hat{\vec{S}}_{\mathrm{SH,j}} \,. \tag{3.10}$$

Here all non-local 2-spin operators are included. The exchange interaction tensor $\underline{\underline{J}}^{i,j}$ can also be written in terms of a sum over irreducible spherical tensors

$$\underline{\underline{J}}^{i,j} = J_{\mathrm{iso}}^{i,j} \underline{\underline{\mathbb{1}}}_3 + \underline{\underline{D_{\mathrm{DMI}}}}^{i,j} + \underline{\underline{K}}^{i,j} \,, \tag{3.11}$$

where the isotropic J_{iso} interaction, anti-symmetric (Dzyaloshinskii-Moriya) $\underline{\underline{D_{\mathrm{DMI}}}}$ interaction and anisotropic symmetric (Kitaev) $\underline{\underline{K}}$ interaction terms are $l = 0$, 1 and 2 irreducible representations, respectively. They are given by [33]

$$\begin{aligned} J_{\mathrm{iso}} &:= \mathrm{Tr}(\underline{\underline{J}}) & (3.12) \\ \underline{\underline{D_{\mathrm{DMI}}}} &:= (\underline{\underline{J}} - \underline{\underline{J}}^T)/2 & (3.13) \\ \underline{\underline{K}} &:= (\underline{\underline{J}} + \underline{\underline{J}}^T)/2 - \mathrm{Tr}(\underline{\underline{J}})/3 \cdot \underline{\underline{\mathbb{1}}} \,, & (3.14) \end{aligned}$$

where the ^{i,j} superscript is dismissed.

The different exchange coupling terms can be further characterized [33]:

- The isotropic exchange J_{iso} generally determines whether the spins in a system tend to align ferro- or antiferromagnetically.
- The Dzyaloshinskii-Moriya exchange (DMI) is given by an antisymmetric 3x3 matrix and therefore has 3 independent components. Due to this DMI can also be expressed as a vector: $\hat{\vec{S}}^{\dagger}_{\text{SH,i}} \underline{\underline{D}}^{i,j} \hat{\vec{S}}_{\text{SH,j}} = \vec{D}_{\text{DMI}} \left(\hat{\vec{S}}^{\dagger}_{\text{SH,i}} \times \hat{\vec{S}}_{\text{SH,j}} \right)$. As can be seen from it's vector form, the DMI is minimized in the case that $\vec{S}_i$ and $\vec{S}_j$ are orthogonal to each another. The antisymmetric nature of the DMI places several restrictions on the local structural symmetry around the midpoint of the exchange path. One of these constraints is that the presence of an inversion center at that midpoint immediately rules out the presence of DMI [33, 34]. Several other conditions for the existence of DMI can be found in [34].
- The Kitaev interaction is given as the symmetric traceless part of $\underline{\underline{J}}^{i,j}$ and therefore has 5 independent components. It acts in a similar fashion to SIA in that it causes the spins to prefer to lie in the direction of it's highest (lowest) eigenvalue in case of parallel (anti-parallel) ordering of the spins at i and j.

Combining these three interactions can lead to a plethora of types of magnetic order, such as, for example, the formation of skyrmion states in case of the presence of a ferromagnetic isotropic exchange and DMI [33, 35].

3.1.3 Higher Order Terms

If a systems consist of more than two individual spins, higher-order terms in the spin operators can become relevant for an adequate description of the system's magnetic properties. So for a system with N_{s} interacting spins interactions between all possible spins to order N_{s} in the spin operators are possible

$$\hat{H}_{\text{SH}} = \sum_i \left(\mu_B \vec{B}^T \underline{g} \hat{\vec{S}}_{\text{SH,i}} + \hat{\vec{S}}^{\dagger}_{\text{SH,i}} \underline{\underline{D}} \hat{\vec{S}}_{\text{SH,i}} \right) + \sum_{i,j} \hat{\vec{S}}^{\dagger}_{\text{SH,i}} \underline{\underline{J}}^{i,j} \hat{\vec{S}}_{\text{SH,j}} + \sum_{n>2}^{N_s} \hat{H}_n \tag{3.15}$$

$$\sum_{n>2}^{N_s} \hat{H}_n := \sum_{n>2}^{N_s} \left(\sum_{i_1,\ldots,i_n}^{N_s} \sum_{k_n,\ldots,k_n}^{3} \alpha^{k_1,\ldots,k_n}_{i_1,\ldots,i_n} \hat{\vec{S}}^{k_1}_{\text{SH},i_1} \ldots \hat{\vec{S}}^{k_n}_{\text{SH},i_n} \right) , \tag{3.16}$$

with $\alpha^{k_1,\ldots,k_n}_{i_1,\ldots,i_n}$ being physical parameters respecting the system's symmetries and the commutation relations of the spin operators. The construction of $\alpha^{k_1,\ldots,k_n}_{i_1,\ldots,i_n}$ will is being discussed in section 3.1.4. It should also be noted, that $\alpha^{k_1,\ldots,k_n}_{i_1,\ldots,i_n}$ can in principle be dependent on the magnetic field $\vec{B}$ [36].

3.1.4 Construction of an Effective Spin Hamiltonian

To construct an effective Spin Hamiltonian, firstly an appropriate model Hilbert-space $\mathcal{H}$ has to be defined. For a system with N_s magnetic ions at sites $0 < i \leq N_{\text{s}}$ local Hilbert-spaces $\mathcal{H}_i$ spanned by the eigenvectors of $\hat{\vec{S}}^2_i$ will be used. In this case the full Hilbert space for the SH reads

$$\mathcal{H}_{\text{SH}} := \bigotimes_{i=1}^{N_s} \mathcal{H}_i \, , \tag{3.17}$$

with the dimension N_{SH} of $\mathcal{H}_{\text{SH}}$ being:

$$N_{\text{SH}} = \sum_{i=1}^{N_s} (2S_i + 1) \, . \tag{3.18}$$

Next, a projection/map from the full electronic Hilbert space $\mathcal{H}_\mathrm{e}$ to $\mathcal{H}_\mathrm{SH}$ needs to be constructed. This first part of the procedure follows Bloch's EH theory [37]. In a first step $\mathcal{H}_\mathrm{e}$ is projected to the space $\mathcal{H}_P$ spanned by the N_SH lowest eigenstates of the electronic Hamiltonian $\hat{H}_\mathrm{e}$, containing all low lying magnetic excitations [38, 37]. Let this projector be called $\hat{P}$. This ensures that the low-energy spectrum of the Hamiltonian stays unchanged. With this projector in hand the spin operators and Hamiltonian can be projected to this subspace as well:

$$\hat{S}_i^P := \hat{P}\hat{S}_i\hat{P} \tag{3.19}$$

$$\hat{H}^P := \hat{P}\hat{H}\hat{P}\,. \tag{3.20}$$

The next step is to project the $N_\mathrm{SH} \times N_\mathrm{SH}$ matrix representation of $\hat{H}^P$ to the fictitious spin operators $\hat{\vec{S}}_{\mathrm{SH},i}$ of the SH's Hilbert space $\mathcal{H}_\mathrm{SH}$ [38]. This can be calculated straight forwardly by noting that the vector space of linear operators acting on $\mathcal{H}_\mathrm{SH}$ is isomorphic to $\mathbb{C}^{N_\mathrm{SH}}$: $\mathcal{L}(\mathcal{H}_\mathrm{SH}) \cong \mathbb{C}^{N_\mathrm{SH}}$ and that the projection can be performed by use of the canonical scalar product of $\mathbb{C}^{N_\mathrm{SH}}$

$$\langle O_1|O_2\rangle = \sum_{i,j=1}^{Ns} (O_1)^*_{i,j}(O_2)_{i,j}\,, \tag{3.21}$$

where $O_1, O_2 \in \mathcal{L}(\mathcal{H}_\mathrm{SH})$. So that for the example of two interacting spins with exchange coupling J_{zz} between their z-components J_{zz} can be obtained as follows

$$J_{zz} = \langle \hat{S}_1^z \hat{S}_2^z | \hat{H}_\mathrm{SH}\rangle\,. \tag{3.22}$$

However one has some freedom on how to choose the fictitious spin operators, since any unitary transformation acting on $\mathcal{H}_\mathrm{SH}$, leads to a valid projection of the Hamiltonian [38]. All physical properties, such as the reaction of the system to an external magnetic field, remain unchanged by such a transformation, due to the changes of the spin operators being absorbed into the parameters of the spin Hamiltonian. This is reminiscent of the construction of Wannier functions, where similar freedoms exist [39]. For example one can choose the Wannier functions such that they are maximally localized or in general most convenient [40]. One therefore needs to carefully consider one's choice of $\hat{\vec{S}}_{\mathrm{SH},i}$ for the question one wishes to answer. The operators can for example be chosen, such that the minimum number of parameters is needed for the spin Hamiltonian or that the fictitious spin operators are close to the original spin operators $\hat{S}_i^P$. To preserve the physical interpretation of the fictitious spin operators the latter option was chosen in this thesis. However there are two mechanisms which make a straight forward one-to-one map $M : \mathcal{H}_P \to \mathcal{H}_\mathrm{SH}$, $\hat{S}_i^P \mapsto \hat{S}_{\mathrm{SH,i}} := \hat{S}_i^P$ a bad choice.

- The non-ionic nature of the magnetic ion's bonds gives rise to an effective reduction of the magnitude of the spins on the corresponding ions when compared to the expected SH spin operator. As an example a $3d^{9.1}$ configuration leads to a reduction of the eigenvalues of the (1-)spin operators by 10%, i.e. $|\langle S_i^z\rangle| = 0.45 < 0.5$.
- SOC mixes higher-lying orbitally excited states into the multiplet of interest. Thus the states spanning $\mathcal{H}_P$ are not pure spin excitations any more. If this is the case, one can, for example, make use of the method developed by Chibotaru and Ungur as described in [38]. However in the case of CuΔ it turns out, that the inclusion of SOC mostly just results in a further reduction of the spin's magnitude, i.e. $|\langle S_i^z\rangle| \approx 0.39$ instead of $|\langle S_i^z\rangle| \approx 0.5$. There are several other effects related to SOC which will be discussed in more detail in section 3.1.4.

Thus for CuΔ the map $M : \mathcal{H}_P \to \mathcal{H}_\mathrm{SH}$, $\hat{S}_i^P \mapsto \hat{S}_{\mathrm{SH,i}} := \hat{S}_i^P / f_i$ for some appropriate f_i yields meaningful results. With the given map the symmetries and alignment of the true spin operators $\hat{S}_i^P$ are preserved.

Meaning that the coordinate system stays unchanged and that the fictitious spin operators $\hat{S}_{\mathrm{SH}}$ are close to the spin operators defined in the DFT calculation. When comparing the SH in the $\hat{S}_i^P$ basis to the SH in the $\hat{S}_{\mathrm{SH,i}}$ the only difference is a rescaling of the SH-parameters so that the Hamiltonian stays unchanged.

Note here, that the method described in this section differs somewhat from the typical methods employed for this kind of mapping between *ab-initio* calculations and spin Hamiltonians. Compared to, for example, the 4-state method [41], it does not rely on the rigid spin rotation approximation [33]. When compared to fitting of a guessed spin Hamiltonian, it does not suffer from over parametrization [33] and instabilities in the fitting algorithm. In other words: the scheme presented here is in principle exact and determines a unique mapping. This comes at a cost of course: On the one hand the full spin-multiplet needs to be known, instead of, for example, only 4-8 states (for the 4-state method [41]). On the other hand there is the problem of mapping the projected spin operators to their SH counterparts, when SOC is involved. This mapping is not perfect as will be shown in section 5.4, but this is an intrinsic issue of these kinds of energy mapping analyses.

3.2 Density-Functional-Theory

As a foundation for the *ab-initio* calculation of the magnetic properties of CuΔ , described in chapter 5 density functional theory (DFT) is employed. It is based on the Hohenberg-Kohn theorems [42], which state that the ground state energy E_0 of a many electron system is uniquely defined by it's electronic density $\rho(r)$ and that there exists a universal functional $F[\rho]$ such that

$$E_0 = F[\rho(r)]\,, \tag{3.23}$$

where $\rho(r)$ for a system with n electrons and a ground state ψ_0 is given by

$$\rho(r) = n \int \prod_{i=2}^{n} dr_i |\psi_0(r, r_2, ..., r_n)|^2\,. \tag{3.24}$$

Having knowledge of the universal functional $F[\rho]$ would reduce the complexity and computational cost for any given system from one that rises exponentially with the number of basis states and electrons to one that increases only linearly with system size. Unfortunately such a universal functional is unknown. The question that arises naturally is, whether one can find suitable approximations for this functional. Within the method developed by Kohn and Sham [43] this question is answered by introducing a set of non-interacting quasi particles (described by wave functions $\{\phi_i\}_i$), in such a way that the ground state density of this non-interacting system ρ_{KS} is identical to the original one. Thus the energy of the system can be described as:

$$E_0 = F[\rho] = T[\rho] + V[\rho] + U[\rho] \tag{3.25}$$

where T denotes the kinetic energy, $V = V_{\mathrm{eN}}$ the electrostatic potential generated by the nuclei and $U = V_{\mathrm{ee}}$ the electron-electron repulsion. For the electrostatic potential an exact representation for the functional is given by [44]

$$V[\rho] = \int dr V_{\mathrm{eN}}(r)\rho(r)\,. \tag{3.26}$$

In the Kohn-Sham method, the kinetic energy can be described as the kinetic energy of the quasi-particles plus some correction term [44]

$$T[\rho] = -\frac{\hbar^2}{2m} \sum_i \langle \phi_i | \nabla^2 | \phi_i \rangle + T_{\mathrm{correlation}}\,. \tag{3.27}$$

Similarly the electron-electron interaction can be expressed as a sum of the classical coulomb energy, an exchange and correction term [44]

$$U[\rho] = \frac{e^2}{2} \int dr dr' \frac{\rho(r)\rho(r')}{|r - r'|} + U_{\text{exchange}} + U_{\text{correlation}} \,. \tag{3.28}$$

Knowledge of the exact form of the entire exchange-correlation functional $E_{\text{XC}} := T_{\text{correlation}} + U_{\text{exchange}} + U_{\text{correlation}}$ would result in an exact theory, but since it is not known appropriate approximations of E_{XC} [44, 45] are needed. One of these approximate techniques, which is also employed in chapter 5 of this thesis, are the LDA[1] functionals. Here E_{XC} is expressed as a locally on $\rho(r)$ dependent quantity

$$E_{\text{XC}} \quad = \quad \int dr e_{\text{XC}}(\rho(r)) \,. \tag{3.29}$$

To determine the exchange-correlation density e_{XC}, e_{XC} is usually fitted to simulated results obtained for simple systems, such as the homogeneous electron gas [45]. This scheme can be amended by my more complicated forms of e_{XC} such as including the first (GGA[2]) and second (meta-GGA) derivatives of ρ in the exchange-correlation energy functional [45].

Armed with this, the second Hohenberg-Kohn theorem can them be used to obtain a set of self consistency equations reminiscent of the Hatree-Fock equations [44, 45]. Solving these equations self consistently finally yields the one particle eigenstates and therefore the systems mean field groundstate.

[1] Local Density Approximation
[2] Generalized Gradient Approximation

Chapter 4

Experimental Results

Both samples which were investigated in this thesis, namely CoΔ and CuΔ, were synthesized in the research group of *I. Morosov* and *A. Vassiliev* (*Moscow State University*). The characterization of the samples was performed by A. Vassiliev *et al.* using powder XRD at a temperature of 130K [22, 46, 23]. A picture of CoΔ crystallites can be found in figure 4.1.



Figure 4.1: Picture of CoΔ crystallites.

4.1 Cobalt Triangle: $NMe_4[Co_3(\mu_3\text{-F})(TFA)_6(Py)_3]$

4.1.1 Structure

$NMe_4[Co_3(\mu_3\text{-F})(TFA)_6(Py)_3]$ (CoΔ) crystallizes in the hexagonal space group $P6_3/m$ (176) with lattice parameters $a = b = 12.2967(2)$ Å, $c = 17.3266(4)$ Å [23, 46]. The crystal structure can be separated into the solvent or cation $[NMe_4]^+$ and the molecule/anion $[Co_3(\mu_3\text{-F})(TFA)_6(Py)_3]^-$. It is displayed in figure 4.2(a) and close ups of the formula unit, i.e. the solvent $[NMe_4]^+$ and molecule $[Co_3(\mu_3\text{-F})(TFA)_6(Py)_3]^-$ are plotted in figures 4.2(b) and 4.2(c) respectively. The distance between the μ_3−F of the two molecules contained in one unit cell is $d_{\text{inter:F-F}} = 11.201$ Å and the distance of the closest cobalt ions between the two molecules amounts to $d_{\text{inter:Co-Co}} = 9.418$ Å. The cobalt ions are in the Co^{2+} ionization state and therefore in a $3d^7$ electronic configuration. For this configuration the Co^{2+} can either be in a low spin state ($S = \frac{1}{2}$) or in a high spin state ($S = \frac{3}{2}$).

The anion has a C_{3h} point group symmetry, with the C_3 axis pointing through the central fluorine (μ_3−F). This high symmetry axis is perpendicular to the plane spanned by the three cobalt ions. These ions have a distance of d(Co-Co) = 3.556 Å to each other and a distance of d(Co-F) = 2.053 Å to the central

fluorine. Locally the cobalt ions are coordinated by four oxygen atoms, one nitrogen atom and the μ_3−F. For reference see figure 4.2(d)). Only considering their nearest neighbors the Co^{2+}-ions exhibit a local C_s symmetry with the σ_h mirror plane being the same as the one for the entire molecule. To some degree of approximation one could alternatively consider the local environment of the cobalt ions to have a C_{2v} or even C_{4v} symmetry with the high symmetry axis pointing along the N-Co-F bond. However this is only approximately true because the angle of the N-Co-F bond differs from 180°, i.e. $\sphericalangle$(N-Co-F) = 177.27°, and the bonding angles between two neighboring oxygen atoms and the cobalt ions deviate from 90° as $\sphericalangle(O_0\text{-Co-}O_1) = 94.51°$, $\sphericalangle(O_1\text{-Co-}O_2) = 86.18°$, $\sphericalangle(O_2\text{-Co-}O_3) = 92.93°$ and $\sphericalangle(O_3\text{-Co-}O_0) = 86.18°$.

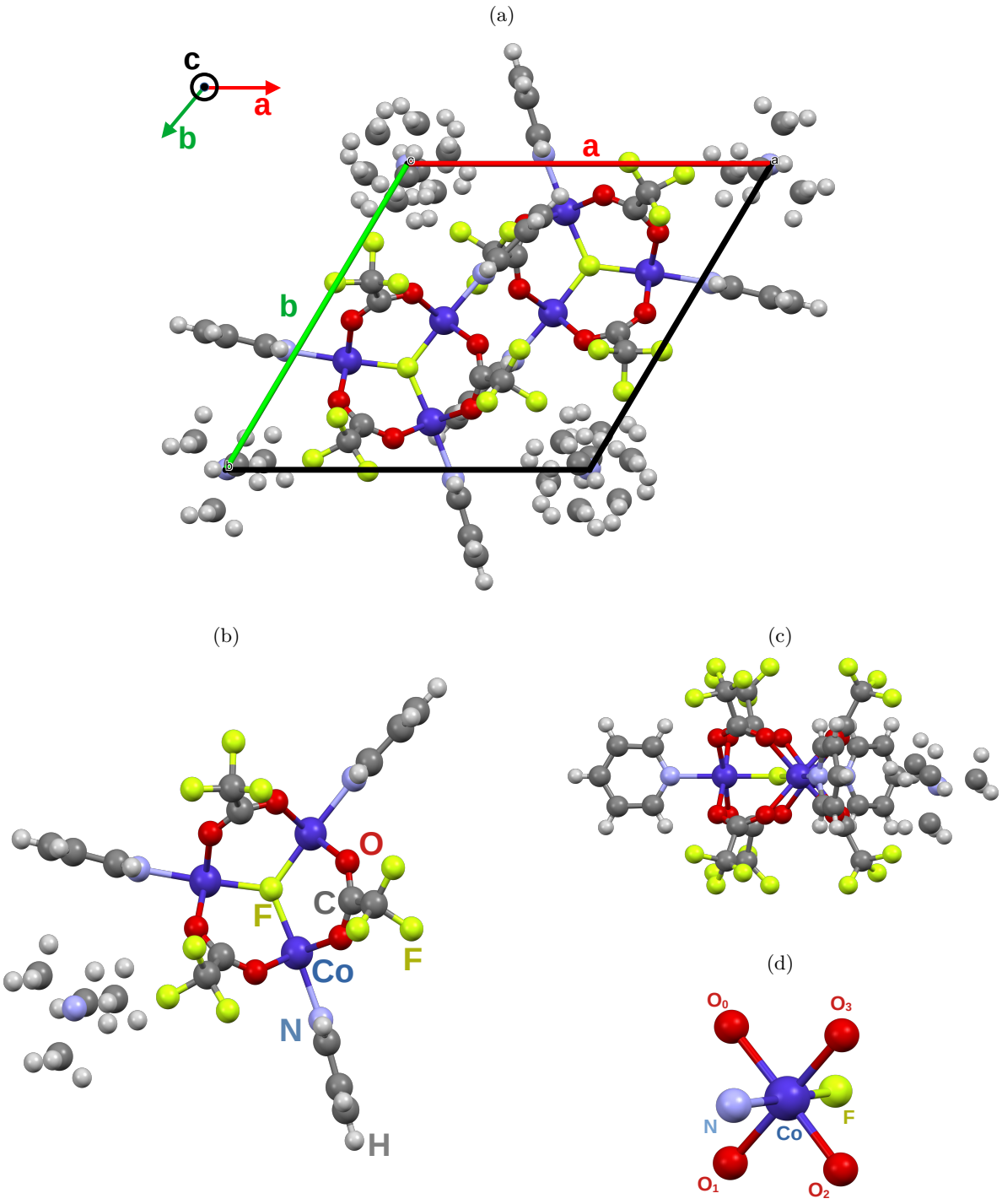


Figure 4.2: Depiction of the crystal structure of CoΔ: (a) Crystal structure of CoΔ viewed along the *c*-axis. One unit cell is comprised of two formula units, which are shifted in the c-direction and rotated by 180°. Only molecules with their center in the unit cell are displayed and shown in their entirety. (b), (c) one formula unit including the solvent and molecular part of the crystal. (d) Local Co^{2+} environment: Nearest neighbors, the oxygen atoms are numerated counter clockwise starting from O_0. Crystallographic data was provided by *I. Morosov* [46, 23] and displayed using *Mercury* [47].

4.1.2 Static Magnetic Properties

Measurement and Data

The static isothermal magnetization $M(B, T = \text{const})$ and static susceptibility $\chi(T) := M(B,T)/B|_{B=\text{const}}$ were measured by *A. Elghandour* [48] using the PPMS (see section 2.1). A fixed powder sample was used, so that all measured quantities are solid angle averages. The used sample's mass is $m_{\text{Co}\Delta} = 13.3(3)\,\text{mg}$. The uncertainties given in this section include the uncertainty in determining the sample mass and the uncertainties provided by the PPMS. The data shown here are corrected for the temperature-independent diamagnetic contribution, as described in section 2.1.

Figure 4.3(a) depicts the isothermal magnetization of CoΔ at various temperatures. The magnetization curve for $T = 2\,\text{K}$ clearly exhibits two plateaus and a step like feature, which are typical for antiferromagnetic coupling in triangular lattices [49, 50]. This behavior can also be seen in the derivative of the magnetization $\partial_B M(B,T)$ (fig. 4.3(b)). Here one can observe a minimum and maximum, which roughly corresponds to the center of the first plateau and the center between the two plateaus respectively. At $T = 2\,\text{K}$ this maximum occurs at $B_\text{c} \approx 8.3\,\text{T}$. These steps are indicative of a transition of the ground state as a function of the magnetic field, where its spin expectation value increases.

Here one can observe that the minima and maxima of $\partial_B M(B,T)$ shift to higher fields with increasing temperature. At $B = 14\text{T}$ the magnetization reaches

$$M(B = 14\text{T}, T = 2\,\text{K}) = 5.52(12)\,\frac{\mu_B}{\text{f.u.}}\,, \tag{4.1}$$

where f.u. stands for formula unit. If cobalt is assumed to be in the low spin state this would imply an average g-factor of at least $\langle g_{\text{LS}}\rangle_\Omega > 3.77(8)$. For the high spin state the same estimate yields the constraint $\langle g_{\text{HS}}\rangle_\Omega > 1.227(27)$.

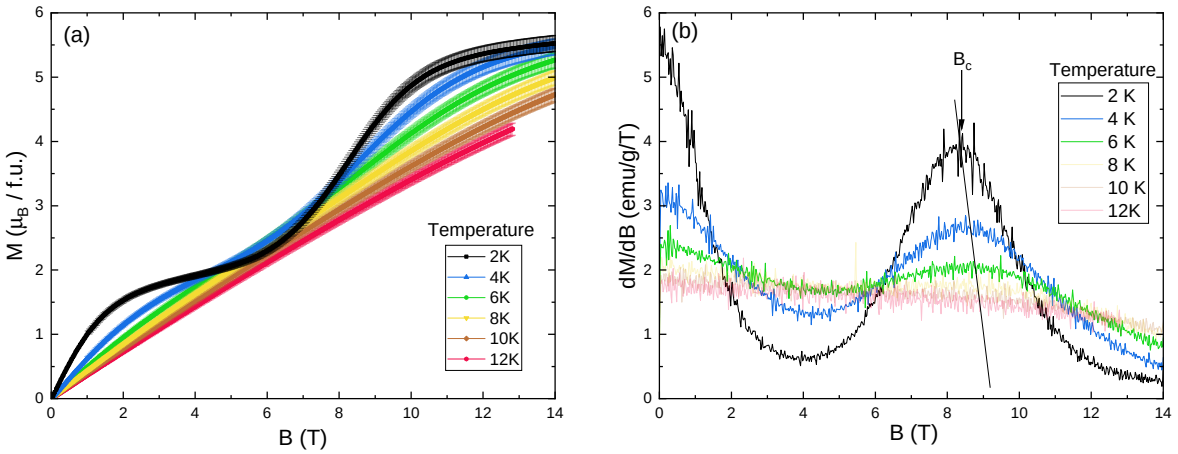


Figure 4.3: (a) Isothermal magnetization $M(B, T = \text{const})$ of CoΔ measured by *A. Elghandour* [48] for a sample of fixed CoΔ powder at various temperatures in the range from 2 K to 12 K. (b) Derivative of $M(B, T = \text{const})$ with respect to the magnetic field B. The data are corrected for the systems diamagnetic contribution (see equations 2.2 and 2.5).

The $\chi T(B = \text{const}, T)$ curve, shown in figure 4.4, increases monotonically until reaching a constant Curie behavior, where χT levels, supporting the hypothesis of antiferromagnetically coupled Co^{2+}-spins [51]. As marked by the blue line in the inset of figure 4.4, the χT curve saturates at a value of

$$\chi T(B = 100\text{mT}, T = 300\,\text{K}) = 6.50(15)\,\frac{\text{erg K}}{\text{G}^2\text{mol}}\,. \tag{4.2}$$

The solid angle averaged g-factor can be calculated from this value with the use of the Curie law for free spins [51]

$$\chi_{\text{free}}T = n\frac{\mu_0\mu_B^2 g^2 S(S+1)}{3k_B} \equiv C\,, \tag{4.3}$$

where n is then number of free spins, S their spin value and k_B represents the Boltzmann factor. For this system $n = 3$ and $S \in \{1/2, 3/2\}$ are appropriate values. This equation then yields an average g-factor of $\langle g_{\text{HS}}\rangle_\Omega = 2.147(24)$ for the high spin case and $\langle g_{\text{LS}}\rangle_\Omega = 4.80(6)$ for the low spin case. Both of these values are consistent with the restrictions imposed by the isothermal magnetization measurements. One can conclude that the high spin state of Co^{2+} is more likely, due to it's g-factor being in a more plausible range [52].

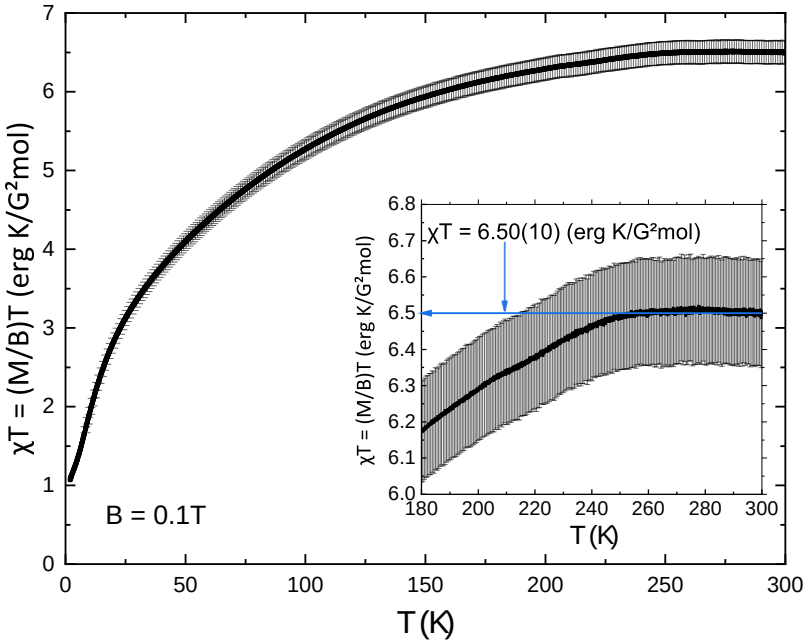


Figure 4.4: Product of $\chi = \frac{M(B,T)}{B}$ with temperature T, χT, is shown. The data in this figure were measured at a magnetic field of $B = 100\,\text{mT}$ by *A. Elghandour* [48] for the fixed CoΔ powder sample. The inset depicts a close up on the high temperature range with the blue line showing the constant value approached for $T \nearrow 300\,\text{K}$. The data are corrected for the systems diamagnetic contribution (see equations 2.2 and 2.6).

Spin Hamiltonian Fitting

In order to gain a better understanding of the observed static magnetic properties a model spin Hamiltonian is fitted to the measured data. The used spin Hamiltonian consists of an isotropic exchange term H_{ex}, a Zeeman term H_{Z}^i and a single ion anisotropy term H_{SIA}^i (acting on site i):

$$\hat{H}_{\text{Co}\Delta} = \hat{H}_{\text{ex}} + \sum_{i=0}^{2}(\hat{H}_{\text{Z}}^i + \hat{H}_{\text{SIA}}^i) \tag{4.4}$$

$$= J\sum_{i=0,j>i}^{2}\hat{\vec{S}}_i^\dagger\hat{\vec{S}}_j + \sum_{i=0}^{2}(\mu_B\hat{\vec{S}}_i^\dagger\underline{\underline{g_i}}\vec{B} + \hat{\vec{S}}_i^\dagger\underline{\underline{D_i}}\hat{\vec{S}})\,. \tag{4.5}$$

The operator-hat $\hat{O}$ will be dismissed from this point on. The number of free parameters in equation 4.5 is reduced by enforcing the C_3 symmetry of the molecule, as well as equation 3.9 to equate the g-tensor

and SIA-tensor. Thus the spin Hamiltonian reads

$$H_{\mathrm{Co}\Delta} = J\sum_{i=0,j>i}^{2}\vec{S_i}^{\dagger}\vec{S_j} + \sum_{i=0}^{2}(\mu_B\vec{S_i}^{\dagger}(R^i)^T\underline{\underline{g_0}}R^i\vec{B} + \vec{S_i}^{\dagger}(R^i)^T(\underline{\underline{g_0}} - 2\mathbb{1})\frac{\lambda}{2}R^i\vec{S_i}) \tag{4.6}$$

$$= J\sum_{i=0,j>i}^{2}\vec{S_i}^{\dagger}\vec{S_j} + \sum_{i=0}^{2}(\vec{S_i}^{\dagger}(R^i)^T\underline{\underline{g_0}}R^i(\frac{\lambda}{2}\vec{S_i} + \mu_B\vec{B})) - \lambda\vec{S_i}^{\dagger}\vec{S_i}\,. \tag{4.7}$$

Exploiting the relation $\vec{S_i}^{\dagger}\vec{S_i} \equiv \frac{3}{2}(\frac{3}{2}+1)\mathbb{1} = \frac{15}{4}\mathbb{1}$, equation 4.7 reduces to

$$H_{\mathrm{Co}\Delta} = J\sum_{i=0,j>i}^{2}\vec{S_i}^{\dagger}\vec{S_j} + \sum_{i=0}^{2}(\vec{S_i}^{\dagger}(R^i)^T\underline{\underline{g_0}}R^i(\frac{\lambda}{2}\vec{S_i} + \mu_B\vec{B}))\,, \tag{4.8}$$

where $\lambda = 515\mathrm{cm}^{-1}$ depicts the experimentally determined SOC constant for Co^{2+} [31] and R represents a rotation matrix rotation the reference frame by 120° around the c-axis. Assuming C_4 symmetry with a small distortion (effectively C_2) for the local environment of the cobalt spins, the g-tensor can be written in the form

$$\underline{\underline{g_0}} = \mathrm{diag}(g_\perp, g_\perp + \delta g_\perp, g_{||})_{\delta g_\perp \approx 0}\,. \tag{4.9}$$

The principle axes are oriented in such a way that the N-Co-F bond coincides with $g_{||}$. Due to $\delta g_\perp \approx 0$, the orientation of the g-factor in the plane of $g_\perp$ is mostly irrelevant. Thus the orientation of the remaining two principle axes is assumed to be rotated by 45° around the N-Co-F bond with respect to the c-axis. The principle axis roughly correspond to the bonds around the cobalt ions.

The resulting spin Hamiltonian is implemented in *EasySpin* (version 6.0.0-dev51) [53] and fitted to the $\chi T(T)$ data at $B = 100\,\mathrm{mT}$ and $M(B)$ data at $T \in \{2\,\mathrm{K}, 4\,\mathrm{K}\}$ simultaneously. A temperature independent paramagnetic contribution χ_{TIP} is employed additionally to account for the lack of sample holder background correction. The resulting fit can be seen in figure 4.5 and the best fit parameters are given in table 4.1. These yield an average g-factor of $\langle g\rangle_\Omega = 2.20(5)$ which is consistent with the estimate made from the room temperature limit of χT. Assuming the fit parameters in table 4.1 the expected saturation magnetization is $M_{\mathrm{sat}} = 3\langle g\rangle_\Omega \cdot \frac{3}{2} = 9.90(23)\,\mu_B/\mathrm{f.u.}$. With this spin Hamiltonian 95% of the saturation magnetization is reached at approximately $B_{95\%} \approx 240\,\mathrm{T}$ after another increase in slope before plateauing again (see figure 4.6). Note here, that all anisotropy in the system was absorbed into the SIA, and therefore the anisotropy of the g-tensor due to their relation through second order perturbation theory (see equation 3.9). In principle, anisotropic exchange such as DMI and Kitaev interaction could also play a role.

Parameter	Best Fit Value
J	92.0(1.2) GHz
$g_{\|\|}$	2.400(16)
$g_\perp$	2.117(12)
$\delta g_\perp$	−0.05(4)
χ_{TIP}	$-0.00177(20)\ \frac{\mathrm{cm}^3}{\mathrm{mol}}$

Table 4.1: Best fit values of the fit parameters for a simultaneous fit to the the $\chi T(T)$ data at $B = 100\mathrm{mT}$ and $M(B)$ data at $T \in \{2\mathrm{K}, 4\mathrm{K}\}$. The fit was performed using *EasySpin* [53]. Errors depicted here are purely the fit errors, i.e. the square root of the covariance matrix generated by *easypin*.

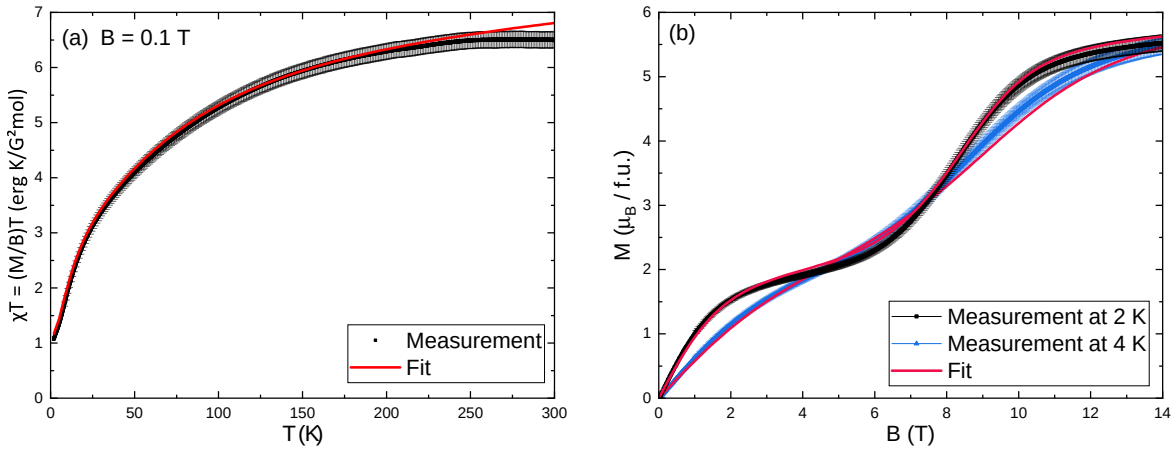


Figure 4.5: (a) Static susceptibility χ times temperature T (at $B = 100\text{mT}$) and (b) isothermal magnetization at $T \in 2\text{K}, 4\text{K}$ including a fit of equation 4.8 to the data. The best fit values are depicted in table 4.1 and the fit was performed using *EasySpin* [53]. The data in this figure were measured by *A. Elghandour* [48] with a sample of fixed CoΔ powder.

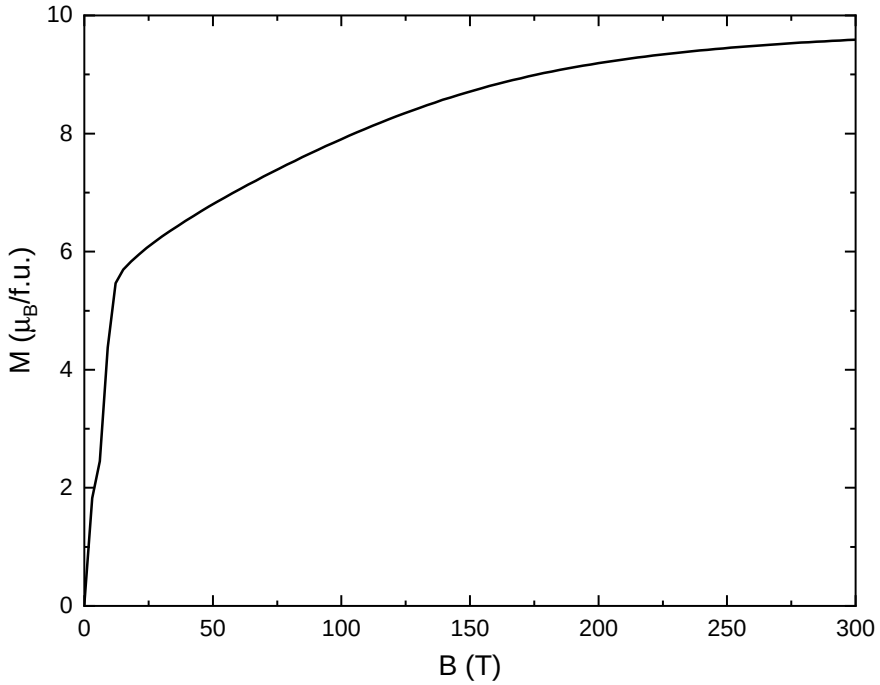


Figure 4.6: Simulated isothermal magnetization curve up to $B = 300\,\text{T}$ at $T = 2\,\text{K}$. The magnetization was calculated using equation 4.8 with fitted parameters given in table 4.1. The simulation was performed using *EasySpin* [53].

4.1.3 High-Field/High-Frequency ESR Studies

High-Field/High-Frequency ESR measurements were performed on a fixed powder sample of CoΔ (fixed with high temperature vacuum grease). Recorded spectra were phase corrected (see section 2.2), such that the main feature exhibits little to no phase mixing. The spectra were recorded at $T = 2\,\mathrm{K}$ and $T = 10\,\mathrm{K}$. The latter temperature was chosen because at $T = 10\,\mathrm{K}$ some transitions between exited states are reasonably visible (see figures 4.11, 4.12(a) and 4.13).

The resonance field of a resonance feature is determined by noting the transmission minimum after phase correction of the signal in question. The respective uncertainty is estimated by measuring the FWHM of the feature in question by hand. Some of the features are too broad for a clear assignment and exhibit a substructure. In this case no clear assignments can be made and the center of the feature is taken with an appropriately large uncertainty. A feature is also only considered to be intrinsic if it appears in both the up- and the down-sweep of a measurement and if the detected phase exhibits the characteristic shape of the derivative of a Lorentzian/Gaussian [24] at the putative resonance field. If phase mixing appears the shape of the phase signal will be a mixture of the true transmission peak and its derivative [30, 24]. The final resonance field of a feature is then determined by calculating the average of the up- and down-sweeps, to account for shifts induced by the sweeping direction of the field.

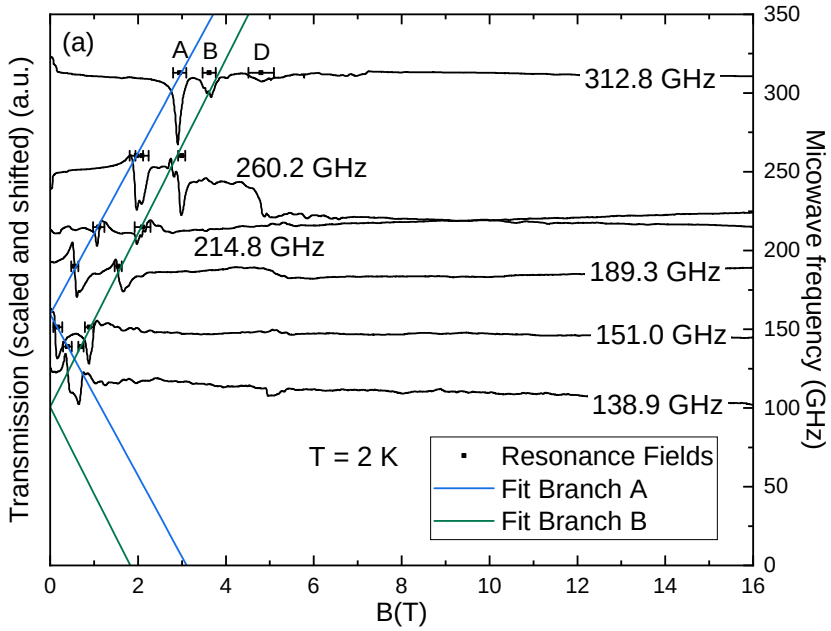


Figure 4.7: HF-ESR transmission spectra (down sweeps) at $T = 2\mathrm{K}$ with the visible resonances as the blue squares. Linear fits for branches A and B are included as solid lines. The measurement was performed on a sample of fixed CoΔ powder.

The non-phase-corrected ESR spectra at $T = 2\,\mathrm{K}$ are plotted in figure 4.7. Here the down sweeps are shown, i.e. the spectra recorded with $\dot{B} = -1\,\mathrm{T/min}$ starting from $B_0 = 16\,\mathrm{T}$. In the spectrum measured at $\nu = 189.3\,\mathrm{GHz}$ phase mixing is well visible at the two resonance features marked in the plot. One can observe two pronounced resonance features, labeled by the letters A and B. Those features exhibit some additional superstructure well resolved in the $\nu = 260.2\,\mathrm{GHz}$ and $\nu = 312.8\,\mathrm{GHz}$ spectra. Features A and B merge partly in the $\nu = 138.9\,\mathrm{GHz}$ spectrum, while still remaining distinguishable. In the $\nu = 312.8\,\mathrm{GHz}$ spectrum an additional feature (labeld as D) can be observed.

The obtained resonance field positions are plotted in figure 4.7. For the resonance branches A and B a

linear regression is performed to obtain their slopes and thereby the effective g-factor $g_{\text{eff}} = g \cdot \Delta S_z$ (ΔS_z denotes the change in the S_z quantum number during the transition) and the zero field splitting Δ, i.e. the y intercept of the resonance branches. The fitted parameters are shown in table 4.2. Fitting was conducted using Scipy's ODR package [54].

Branch	A	B
effective g_{eff}	3.69(4)	4.12(19)
Δ (GHZ)	159.9(7)	99(3)

Table 4.2: Effective g-factors and ZFS of the resonance branches A and B as determined by linear fits of the form $\nu(B) = \Delta + 13.98\,\frac{\text{GHz}}{\text{T}} \cdot g \cdot B$ (see figure 4.7). The fitting was performed using Scipy's ODR package [54].

The phase corrected spectra at $T = 10\,\text{K}$ are plotted in figures 4.8 (up-sweep) and 4.9 (down-sweep). The observed resonance features are also marked by squares in those figures. The most pronounced features A and B can be observed at $T = 10\,\text{K}$ as well. While the intensity of A remains almost constant for all measured frequencies, the relative spectral weight of B to A (and the rest of the spectrum) decreases for increasing frequencies. It can also be observed that the intensity of the resonance features E and F increases significantly for $\nu \gtrsim 350\,\text{GHz}$, or in other terms for $B \gtrsim 7\,\text{T} - 8\,\text{T}$. This indicates that the system in close to a transition between two ground states in this field range, which is consistent with the observed peak in the $\partial_B M(B)$ data. It has to be noted, that in some spectra features A and B exhibit a superstructure. This is noted with the subscripts 1 and 2, i.e. A_1, A_2, B_1 and B_2.

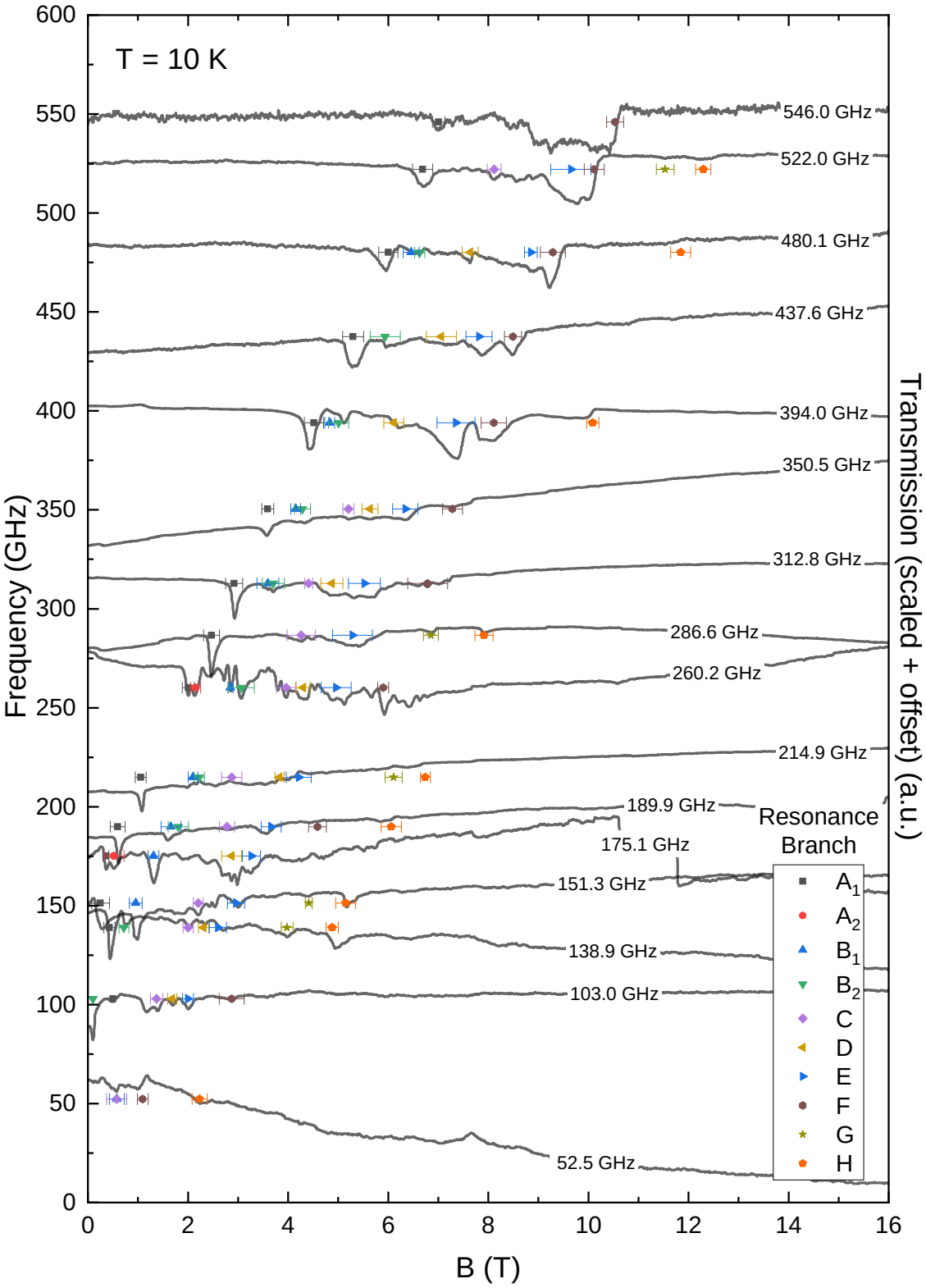


Figure 4.8: Phase corrected HF-ESR transmission spectra (up-sweep) at $T = 10\,\mathrm{K}$. The spectra are shifted and scaled for better clarity of the plot. The observed resonances are marked by the black squares and positioned according to the ordinate on the left. The measurement was performed on a sample of fixed CoΔ powder.

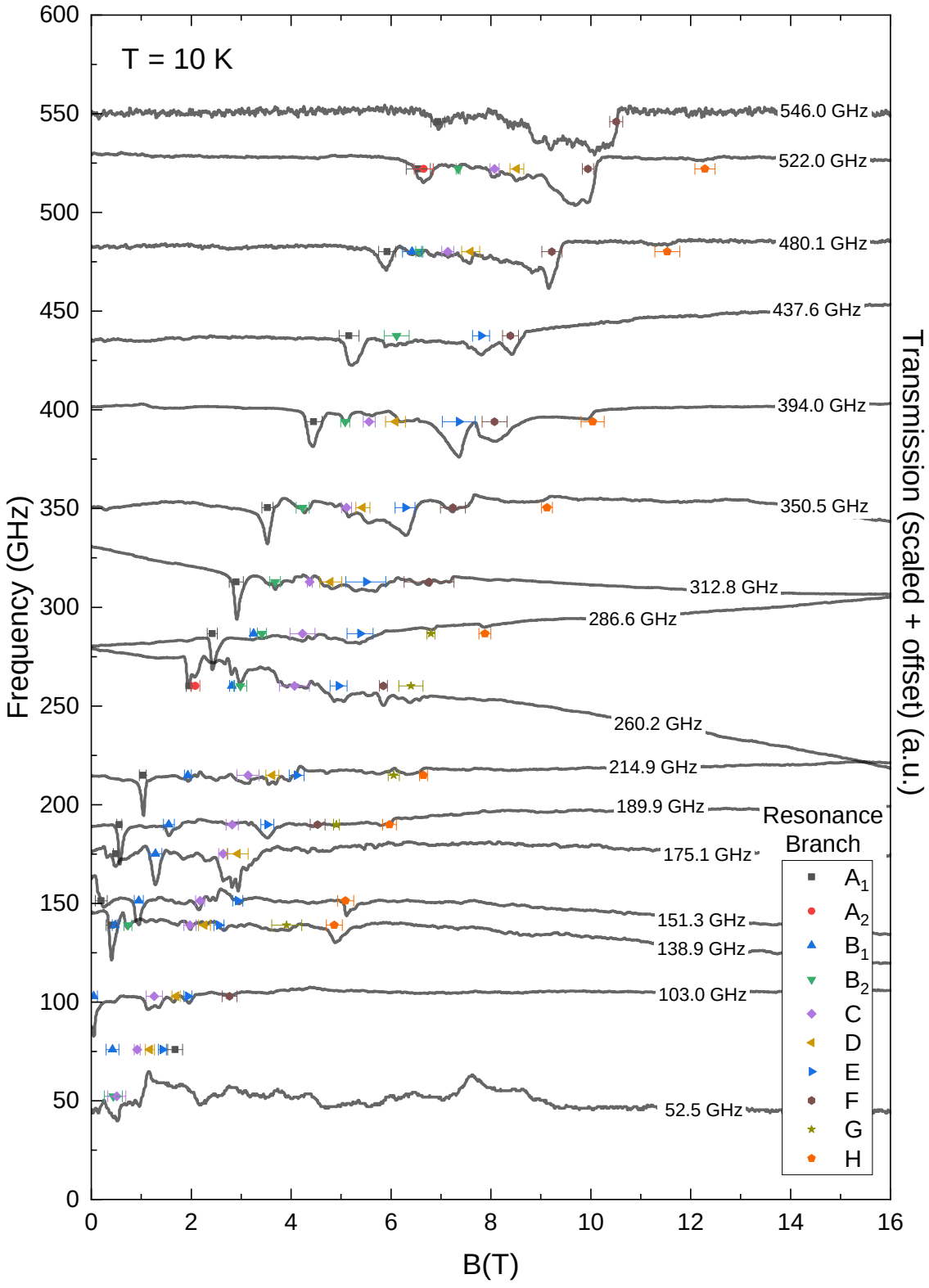


Figure 4.9: Phase corrected HF-ESR transmission spectra (down-sweep) at $T = 10\,\mathrm{K}$. The spectra are shifted and scaled for better clarity of the plot. The observed resonances are marked by the black squares and positioned according to the ordinate on the left. The measurement was performed on a sample of fixed CoΔ powder.

All observed resonance features are summarized in a ν-B diagram (figure 4.10). The resonance features are arranged on almost linear branches. To asses these, similar linear fits as for the 2K data were performed and the best fit parameters are shown in table 4.3. To asses whether the branches are truly linear or exhibit some bending/non-linearity the reduced χ^2_{reduced} value of the fit is computed [55]. Note, that this test is appropriate in this case, because a truly linear model is fitted to the data [55].

All observed branches have a slope corresponding to a g-Factor larger than $g \gtrsim 3.5$ indicating the observation of forbidden transitions and/or that the relevant eigenstates are far from pure spin eigenstates, meaning that the resonances stem from mixed states. These would include admixtures of states with higher spins along the direction of the field $S_{||B}$.

First of all one must note that $\chi^2_{\text{reduced}} = 22.85$ for branch G, which is reasonable, since it only contains 3 data points which cannot be described by a linear fit. For this reason, the fit was excluded from figure 4.10. All other fits have χ^2_{reduced} values in the range of $0.42 \leq \chi^2_{\text{reduced}} \leq 2.92$. Since the linear fit is already a quite minimal model (2 parameters), the $\chi^2_{\text{reduced}} < 1$ probably results from overestimating the uncertainties. $\chi^2_{\text{reduced}} > 1$ on the other hand indicates a poor fit, meaning that the employed model is not appropriate. This can already be seen from figure 4.10, since bending of the resonance branches can be observed especially for the fields in the range of $6\,\text{T} \leq B \leq 8\text{T}$. This reveals slight upward bending for branches A, B, D, E, F and H and some downward bending for branch C. Bending of the resonance branches can be explained by considering that the SU(2) symmetry of the spins is broken by SOC in combination with the coordinating ligands introducing spatial anisotropy (SIA and anisotropic exchange in the spin Hamiltonian formalism). This leads to mixing of pure spin eigenstates states as a function of applied magnetic field, thus leading to the observed non-linear behavior. At this field range there also occurs the ground state transition, observed in the $M(B, T = \text{const})$ data, which indicate that the mixing occurs between the ground state for $B < B_\text{c}$ and the new ground state for $B > B_\text{c}$. When comparing the fit for branches A and B at $T = 2\,\text{K}$ to the one performed at $T = 10\,\text{K}$ it becomes apparent that the fitted slopes at $T = 10\,\text{K}$ are significantly larger than for $T = 2\,\text{K}$. This can simply be explained by the observed upward bending of the relevant resonance branches for higher fields, which occurs at fields larger than were reached for the frequencies of the $T = 2\,\text{K}$ measurement.

Branch	A	B_1	B_2	C	D	E	F	G	H
g_eff	3.97(5)	4.22(6)	4.17(6)	4.52(7)	4.52(14)	4.04(8)	4.33(10)	4.1(1.3)	3.60(11)
Δ (GHz)	153(2)	94.5(2.5)	96(4)	16(4)	−4(7)	−11(4)	−87(10)	−110(110)	−114(11)
χ^2_{reduced}	1.37	0.42	0.84	1.04	2.92	0.66	1.76	22.85	2.06

Table 4.3: Effective g-factors g_eff and ZFS Δ of all observed resonance branches as determined by linear fits of the form $\nu(B) = \Delta + 13.98\,\frac{\text{GHz}}{\text{T}} \cdot g \cdot B$ (see figure 4.10). Additionally the reduced χ^2_{reduced} value of the fit is given in order to asses it's merit. The fitting was performed using Scipy's ODR package [54].

In order to determine whether the observed resonance features originate from transitions between the ground state and an exited state or between exited states, subject spectra were measured at the fixed frequencies $\nu = 75.9\,\text{GHz}$, $\nu = 312.8\,\text{GHz}$ and $\nu = 522.0\,\text{GHz}$ for varying temperatures. Those frequencies were chosen because the measured signal exhibits little to no phase mixing, such that the intensities between different temperatures are comparable. The recorded spectra are plotted in figures 4.11, 4.12(a) and 4.13. A zoomed in version of figure 4.12(a) is depicted in figure 4.12(b). Using these temperature sweeps (more specifically the evolution of a feature's intensity with temperature) it can be determined whether an observed resonance feature arises from a ground state transition or a transition between exited states. For a resonance feature arising from a ground state transition one expects a continuously decreasing intensity with increasing temperature, due to an increase in the thermal population of the

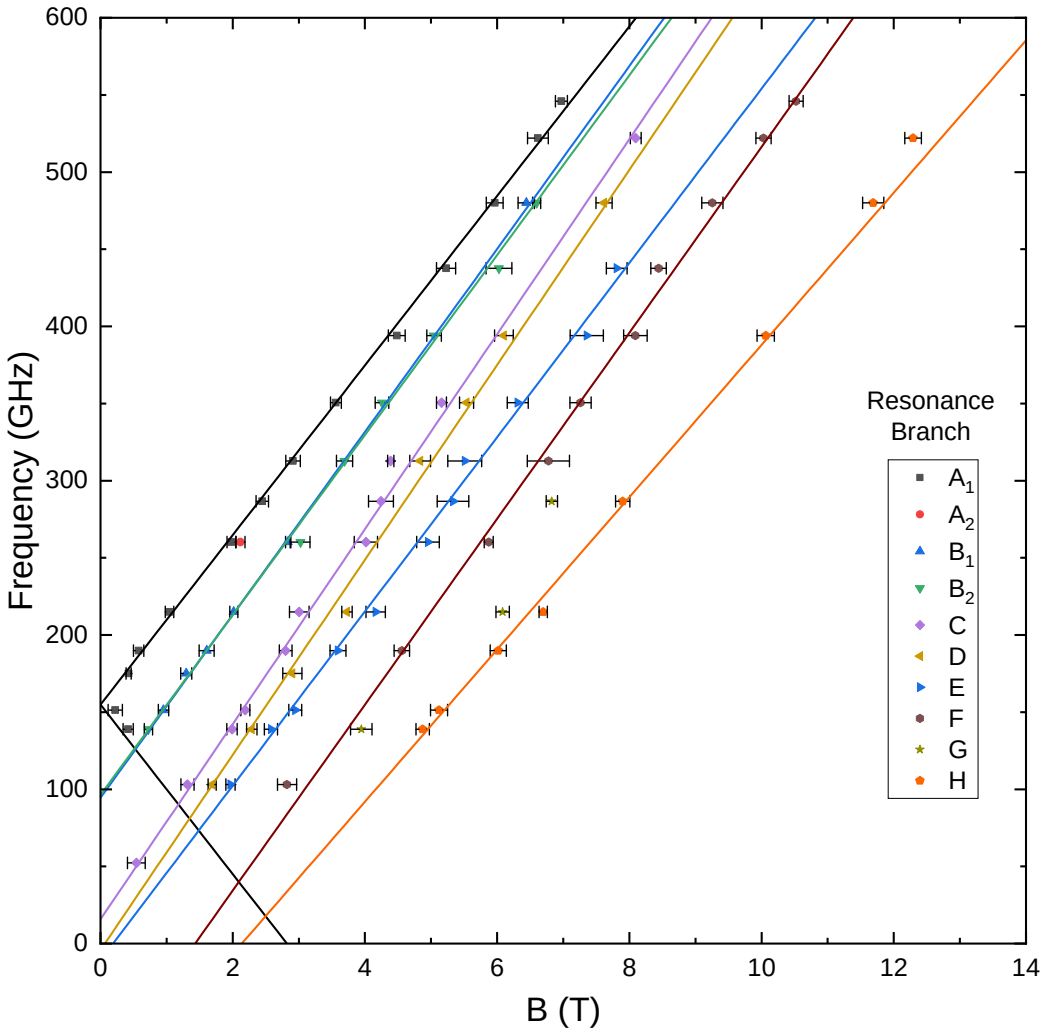


Figure 4.10: Resonance field-frequency diagram for fixed CoΔ powder at $T = 10\,\mathrm{K}$. The displayed resonance positions are averaged over the respective positions in the up- and down-sweeps. Linear fits are included as solid lines, as discussed in the text.

higher lying state. This reduces the overall intensity because the target phase-space is more populated than for lower temperatures. If the intensity increases up to a given temperature and decreases afterwards, this would indicate a transition between exited states. Here the thermal population of the involved initial state increases for increasing temperature, since it is not the ground state, thereby increasing the transition probability. The target state's thermal population increases as well, such that there comes a temperature where the same effect of a reduced target phase-space reduces the transition probability again. To show the intensity evolution more clearly, the intensity of the resonance features as a function of temperature is plotted in in figures 4.14(a) and 4.14(b) for $\nu = 75.9\,\mathrm{GHz}$ and $\nu = 312.8\,\mathrm{GHz}$ respectively. The intensity is determined by first estimating a suitable field range, including most of the feature. The chosen field ranges are shown in table A.1. Then an individual linear background is subtracted by connecting the beginning and end of the respective field window. Lastly the integral over the corrected feature is calculated by using the composite trapezoidal rule as implemented in NumPy [56]. At $\nu = 312.8\,\mathrm{GHz}$ the substructure of features B to F were integrated over for each resonance feature, because a clear separation was not always plausible and practical.

The intensities of resonance features A and B decrease with increasing temperature at all measured frequencies and are very pronounced in the spectra recorded at $T = 2\,\mathrm{K}$ (figure 4.7). This leads to the conclusion that these resonances originate from the systems ground state, or at least states energetically close to the ground state. At $\nu = 75.9\mathrm{GHz}$ (figure 4.11) the other three visible peaks C,D and E, located between A and B, show an increase in intensity up to $T \approx 13\,\mathrm{K}{-}20\,\mathrm{K}$ (see figure 4.14(a)), which is characteristic for transitions between exited states. The intensity evolution of the resonance features C and D appear to be almost identical at $\nu = 75.9\,\mathrm{GHz}$ and similar at $\nu = 312.8\,\mathrm{GHz}$ and $\nu = 522.0\,\mathrm{GHz}$. At $\nu = 75.9\,\mathrm{GHz}$ both resonance features behave like they arise from transitions between exited states, i.e. their intensity first increases with temperature from $T = 2\,\mathrm{K}$ and decreases for $T > 20\,\mathrm{K}$. Likewise this also occurs at $\nu = 312.8\,\mathrm{GHz}$, although the magnitude of signal itself and the intensity changes are considerably weaker. The features reach their maximum intensity around $T \approx 8\,\mathrm{K}$ which is quite a bit lower than for $\nu = 75.9\,\mathrm{GHz}$ where this occurs in the range of $16\,\mathrm{K} \lesssim T \lesssim 20\,\mathrm{K}$. At $\nu = 522.0\,\mathrm{GHz}$ on the other hand both features behave like transitions originating from a ground state. This could be explained by considering that at $B_\mathrm{c} \approx 8.3\,\mathrm{T}$ there is a change in ground states as a function of magnetic field, as observed in the isothermal magnetization (see figure 4.3(b)). Thus the initial state of the resonance features C and D is now the ground state or states lying energetically close to it.

For branches E and F it was already proposed from the frequency dependence data, that these transitions originate from the new ground state for $B \gtrsim B_\mathrm{c}$. At $\nu = 75.9\,\mathrm{GHz}$ both features are not visible, but at $\nu = 312.8\,\mathrm{GHz}$ the peaks comprising E and F behave like transitions between exited states (see figure 4.12(b) and 4.14(b)). At $\nu = 522.0\,\mathrm{GHz}$ their intensities decrease as a function of temperature as expected of a ground state transition. This supports the previous hypothesis, since at $\nu = 522.0\,\mathrm{GHz}$ features E and F occur at magnetic fields greater than B_c. Branch G is not visible at the three frequencies for which temperature sweeps were performed and branch H only once at $\nu = 522.0\,\mathrm{GHz}$ and only quite faintly there. Nevertheless H exhibits the behavior typical of a transition between exited states.

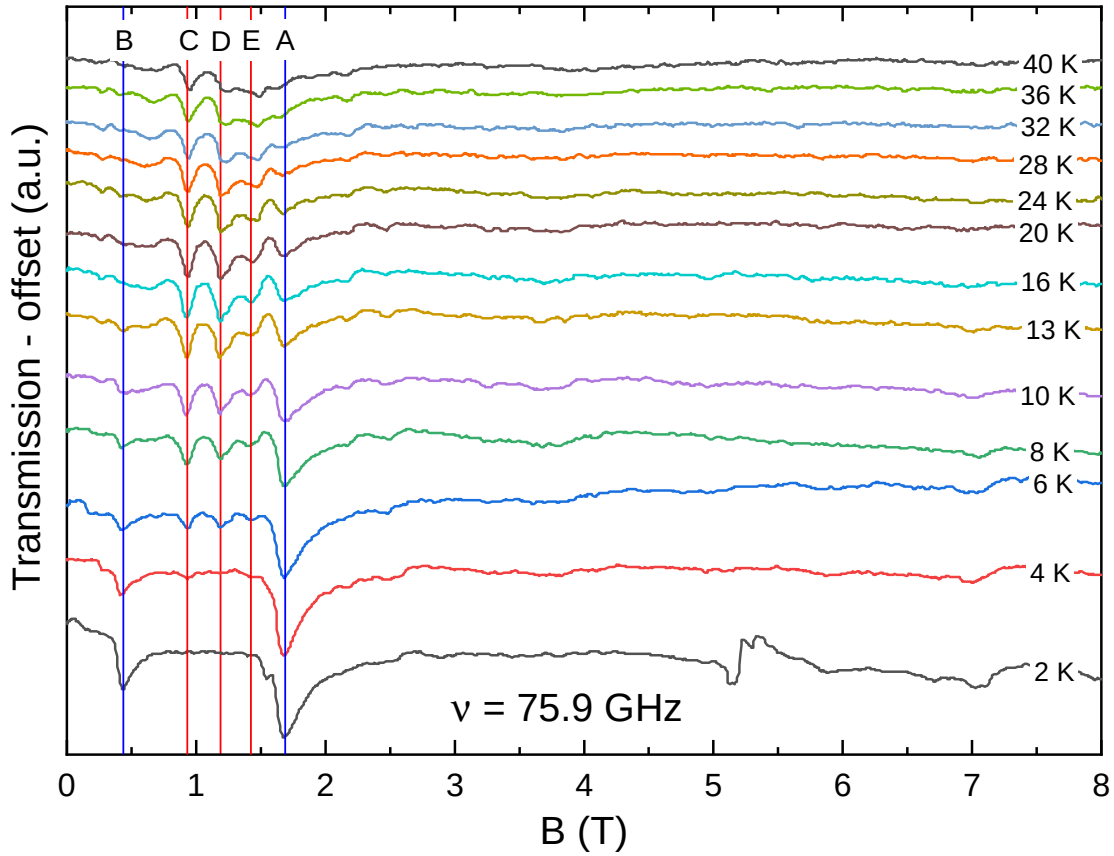


Figure 4.11: HF-ESR spectra (down-sweeps) recorded at a microwave frequency of $\nu = 75.9\,\text{GHz}$ and for different temperatures. The spectra are not phase-corrected. The positions of observed resonances are marked by vertical lines, which are red if the respective resonance is believed to be a transition between two exited states and blue if it originates from the ground state. The measurement was performed on a sample of fixed CoΔ powder.

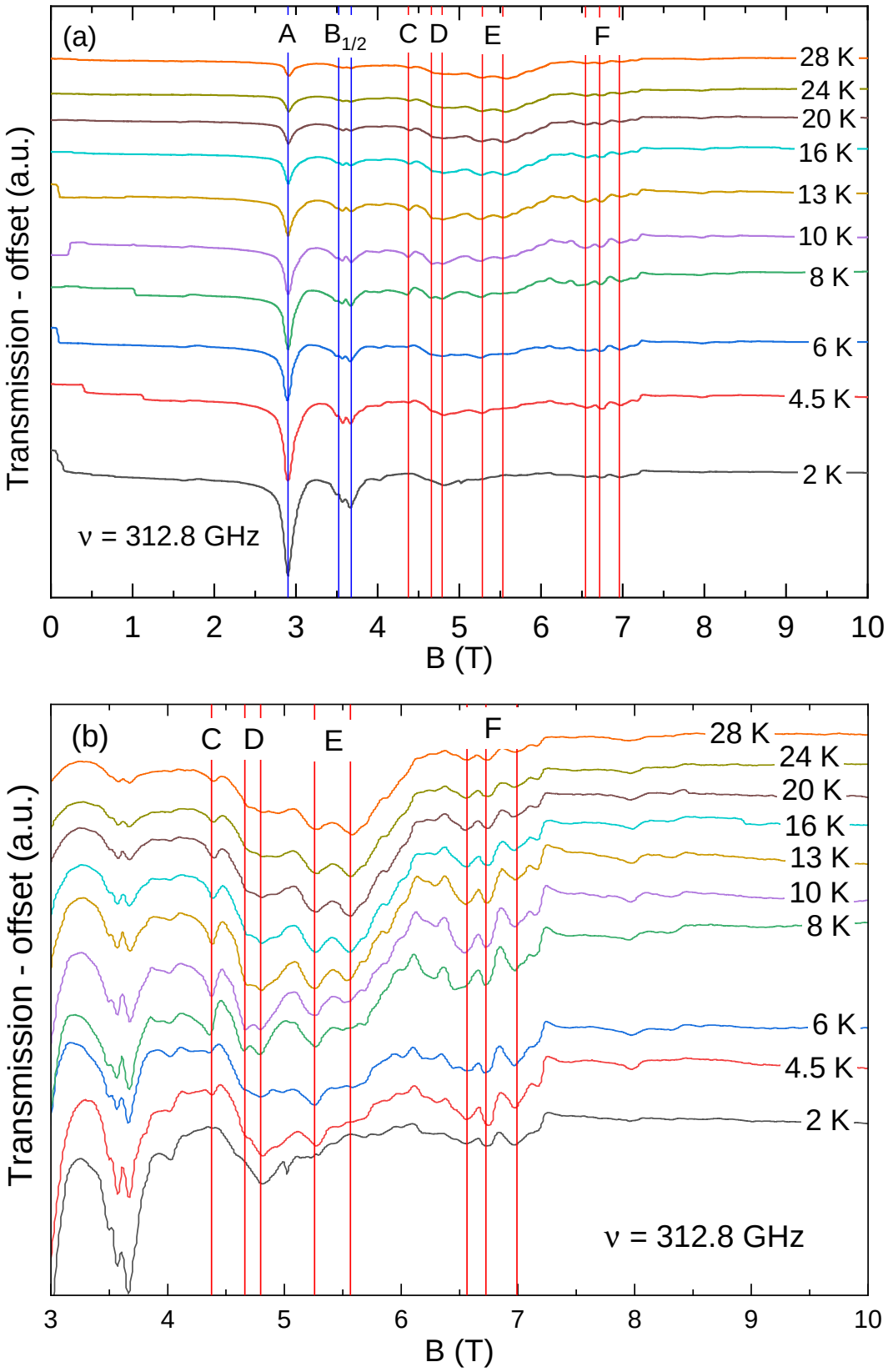


Figure 4.12: (a) HF-ESR spectra (down-sweeps) recorded at a microwave frequency of $\nu = 312.8\,\mathrm{GHz}$ and for different temperatures. (b) Zoomed in version of (a). The spectra are not phase-corrected. The positions of observed resonances are marked by vertical lines, which are red if the respective resonance is believed to be a transition between two exited states and blue if it originates from the ground state. The measurement was performed on a sample of fixed CoΔ powder.

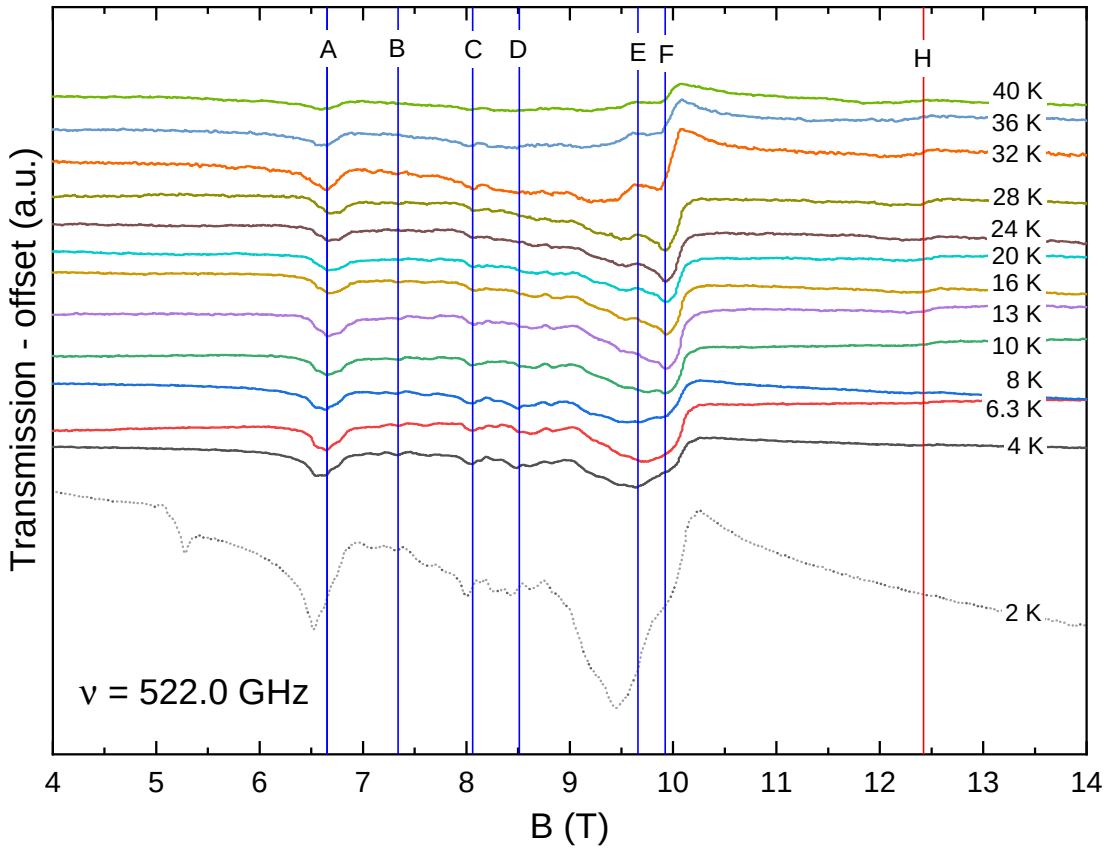


Figure 4.13: HF-ESR spectra (down-sweeps) recorded at a microwave frequency of $\nu = 522.0\,\mathrm{GHz}$ and for different temperatures. The spectra are not phase-corrected. The positions of observed resonances are marked by vertical lines, which are red if the respective resonance is believed to be a transition between two exited states and blue if it originates from the ground state. The measurement was performed on a sample of fixed CoΔ powder.

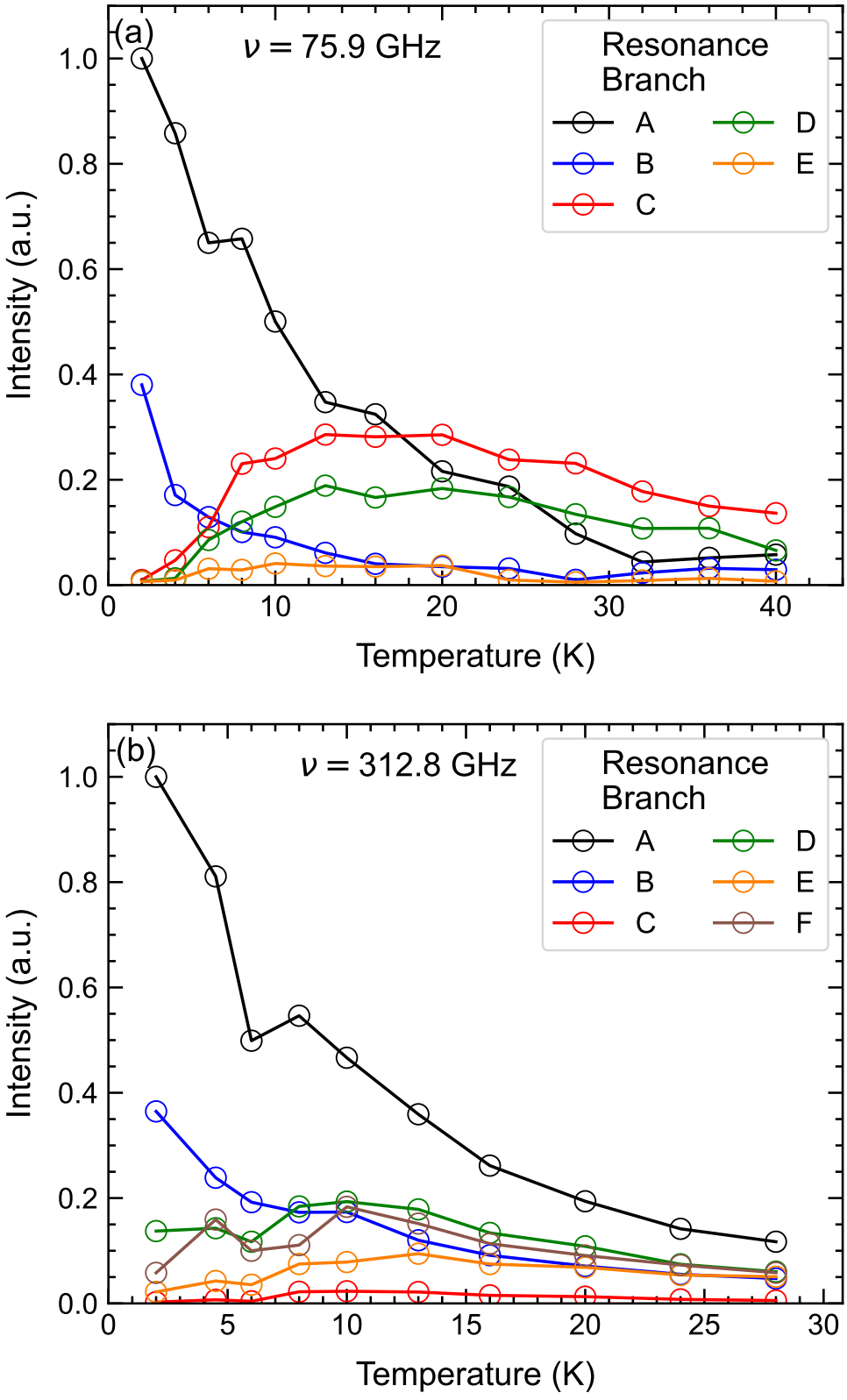


Figure 4.14: Intensities of the resonance features observed at a microwave frequency of (a) $\nu = 75.9\,\mathrm{GHz}$ and (b) $\nu = 312.8\,\mathrm{GHz}$. The corresponding spectra are displayed in figures 4.12 and 4.11. The intensities were determined by subtracting a linear background from each peak and then integrating over them. The absolute value of these integrals is shown here. The measurement was performed on a sample of fixed CoΔ powder.

4.2 Copper Triangle: $NMe_4[Cu_3(\mu_3\text{-}F)(TFA)_6(Py)_3]$

4.2.1 Structure

$NMe_4[Cu_3(\mu_3\text{-}F)(TFA)_6(Py)_3]$ (CuΔ) crystallizes in the trigonal space group $R3_c$ (161) with lattice parameters $a = b = 12.1811(4)\,\text{Å}$ and $c = 50.558(2)\,\text{Å}$ [46]. The structure can be separated into solvent cations $[NMe_4]^+$ and tri-nuclear complex anions $[Cu_3(\mu_3\text{-}F)(TFA)_6(Py)_3]^-$. In figure 4.15(a) the crystal structure is displayed and close ups on the formula unit, i.e. the solvent $[NMe_4]^+$ and molecule $[Cu_3(\mu_3\text{-}F)(TFA)_6(Py)_3]^-$ are plotted in figures 4.15(b) and 4.15(c) respectively. The smallest distance between the central fluorine atoms of neighboring molecules located in one unit cell is $d_{\text{inter:F-F}} = 10.976\,\text{Å}$ and the distance of the closest copper ions between the two molecules is $d_{\text{inter:Cu-Cu}} = 9.384\,\text{Å}$. The copper ions are in the Cu^{2+} ionization state and therefore in a $3d^9$ electronic configuration. In this configuration the Cu^{2+} hosts one hole in the $3d$ shell, meaning that their spin state is $S = \frac{1}{2}$.

The complex anion exhibits a C_3 point group symmetry, with the C_3 axis pointing through the central fluorine (μ_3-F). This high-symmetry axis lies perpendicular to the plane spanned by the three magnetically active copper ions. These ions have a distance of $d(\text{Cu-Cu}) = 3.427\,\text{Å}$ between each other and a distance of $d(\text{Cu-F}) = 1.987\,\text{Å}$ to the central fluorine. Locally, the copper ions are coordinated by four oxygen atoms, one nitrogen atom and the μ_3-F. For reference see figure 4.15(d). When only considering their nearest neighbors the atomic environment of the Cu^{2+}-ions show no local symmetry, i.e. the C_1 point group. To some degree of approximation one could alternatively consider the local environment of the copper ions to exhibit a C_{2v} symmetry, with the C_2 axis pointing along the N-Cu-F bond. However, this is only approximately true since the the N-Cu-F bond angle differs from 180°, i.e. $\sphericalangle(\text{N-Cu-F}) = 175.74°$ and the bond angles between two neighboring oxygen atoms and the copper ions deviate from 90° as $\sphericalangle(\text{O}_0\text{-Cu-O}_1) = 90.37°$, $\sphericalangle(\text{O}_1\text{-Cu-O}_2) = 83.48°$, $\sphericalangle(\text{O}_2\text{-Cu-O}_3) = 98.58°$ and $\sphericalangle(\text{O}_3\text{-Cu-O}_0) = 87.46°$.

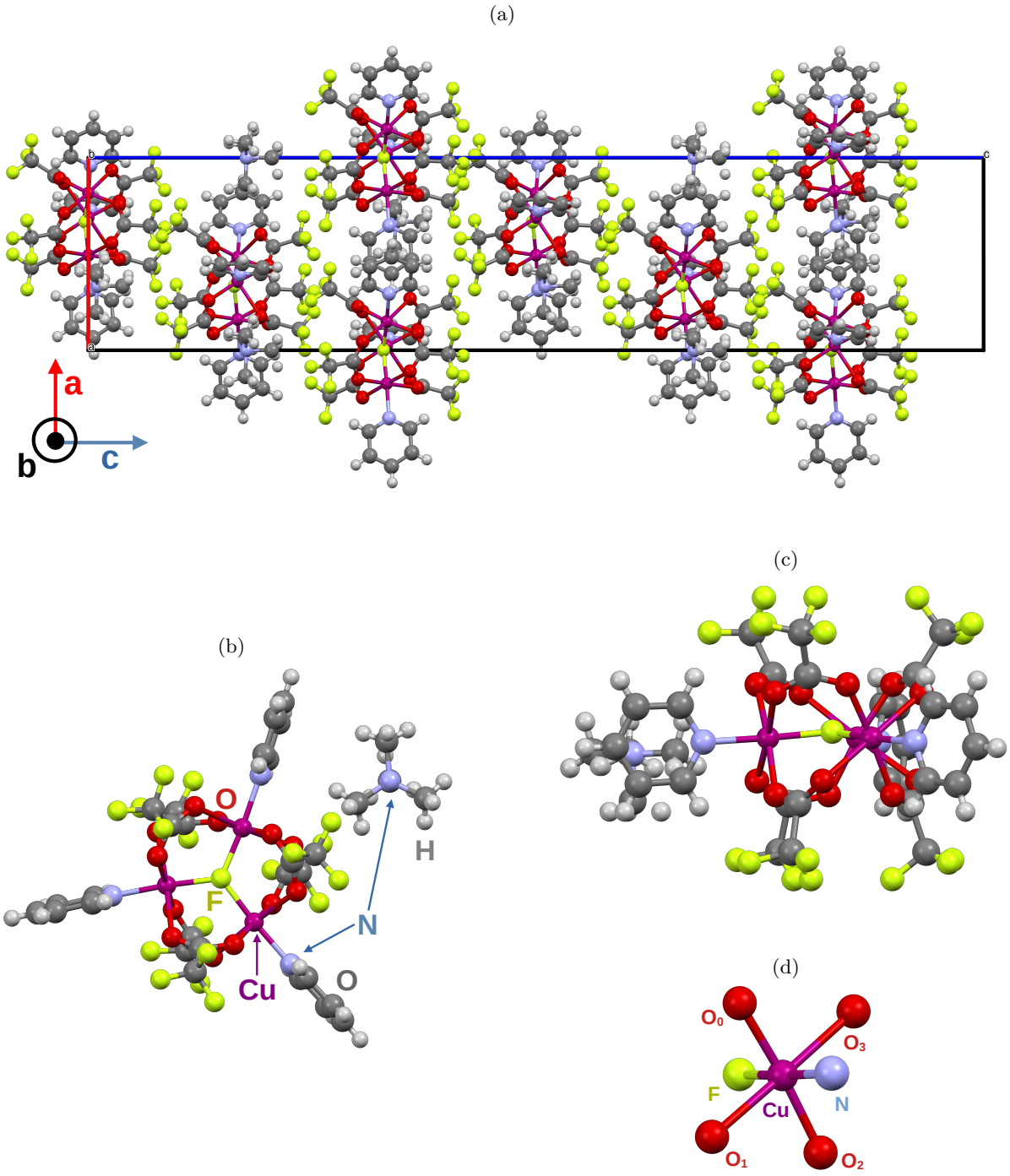


Figure 4.15: Depiction of the crystal structure of CuΔ: (a) Crystal structure of CuΔ viewed along the *b*-axis. Only molecules with their center of mass lying in the unit cell are displayed in their entirety. In (b) and (c) one formula unit including the solvent and molecular part of the crystal is displayed. (d) Local Cu^{2+} environment, i.e. the nearest neighbors, including the oxygen atoms, which are numerated counter clockwise starting from O_0. Crystallographic data was provided by [46] and displayed using *Mercury* [47].

4.2.2 Room Temperature X-Band ESR Studies

Room temperature ($T \approx 293\,\mathrm{K}$) X-Band ESR measurements were carried out on a fixed powder sample of CuΔ. The sample was previously used in HF-ESR measurements, then transferred into the PPMS for magnetization measurements and finally inserted into the X-Band ESR tube. Additionally, the X-Band ESR signal of an empty sample holder was determined, so that sample's spectrum could be background-corrected. In figure 4.16 the corrected X-Band ESR spectrum of the sample is plotted. The observed resonance features are labeled as $\mathrm{x}_i, 1 \leq i \leq 6$. Resonance features $\mathrm{x}_{2\ldots5}$ appear to arise from hyperfine interaction. x_5 is only visible as a shoulder of the most prevalent feature x_6. The main feature x_6 is asymmetrical, i.e. lob-sided towards higher fields, which is indicative of an axial type anisotropy of the g-factor ($g_{||} > g_{\perp}$). The presence of x_1 is unexpected, due to it's position corresponding an effective g-factor of $g_1 \approx 4.4$. This is surprising, since one expects the ambient temperature to dominate the energy scale of interactions (see section 4.2.3) and that, therefore, only the features corresponding to the isolated Co^{2+}-ions (in a crystal field) should be visible. The nature of this feature is currently unknown.

A spin Hamiltonian of an isolated Cu^{2+} ($S = 1/2$) is fitted to the remaining features ($x_{2..6}$). This Hamiltonian reads

$$H_{\text{X-ESR}} = \mu_B(g_{||}B_\mathrm{z}S_\mathrm{z} + g_{\perp}(B_\mathrm{x}S_\mathrm{x} + B_\mathrm{y}S_\mathrm{y})) + A_{||}S_\mathrm{z}I_\mathrm{z} + A_{\perp}(S_\mathrm{x}I_\mathrm{x} + S_\mathrm{y}I_\mathrm{y})\,, \tag{4.10}$$

where the hyperfine coupling constants are denoted by $A_{||}$ and $A_{\perp}$ and the nuclear spin by $I_{i\in\{\mathrm{x,y,z}\}}$. The fit was performed using *EasySpin* (version 6.0.0-dev51) [53] on the B-Field range shown in figure 4.17. In this figure the best fit is displayed as a solid green line. The best fit parameters are shown in table 4.4. The obtained g-tensor yields a solid angle averaged g-factor of $\langle g\rangle_\Omega = 2.151(3)$.

Parameter	Best Fit Value
$g_{||}$	2.3181(13)
$g_{\perp}$	2.065(7)
$A_{||}$	$-495(5)$ MHz
$A_{\perp}$	54(3) MHz

Table 4.4: g-factors and hyperfine interaction parameters of CuΔ as determined by fitting the spin Hamiltonian (equation 4.10) to the room temperature X-ESR spectrum (see figure 4.17). The fit was performed using *EasySpin* [53]. The errors depicted here are purely fit errors, i.e. the square root of the covariance matrix generated by *EasySpin*.

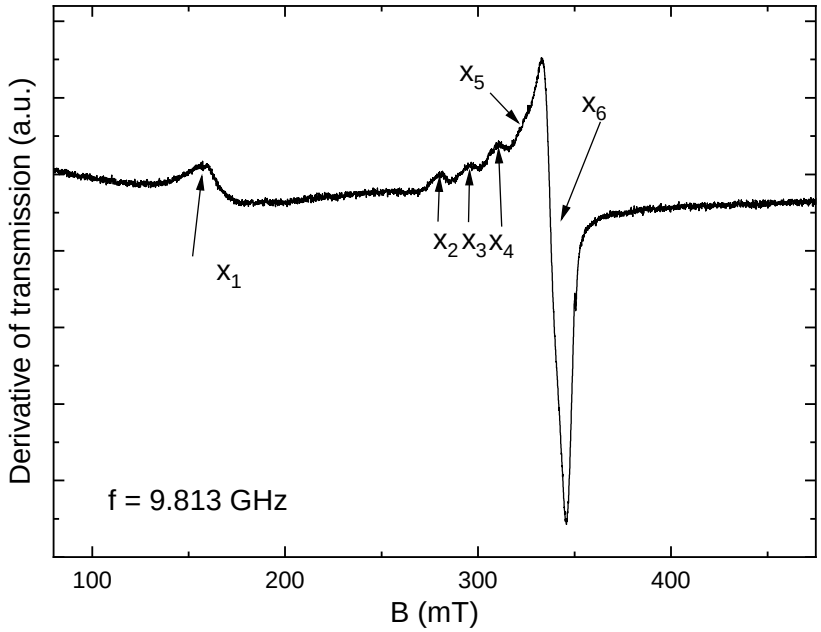


Figure 4.16: Room temperature X-Band ESR spectrum of a fixed powder sample of CuΔ . Resonance features are denoted by $x_{i\in\mathbb{N}}$

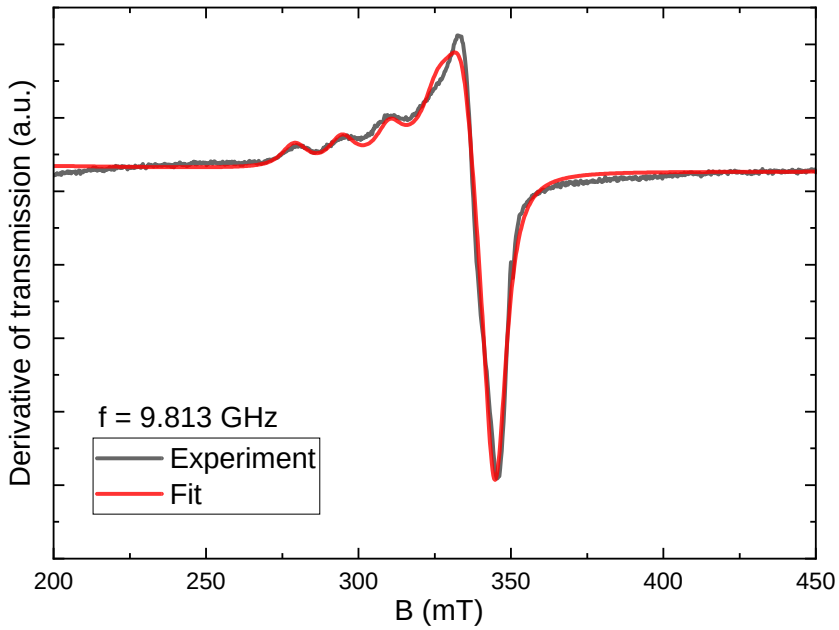


Figure 4.17: Room temperature X-Band ESR spectrum (green) of a fixed powder sample of CuΔ overlayed with the best fit using equation 4.10 (gray). The fitting parameters are given in table 4.4.

4.2.3 Static Magnetic Properties

Measurement and Data

Static magnetic properties of a fixed powder sample of CuΔ with a mass of $m = 10.4(3)\,\mathrm{mg}$ were measured by *A. Elghandour* [48] using the PPMS and (primarily) the MPMS (see section 2.1). The static magnetization of the empty container M_{SH} was measured at $B = 0.1\,\mathrm{T}$ and temperatures in the range of $1.8\,\mathrm{K} \leq T \leq 400\,\mathrm{K}$ (see figure A.1), so that measurements of the sample could be corrected for the putative background of the sample holder. Additionally, the measured magnetization M_{M} was corrected for the diamagnetic contribution of the sample itself (see section 2.1).

The $\chi T(B,T) = \frac{M(T,B)}{B}T$ curves measured at $B = 0.1\,\mathrm{T}$ are plotted in figure 4.18 for the DC option and for the VSM option. In the inset VSM $\chi T(B,T)$ data at $B = 7\,\mathrm{T}$ is shown. χT increases when cooling from the high-temperature regime $\chi T(T \gtrsim 175\mathrm{K})$, leading to the conclusion that the copper spins are ferromagnetically coupled. In said high-temperature regime $\chi T(T \gtrsim 175\mathrm{K})$ asymptotically approaches a constant (or linear) functional dependence $\chi T \searrow \chi_{\mathrm{DC}}T(T \to 300\mathrm{K})$. However, as indicated, differ the behaviors of the two curves measured with the DC and VSM option. The DC measurement of χT indeed approaches a constant value of $\chi_{\mathrm{DC}}T(T \to 300\mathrm{K}) = 1.668(9)\frac{\mathrm{ergK}}{\mathrm{G^2mol}}$. While $\chi_{\mathrm{VSM}}T$ for the VSM measurements shows a linear increase for $T \gtrsim 175\mathrm{K}$. This increase can be attributed to an overestimation of the applied corrections to the VSM mode. To compensate for this, fits to this data set include an additional temperature-independent correction term χ_0 as a fitting parameter. From the high-temperature limit of $\chi_{\mathrm{DC}}T$ the solid angle averaged g-factor from it (using equation 4.3) yields $\langle g \rangle_\Omega = 2.44(6)$ for the DC-option, which is inconsistent with the value obtained from X-Band ESR measurements and significantly higher than the usually observed g-factors for copper [57, 58, 59, 10]. This most presumingly indicates, that a systematic error occurred during the determination of the sample's mass. It will be shown in the next subsection that the large g-factor can be explained by an overestimation of the mass by roughly 23%.

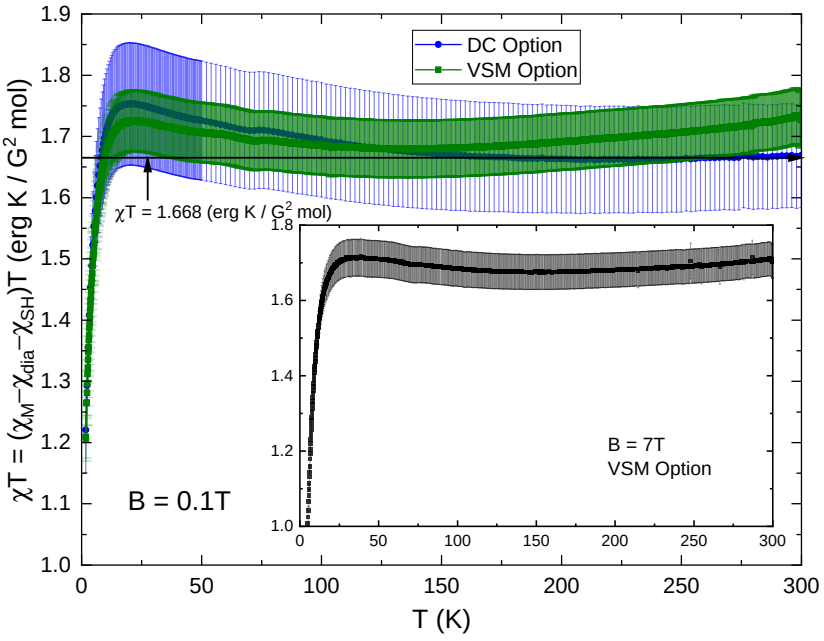


Figure 4.18: Static magnetic susceptibility of CuΔ measured in the MPMS's DC and VSM modes. The measurement was performed by *A. Elghandour* [48] at $B = 100\,\mathrm{mT}$ and $B = 7\,\mathrm{T}$ (inset). The data was corrected for the samples diamagnetic contribution and the empty sample holders contribution.

Isothermal magnetization $M(B, T = \text{const})$ curves, measured in the MPMS for fields up to $B = 7\,\text{T}$, can be seen in figure 4.19(a). $M(B, T = \text{const})$ increases monotonically for increasing field strength, while the derivative of the isothermal magnetization (see figure 4.19(b)) decreases asymptotically. The anomalies at $T = 1.8\,\text{K}$ ($B \approx 2.5\,\text{T}$) and at $T = 2\,\text{K}$ ($B \approx 1\,\text{T}$) cannot be seen at different temperatures, leading to the conclusion that they are artifacts of the measurement and not intrinsic features. For magnetic fields up to $B = 14\text{T}$ the same behavior of monotonically increasing and asymptotically decreasing can be observed for the isothermal magnetization and for it's derivative (see figure 4.20). These measurements were performed in the PPMS. The PPMS measurement had to be performed with a sample, that was previously used in the fixed powder HF-ESR measurements. This means, that it was contaminated with an unknown quantity of H-Vacuum grease and therefore it's mass could not be determined. To work around this issue, the PPMS data was scaled to fit the MPMS data up to $B = 7\,\text{T}$. The lack of any discernible step-like features, like the ones observed for CoΔ, in the isothermal magnetization (figures 4.19(a) and 4.20(a)) or maxima/minima in it's derivative (figures 4.19(b) and 4.20(b)) supports the conclusion of either uncoupled or ferromagnetically coupled spins in CuΔ.

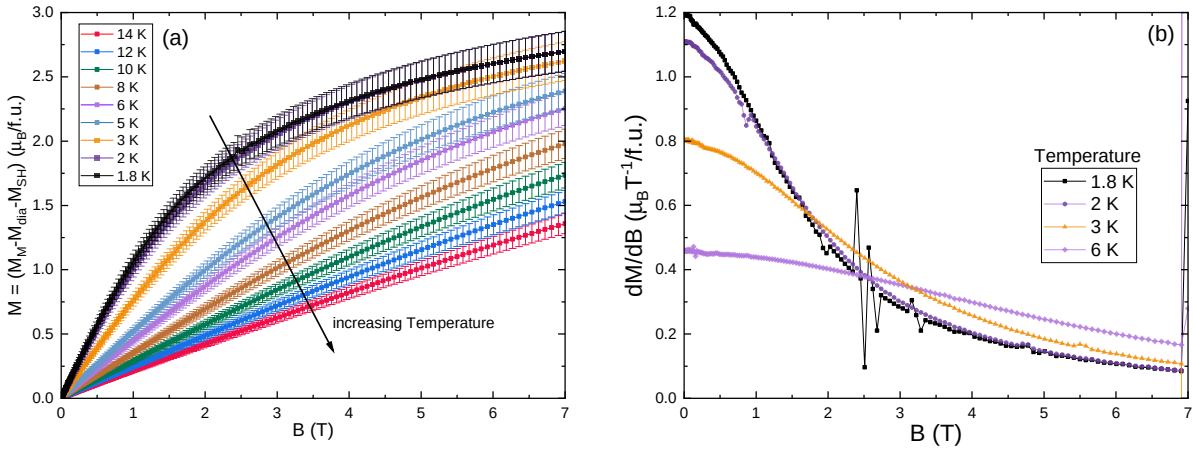


Figure 4.19: (a) Isothermal magnetization $M(B)$ of CuΔ measured by *A. Elghandour* [48] for temperatures in the range from 1.8 K to 14 K. (b) Derivative of $M(B)$ with respect to the magnetic field B. The data are corrected for the contribution of an empty sample holder and for the systems diamagnetic contribution (see equations 2.2 and 2.5).

In figure 4.21 simulated $M(B)$ curves for three free spins with different g-factors are overlayed over the isothermal magnetization measured at $T = 2\,\text{K}$. One can observe that the experimentally determined isothermal magnetization is suppressed well below the calculated magnetization for $g = 2.44$ (i.e. for the g-factor obtained from the χT data). Since the mass overestimation affects χT and $M(B)$ in the same way, one would expect that $M(B)$ of CuΔ saturates at least as quickly as free spins (ferromagnetic coupling). This points to the relevance of magnetic anisotropy in CuΔ, which is necessarily governed by the anisotropy of the spin-spin interactions, since SIA only leads to a total shift of the system's total energy, due to $S_{\text{Cu(II)}} = 1/2$. The relevance of magnetic anisotropy is also indicated by χT decreasing for lower temperatures, which can be attributed to such a competition of anisotropic and ferromagnetic interactions (see fitting). This decrease of χT occurs before a maximum at $T_{\text{max}}^{\text{DC}} = 20.3(5)\text{K}$ for the DC option and $T_{\text{max}}^{\text{VSM}} = 21.20(6)\text{K}$ for the VSM option. It has to be noted that the position of this maximum is influenced by the applied corrections, giving a possible explanation of the difference between the two data sets.

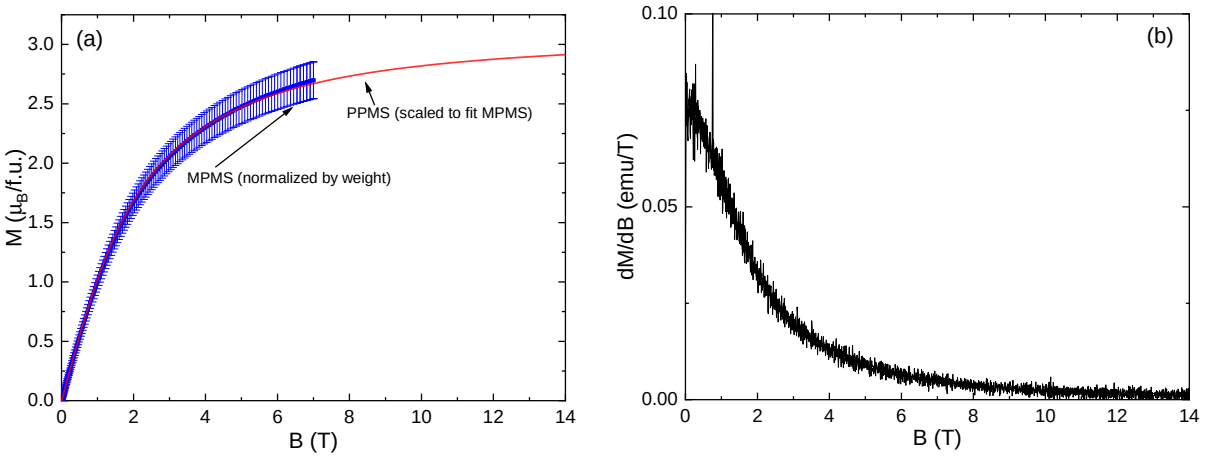


Figure 4.20: (a) Comparison of isothermal Magnetization $M(B)$ of CuΔ measured at $T = 2\,\mathrm{K}$ by *A. Elghandour* [48] using the MPMS (blue dots with error bars) and PPMS (solid line). Due to an unknown mass of the sample used in the PPMS the PPMS data was scaled to fit the MPMS data. (b) Derivative of $M(B)$ with respect to the magnetic field B (PPMS) at $T = 2K$.

Spin Hamiltonian Fitting

In order to check and quantify the conclusions drawn from qualitative discussion of the magnetization data, the fitting of a spin Hamiltonian is performed. The employed spin-Hamiltonian has the following form

$$H_{\mathrm{SH}} := \sum_{i=0,j>i} \vec{S}_i^{\dagger} \underline{\underline{J}}^{i,j} \vec{S}_j + \sum_i \mu_B \vec{B}^{\dagger} \underline{\underline{g}}^i \vec{S}_i \,. \tag{4.11}$$

A first reduction of parameters can be achieved by exploiting the C_3 symmetry axis of the molecule via

$$H_{\mathrm{SH}} := \sum_i \vec{S}_i^{\dagger} (\underline{\underline{R}}^{\dagger})^i \underline{\underline{J}}^{0,1} \underline{\underline{R}}^i \vec{S}_{i+1 \bmod 3} + \sum_i \mu_B \vec{B}^{\dagger} (\underline{\underline{R}}^{\dagger})^i \underline{\underline{g}}^0 \underline{\underline{R}}^i \vec{S}_i \,. \tag{4.12}$$

Here $\underline{\underline{R}}$ represents a rotation matrix rotating the reference frame by 120° around the c-axis. As a next step $\underline{\underline{g}}^0$ is constructed using the fit results from the room-temperature X-Band ESR measurement. The principle axis is assumed to lie along the F-Cu-N bonds with $g_{||} = 2.3181(13)$ and $g_{\perp} = 2.065(7)$. In that way only the nine parameters for the spin-spin interaction term, χ_0 and the mass correction scaling f_{m} remain. The parameters for the spin-spin interaction terms are further reduced by decomposing $\underline{\underline{J}}^0$ into it's $l = 0, 1, 2$ irreducible representations, namely the isotropic-, DM- and Kitaev-exchange. These tenors are taken from the *ab-initio* calculations described in chapter 5 and scaling factors for each part are taken as fitting parameters. This is done with the assumption, that the symmetries of the system and thereby the spin-spin interaction are captured by the *ab-initio* calculations, justifying the way they are employed here. This reduces the total amount of fitting parameters to five. These are the isotropic exchange J_{iso}, magnitude of DMI $||\underline{\underline{D}}||_2 =: f_{\mathrm{DMI}}$ and Kitaev interaction $||\underline{\underline{K}}||_2 =: f_{\mathrm{K}}$ as well as χ_0 and f_{m}. $||\underline{\underline{O}}||_2$ with $O \in \mathcal{L}(\mathbb{C}^n), n \in \mathbb{N}$ represents the operator 2-norm here. This results in the final spin Hamiltonian used for the fitting:

$$H_{\mathrm{SH}} = \sum_i \vec{S}_i^{\dagger} (\underline{\underline{R}}^{\dagger})^i (J_{\mathrm{iso}} + f_{\mathrm{DMI}} \underline{\underline{D}}^{\mathrm{ai}} + f_{\mathrm{K}} \underline{\underline{K}}^{\mathrm{ai}}) \underline{\underline{R}}^i \vec{S}_{i+1 \bmod 3} + \sum_i \mu_B \vec{B}^{\dagger} (\underline{\underline{R}}^{\dagger})^i \underline{\underline{g}}^{\text{X-Band ESR}} \underline{\underline{R}}^i \vec{S}_i \,, \tag{4.13}$$

where $\underline{\underline{D}}^{\mathrm{ai}}$ and $\underline{\underline{K}}^{\mathrm{ai}}$ represent the normalized (using the operator 2-norm) DMI and Kitaev interaction terms obtained from the *ab-initio* calculations. The VSM-χT data at $B = 100\mathrm{mT}$ as well as the $M(B)$ data at $T \in \{2\mathrm{K}, 5\mathrm{K}, 10\mathrm{K}\}$ were fitted simultaneously using *EasySpin* (version 6.0.0-dev51) [53]. The

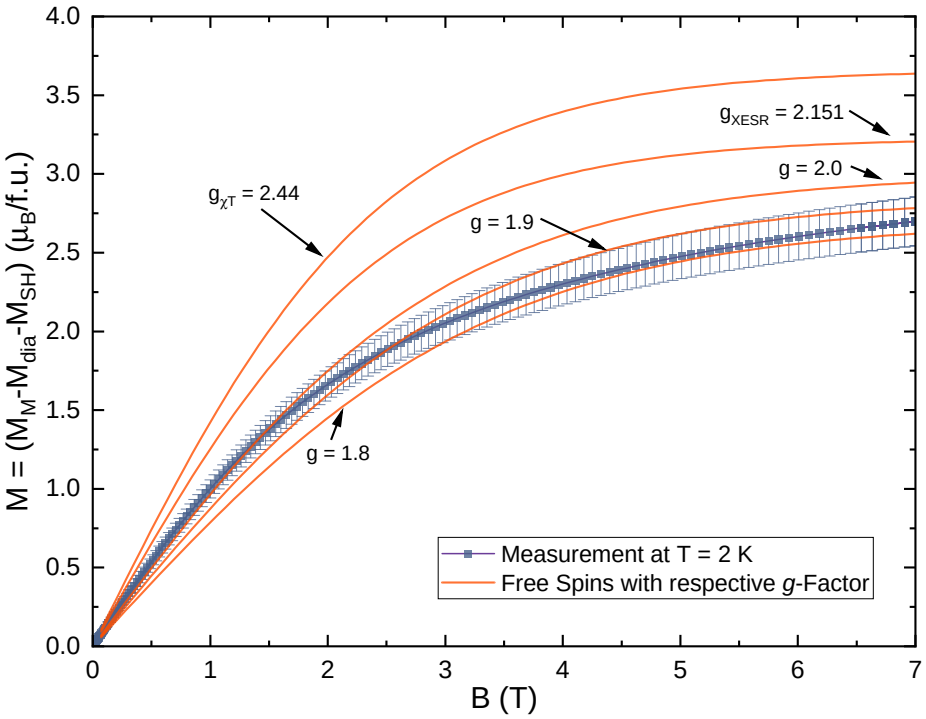


Figure 4.21: Magnetization curve of CuΔ as seen in figure 4.19(a) for $T = 2\,\mathrm{K}$. The solid lines depict the expected magnetization curves for three free spin $\frac{1}{2}$ spins for different g-factors, as indicated in in the labels. Two of the used g-factors are the solid angle averages obtained from the DC χT measurement $g_{\chi\mathrm{T}} = 2.44(6)$ and the X-Band ESR measurement $g_{\mathrm{XESR}} = 2.151(3)$.

best fit parameters are shown in table 4.5 and the fitted curves are plotted in figures 4.22(a) and 4.22(b). With these parameters the DM-interaction in vector representation is given as

$$\vec{D}/\,\mathrm{K} = \begin{pmatrix} 2.2 \\ -0.3 \\ -3.9 \end{pmatrix}, \tag{4.14}$$

and the Kitaev-exchange is given in matrix form as

$$\underline{\underline{K}}/\,\mathrm{K} = \begin{pmatrix} -2.7 & 5.5 & -14.4 \\ 5.5 & -12.1 & 13.3 \\ -14.4 & 13.3 & 14.8 \end{pmatrix}. \tag{4.15}$$

The reference system here is chosen in such a way that the z-axis corresponds to the molecules c-axis and that the x-axis points along one of the N-Cu-F bonds towards the center of the molecule. $\underline{\underline{K}}$ has eigenvalues $\lambda/\,\mathrm{K} \in \{-23.7, -1.5, 25.3\}$. With the highest eigenvalue and therefore the preferred spin orientation (not considering DMI) [33] corresponding to the eigenvector

$$\vec{v}_+ = \begin{pmatrix} -0.4030 \\ 0.2531 \\ 0.8795 \end{pmatrix}. \tag{4.16}$$

In the triangle plane this vector has an angle of $\phi = 2.13°$ with respect to the straight line connecting two Cu-ions.

Parameter	Best Fit Value
J_{iso}	$-6.24(16)\,\mathrm{K}$
$\lvert\lvert\underline{\underline{D}}\rvert\rvert_2$	$4.5(4)\,\mathrm{K}$
$\lvert\lvert\underline{\underline{K}}\rvert\rvert_2$	$25.3(4)\,\mathrm{K}$
f_{m}	0.8130(5)
χ_0^{VSM}	$-2.65(4)\cdot 10^{-4}\,\frac{\mathrm{cm}^3}{\mathrm{mol}}$

Table 4.5: Best fit values of the fit parameters for a simultaneous fit to the the experimental $\chi T(T)$ data of CuΔ at $B = 100\,\mathrm{mT}$ (VSM-option) and $M(B)$ data at $T \in \{2\,\mathrm{K}, 5\,\mathrm{K}, 10\,\mathrm{K}\}$. The fit was performed using *easyspin* [53]. The errors depicted here are purely the fit errors, i.e. the square root of the covariance matrix generated by *easypin*.

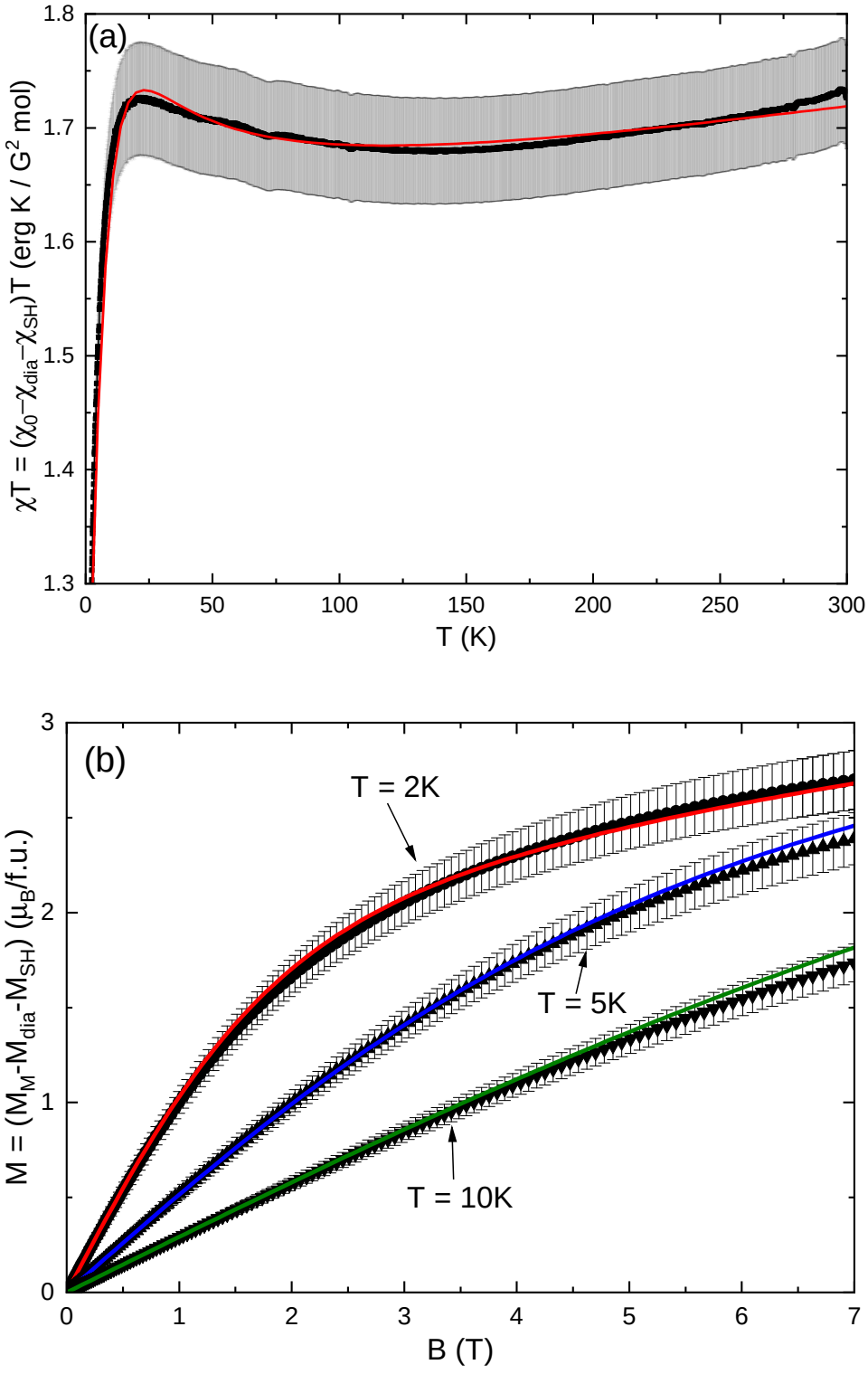


Figure 4.22: (a) Static susceptibility (at $B = 100\,\mathrm{mT}$) and (b) isothermal magnetization of CuΔ (at $T \in 2\,\mathrm{K}, 5\,\mathrm{K}, 10\,\mathrm{K}$) including the fit performed with equation 4.13 and best fit values depicted in table 4.5. The fit was performed using *easyspin* [53]. The data in this figure were measured at a magnetic field of $B = 100\mathrm{mT}$ by *A. Elghandour* [48].

4.2.4 High-Field/High-Frequency ESR Studies

High-Field/High-Frequency ESR measurements were performed on a fixed powder (fixed with H-vacuum grease) as well as a loose powder sample of CoΔ. Recorded spectra for the frequency dependence measurements were phase corrected (see section 2.2), such that the main feature (denoted by A) exhibits little to no phase mixing. The spectra were recorded at $T = 2$K. In general the spectra were processed as outlined in section 4.1.3.

Fixed Powder Measurements

Temperature sweeps were performed at the two frequencies $\nu = 70.1\,\text{GHz}$ (figure 4.23(a)) and $\nu = 228.4\,\text{GHz}$ (figure 4.23(b)). At $\nu = 70.1\,\text{GHz}$ both large features (at $B \approx 1.5\,\text{T}$ and $\approx 2.5\,\text{T}$) (which appear to be an amalgamation of many individual features) decrease in total intensity for higher temperatures. Meaning that the temperature evolution of their intensities behave like resonance features arising from transitions originating from the ground state. Although the cluster of features at roughly $B \approx 2.5\,\text{T}$ (corresponding to $g_{\text{eff}} \approx 2$) is more stable with increasing temperature than the cluster at $B \approx 1.5\,\text{T}$ (corresponding to $g_{\text{eff}} \approx 3.34$). At $\nu = 228.4\,\text{GHz}$ things become more complex, as the previously described clusters appear to have disbanded. However the same trend as for $\nu = 70.1\,\text{GHz}$ can be seen here. The cluster of features at $B \approx 8.2\,\text{T}$ ($g \approx 2$) is again relatively stable with increased temperature when compared to the remaining features. These resonance features with an observed effective g-Factor around $g_{\text{eff}} = 2$ may be attributed to paramagnetic impurities in the sample.

The down-sweep spectra at different microwave frequencies for the fixed powder sample are shown in figure 4.24. As can be seen the spectra are so complex that assignment of features and their tracking becomes impractical. For this reason the loose powder measurements were performed.

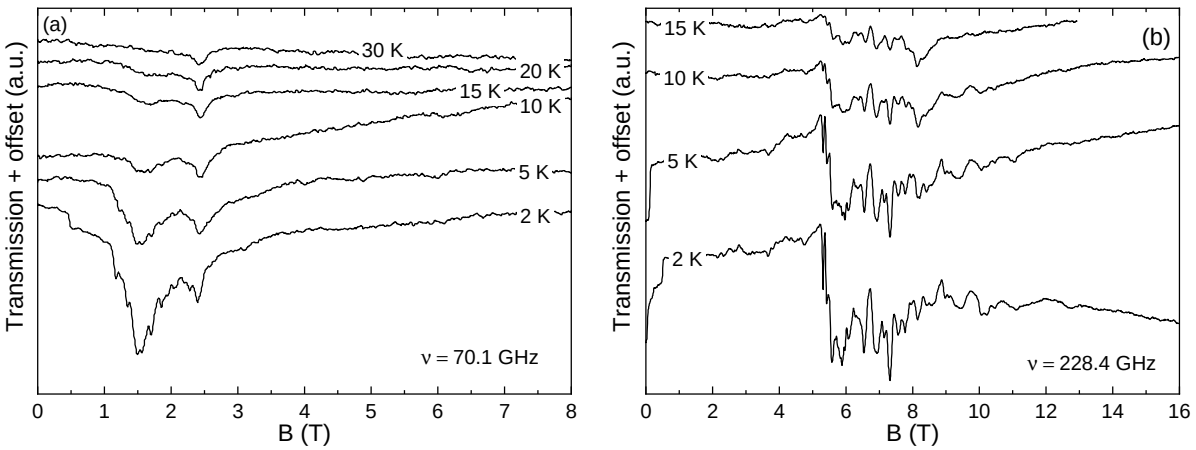


Figure 4.23: HF-ESR transmission spectra (down-sweeps) recorded at different temperatures and at frequencies (a) $\nu = 70.1\,\text{GHz}$ and (b) $\nu = 228.4\,\text{GHz}$. The spectra are not phase corrected. The measurements were performed on a fixed powder sample of CuΔ.

Loose Powder Measurements

To limit the spectral weight of most spatial directions in the measured solid angle averaged spectra the HF-ESR measurements were repeated with a sample of loose powder CuΔ. The CuΔ crystallites were ground up to a fine powder before being inserted into a PEEK container and subsequently the HF-ESR spectrometer. The guiding principle of the loose powder measurement is that the loose kernels will orient

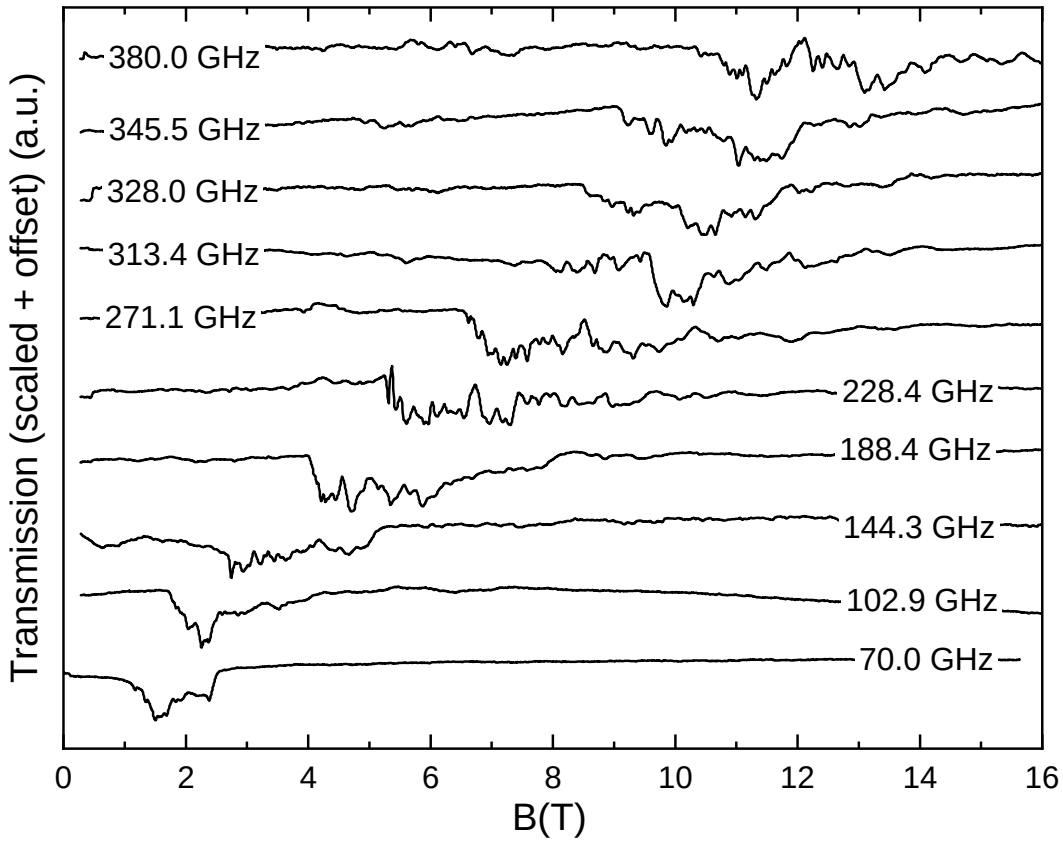


Figure 4.24: Phase corrected HF-ESR transmission spectra (down-sweep) at $T = 2\,\mathrm{K}$. The spectra are shifted and scaled for better clarity of the plot. The measurement was carried out on a fixed powder sample of CuΔ.

themselves in the magnetic field and thereby shift spectral weight to (ideally) only one spatial direction. This yields clearer and less convoluted spectra. In order to ensure alignment, several field sweeps are conducted until the spectra do not change between sweeps. This is done before each measurement session due to the orientations relaxing without an applied field and at higher temperatures during pauses.

The phase corrected spectra at $T = 2\,\mathrm{K}$ are plotted in figures 4.25 (up-sweep) and 4.26 (down-sweep). The observed resonances are marked in these figures by different symbols. There are several pronounced resonance features which will be denoted by A,B, D and E. A and B are close together forming a sort of double feature. Both of these resonance features have a significant amount of spectral weight for all frequencies and dominate the spectrum at low frequencies. Resonance features D and E however get significantly more intense and sharper for higher frequencies ($\nu \gtrsim 300\mathrm{GHz}$). Features of resonance branch C and F have a relatively small amount of spectral weight, when compared to the other features, and disappear for $\nu \gtrsim 250\mathrm{GHz}$. There is also some superstructure and very small features, which appear inconsistently between sweeps and frequencies. These could be explained by an imperfect alignment of the kernels. There is also the aspect of the number of possible ground state transitions for three spin 1/2 being rather limited, so that these features have to originate from somewhere else. Their inconsistent appearance would also speak for some form of misalignment that slightly changes from sweep to sweep.

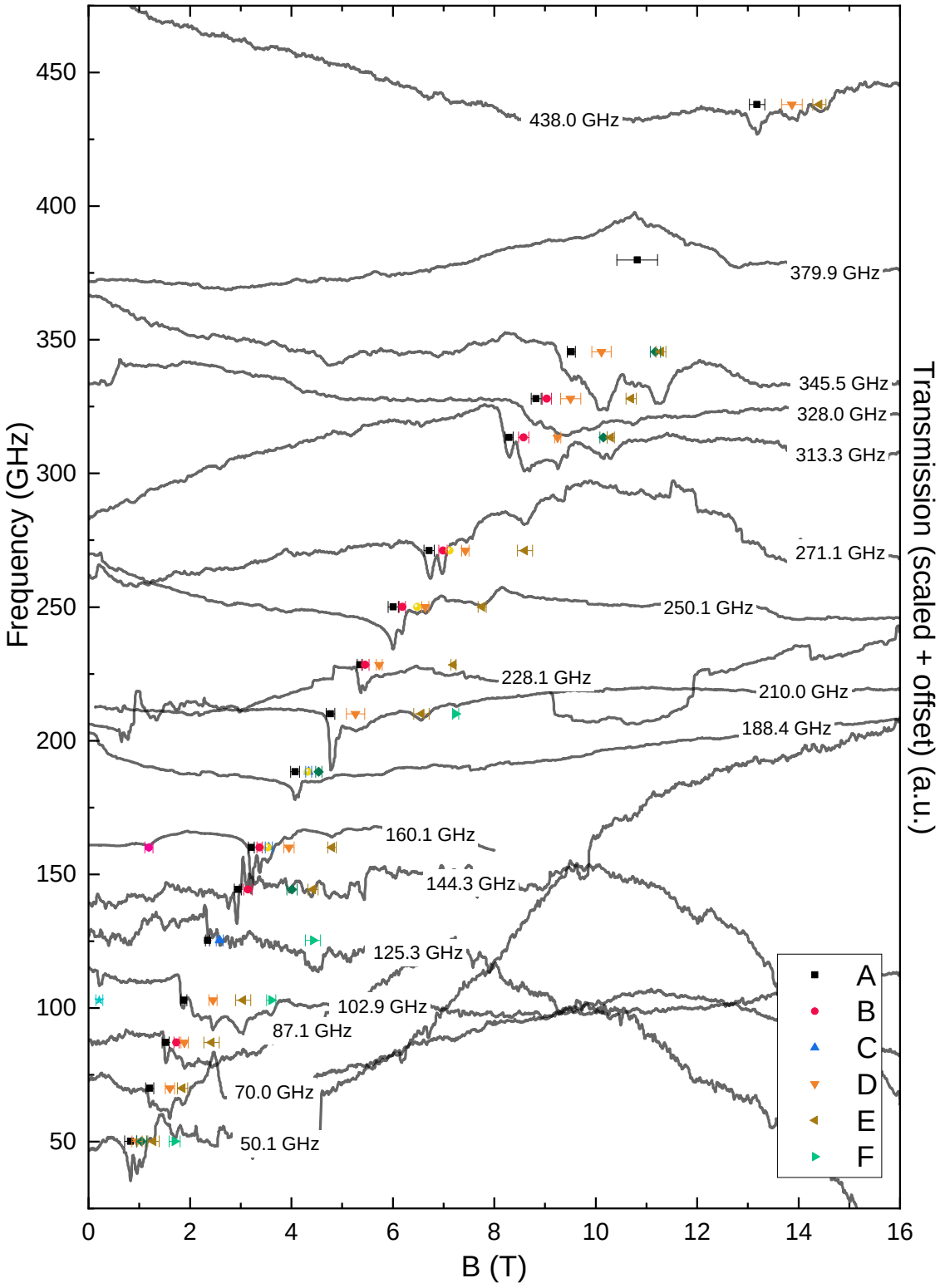


Figure 4.25: Phase corrected HF-ESR transmission spectra (up-sweep) at $T = 2\,\mathrm{K}$. The spectra are shifted and scaled for better clarity of the plot. The observed resonances are marked by the black squares and positioned according to the ordinate on the left. The measurement was carried out on a loose powder sample of CuΔ.

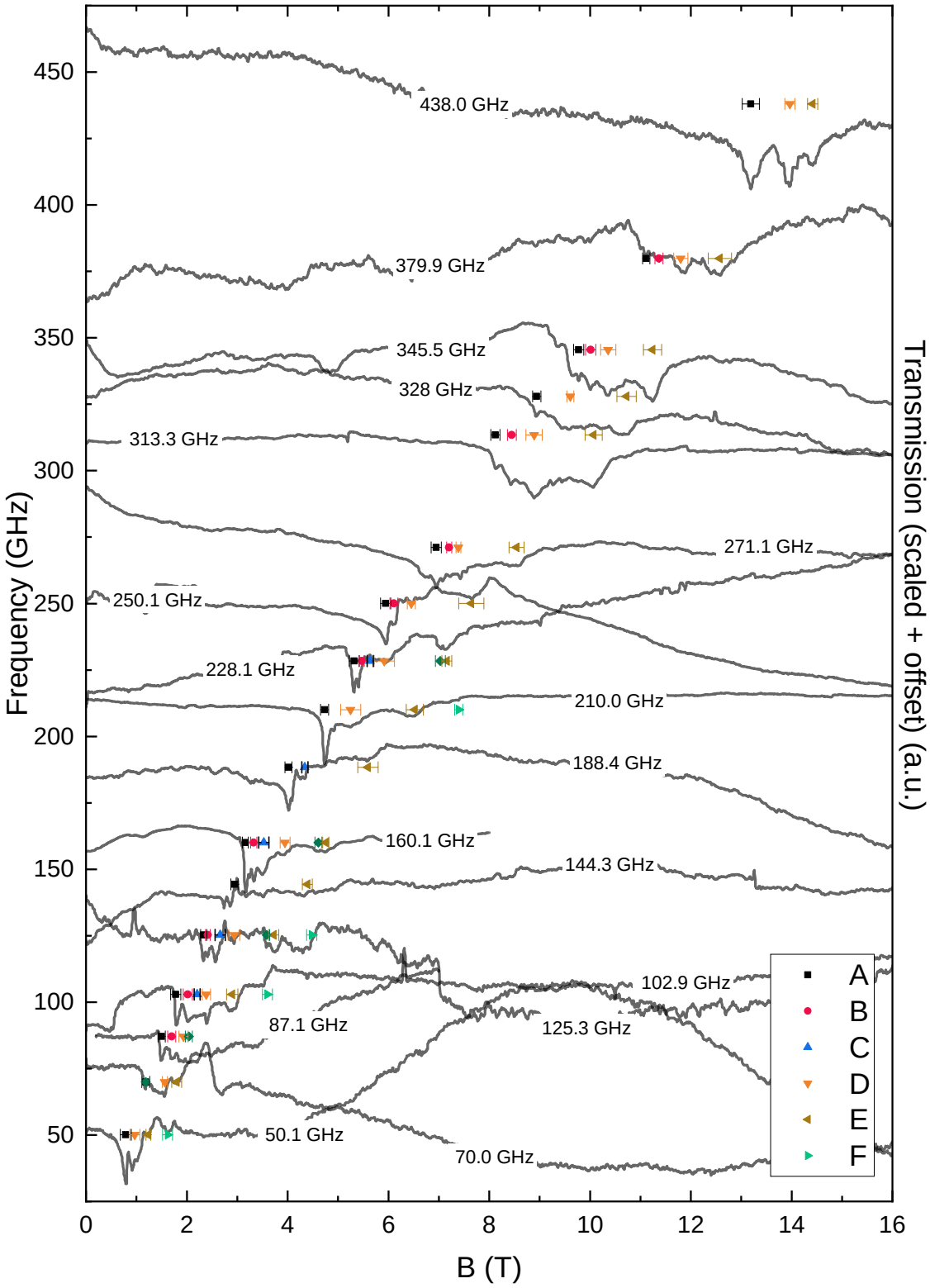


Figure 4.26: Phase corrected HF-ESR transmission spectra (down-sweep) at $T = 2\,\mathrm{K}$. The spectra are shifted and scaled for better clarity of the plot. The observed resonances are marked by the black squares and positioned according to the ordinate on the left. The measurement was carried out on a loose powder sample of CuΔ.

All observed resonance features are summarized in a ν-B diagram (figure 4.27). Branches A,B and D exhibit bending in the vicinity of $B \approx 5\,\mathrm{T}$. They change their slopes from $g_{\mathrm{eff}} > 2.6$ to slopes corresponding to $g_{\mathrm{eff}} < 1.92$. To quantify this change a linear orthogonal-distance-regression for $B < 4\,\mathrm{T}$ and $B > 6\,\mathrm{T}$ is performed separately. This fitting is conducted using Scipy's ODR package [54]. The resulting effective g-factors and ZFS Δ can be found in table 4.6 and the fitted functions are plotted in figure 4.27 alongside the positions of the resonance fields as either dashed or solid lines. It has to be noted that for branch B there are only two data points for lower fields leading to the omission of any uncertainties and $\chi^2_{\mathrm{reduced}} = 0$. Resonance branches A and D start out with different slopes but become parallel for higher fields. $\chi^2_{\mathrm{reduced}}$ is small ($\chi^2_{\mathrm{reduced}} << 1$) for all fits except branch A for low fields. On one hand this indicates some overestimation of errors and for A that there are some significant non-linearities remaining even in such a limit field range up to $B = 4\,\mathrm{T}$. In contrast to this branches E and F are linear as deemed from the linear fits over the entire field range, yielding effective g-factors and ZFS Δ, that are shown in table 4.7 and plotted in figure 4.26. With $\chi^2_{\mathrm{reduced}} < 1$ (especially for F) one is in the regime of over fitting or overestimating uncertainties. Which is quite reasonable for F, where the ZFS parameter Δ vanishes within errors.

Examination of the temperature sweeps at $\nu = 102.1\,\mathrm{GHz}$ (figure 4.28) and $\nu = 228.1\,\mathrm{GHz}$ (figure 4.29) reveals that all resonance features observed in the $T = 2\,\mathrm{K}$ data arise from transition originating from the system's ground state. This conclusion is reached, due to their intensity decreasing steadily with temperature, which can be easily observed in figure 4.30(a) for $\nu = 102.1\,\mathrm{GHz}$ and in figure 4.30(b) for $\nu = 228.1\,\mathrm{GHz}$. Here the same method as in section 4.1.3 was used to calculate the relative intensities of the observed resonance features. The chosen field ranges are shown in table A.2. In figure 4.30(b) the estimated intensities of features A to E at $\nu = 228.4\,\mathrm{GHz}$ are shown. Comparing the resonance features and their resonance fields for the loose powder measurements to the fixed powder ones shows, that the loose powder resonances correspond to the set of features decreasing in intensity more quickly than, for example, the cluster at $B \approx 8.2\,\mathrm{T}$ for $\nu = 228.4\,\mathrm{GHz}$. Which indicates, that said cluster originates from paramagnetic impurities in the grease used to fix the sample or some other contamination, which could have occurred during preparation of the fixed powder sample. However for $\nu = 228.1\,\mathrm{GHz}$ there are some additional resonance features $\mathrm{h}_{1\ldots4}$ visible, which have their maximal intensities in the range of $8\mathrm{K} \leq T \leq 14\,\mathrm{K}$ (see figure 4.30(c)). Something similar to this was not observed for the temperature sweep at $\nu = 102.1\,\mathrm{GHz}$. The origin of $\mathrm{h}_{1\ldots4}$ is unclear, but they appear to correspond to transitions between exited states.

All of these observations lead to the following picture: The ground state quartet is split by the anisotropic exchange interactions into two doublets at $B = 0\,\mathrm{T}$ with a well isolated $S_{i\in\{\mathrm{x,y,z}\}} \approx 3/2$ ground state. Branch E arises from excitations within the lowest of these two doublets. The remaining two states from the split ground state quartet initially have a differing slope but they start to interact with the states from the two remaining $S \approx 1/2$ doublets around $B = 5\,\mathrm{T}$. This mixing then leads an avoided level crossing and a decrease and aliment of their slopes. Features B and C are possibly artifacts from misalignment of the sample to the magnetic field or the two orientations of molecules in the unit cell. With $g_{\mathrm{eff}} \approx 2$ branch F could be the result of paramagnetic impurities within the sample, as already conjectured from the fixed powder data.

Branch	A	B	D
Fit range	$B < 4\,\mathrm{T}$	$B < 4\,\mathrm{T}$	$B < 4\,\mathrm{T}$
g_{eff}	3.16(13)	3.20	2.65(6)
Δ (GHZ)	19(4)	10.4	13.6(2.2)
$\chi^2_{\mathrm{reduced}}$	1.51	0.0	0.48
Fit range	$B > 6\,\mathrm{T}$	$B > 5\,\mathrm{T}$	$B > 6\,\mathrm{T}$
g_{eff}	1.84(3)	1.98(7)	1.836(12)
Δ (GHZ)	99(5)	77(6)	81.3(1.5)
$\chi^2_{\mathrm{reduced}}$	0.35	0.62	0.07

Table 4.6: Effective g-factors and ZFS for the resonance branches A, B and D at $T = 2\,\mathrm{K}$ of CuΔ as obtained through fitting of the function $\nu(B) = \Delta + 13.98\,\frac{\mathrm{GHz}}{\mathrm{T}} \cdot g \cdot B$. Additionally the reduced χ^2 value of the fit is given in order to asses it's merit. The range of the used data points is indicated in the table.

Branch	E	F
g	2.010(14)	2.02(4)
Δ (GHZ)	16.5(1.5)	1.5(2.5)
$\chi^2_{\mathrm{reduced}}$	0.73	0.43

Table 4.7: Effective g-factors and ZFS for the resonance branches E and F of CuΔ at $T = 2\,\mathrm{K}$ as obtained through fitting of the function $\nu(B) = \Delta + 13.98\,\frac{\mathrm{GHz}}{\mathrm{T}} \cdot g \cdot B$. Additionally the reduced χ^2 value of the fit is given in order to asses it's merit. The range of the used data points is indicated in the table.

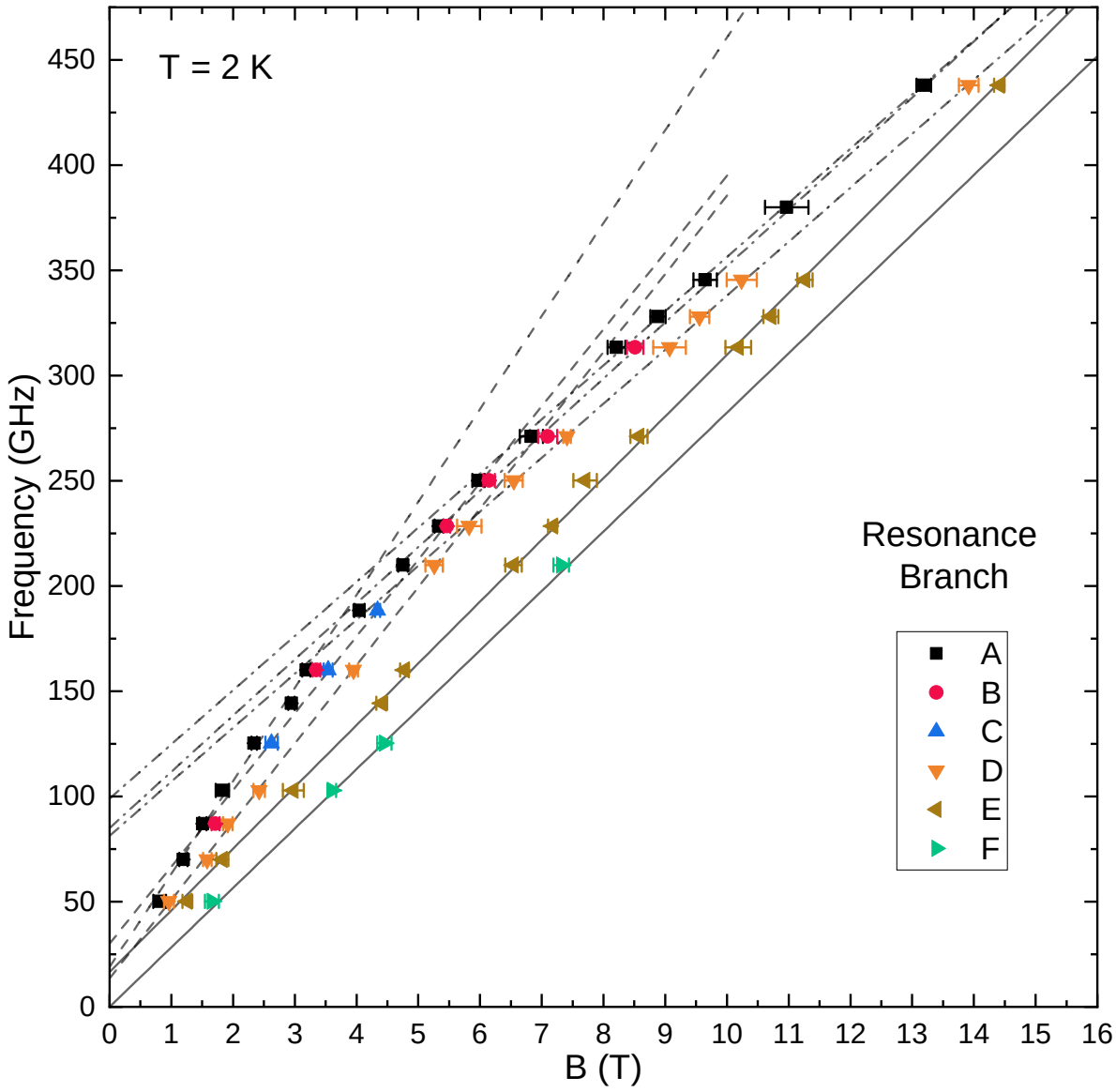


Figure 4.27: Resonance field positions for spectra at different frequencies for CuΔ. The displayed positions are averaged over their respective positions in the up and down sweeps. Linear fits are included, as discussed in the text. These are either depicted as solid lines in which case the fit range is the entire field range or dashed (dashed-dotted). There the fit is performed with the data for low (high) fields only.

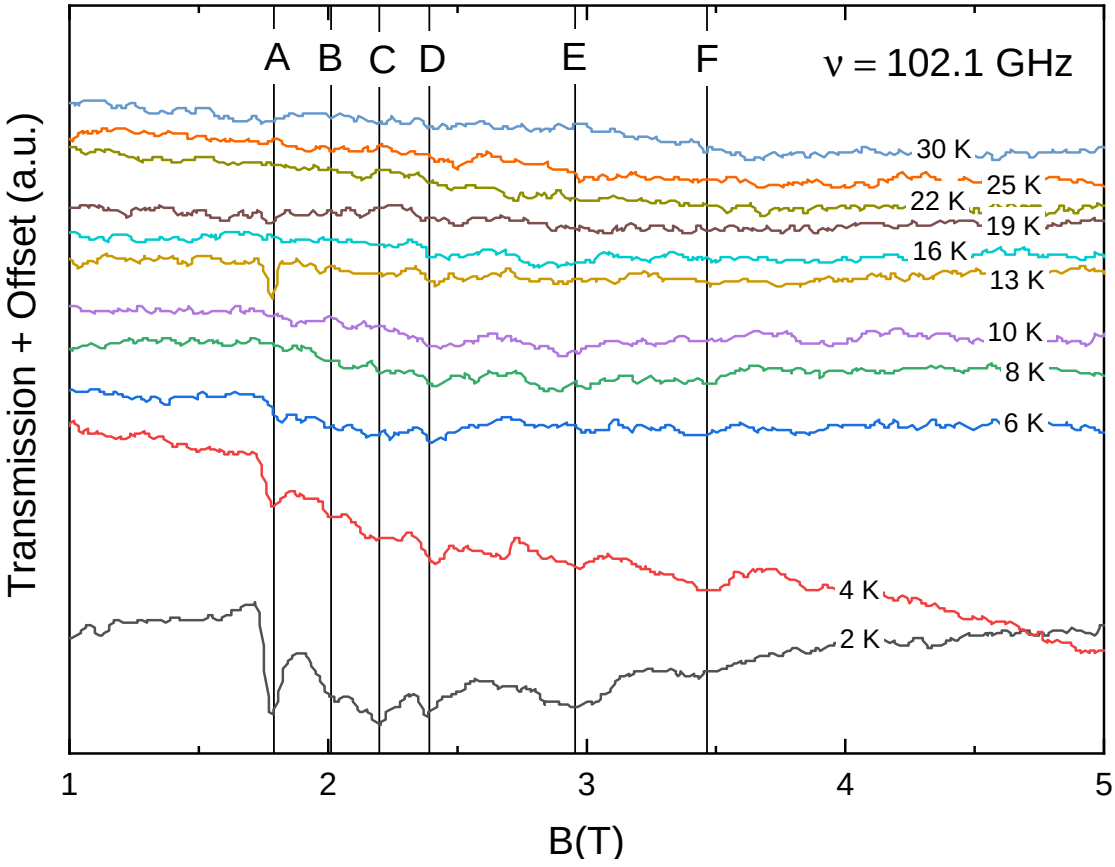


Figure 4.28: HF-ESR spectra (down-sweeps) recorded at a microwave frequency of $\nu = 102.1\,\mathrm{GHz}$ at different temperatures. The spectra are not phase corrected. The position of observed resonances are marked by vertical lines. The measurements were performed on a loose powder sample of CuΔ.

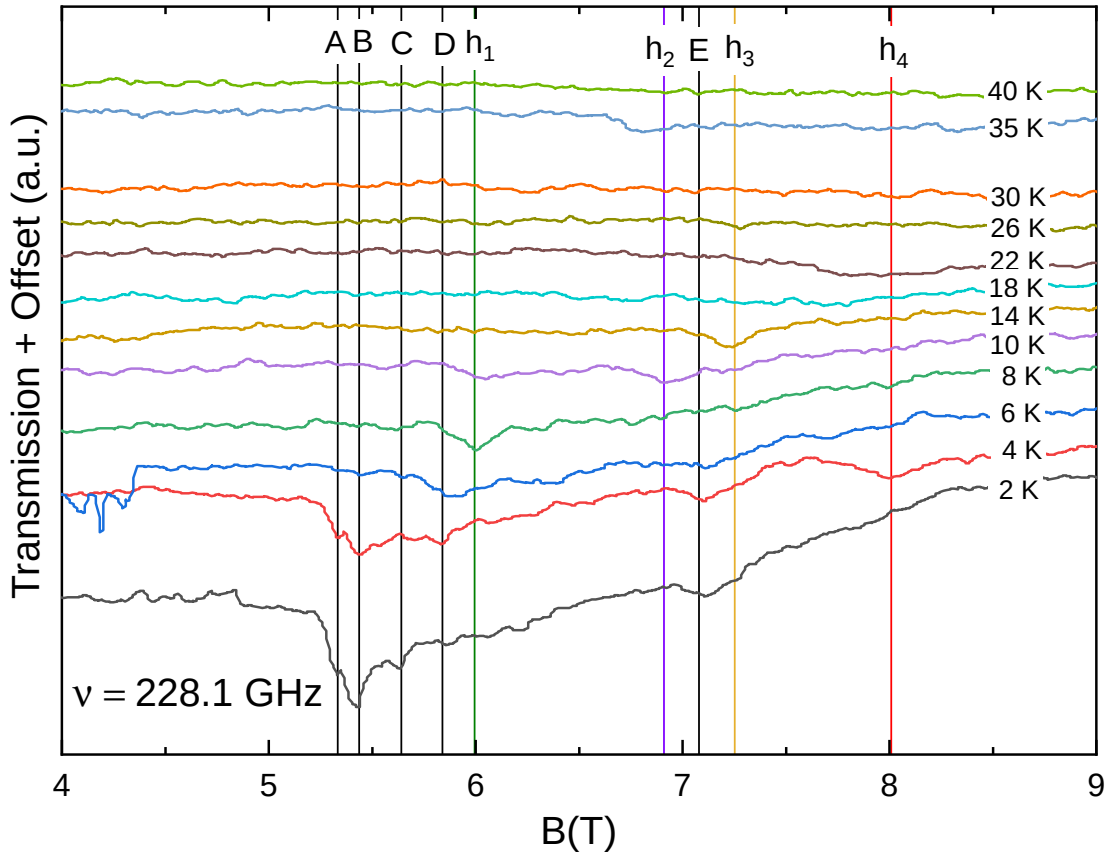


Figure 4.29: HF-ESR spectra (down-sweeps) recorded at a microwave frequency of $\nu = 228.1\,\mathrm{GHz}$ at different temperatures. The spectra are not phase corrected. The position of observed resonances are marked by vertical lines. The color of these lines indicate at which temperature the feature has it's maximal intensity. The measurements were performed on a loose powder sample of CuΔ.

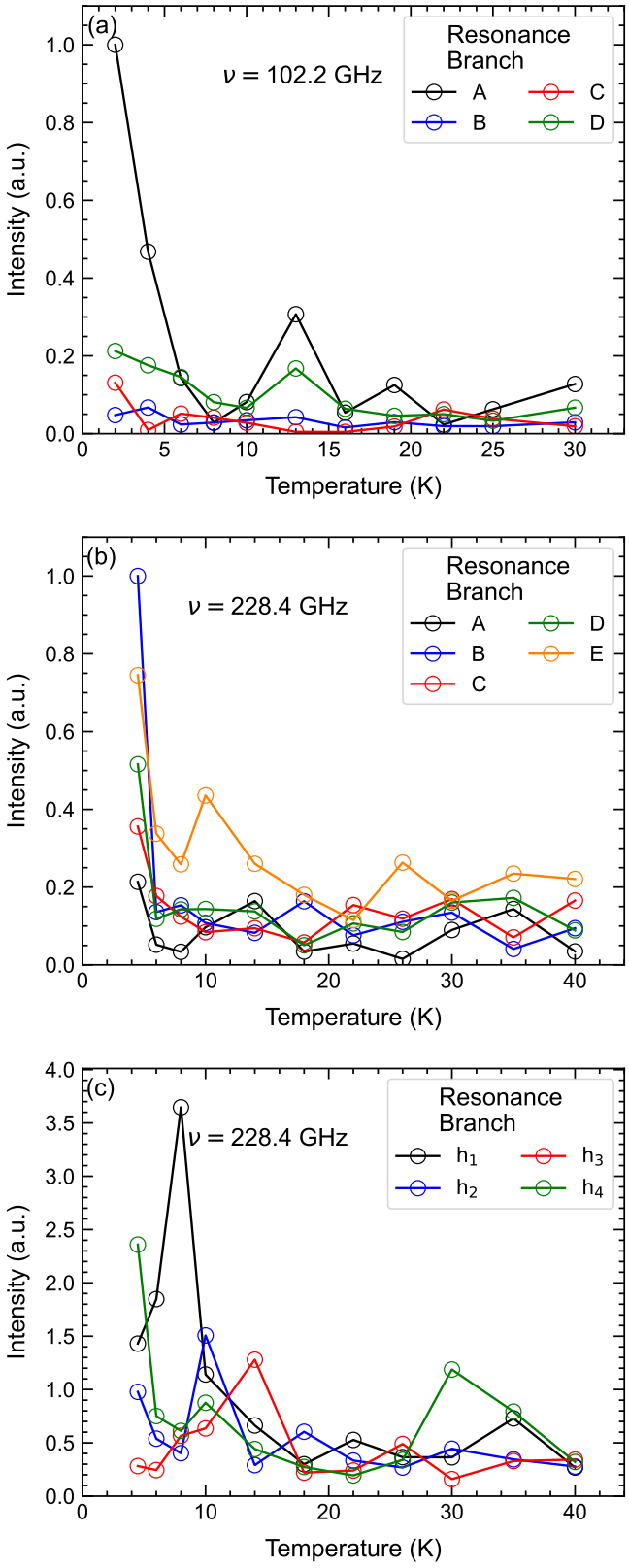


Figure 4.30: Intensities of the resonance features observed at a microwave frequency of (a) $\nu = 102.9\,\mathrm{GHz}$ and (b),(c) $\nu = 228.4\,\mathrm{GHz}$. The corresponding spectra are displayed in figures 4.28 and 4.29. In (b) the intensities for features A to E are displayed and in (c) the intensities of h_1 to h_2. The intensities were determined by subtracting a linear background from each peak and then integrating over them. The absolute value of these integrals is shown here. The measurement was performed on a sample of fixed CoΔ powder.

Chapter 5

Ab-Initio Calculations on $NMe_4[Cu_3(\mu_3\text{-}F)(TFA)_6(Py)_3]$

All relevant physical properties of the molecules investigated in the previous section or (in general) most condensed matter systems can be fully described by the usual classical Hamiltonian with some relativistic corrections added. The issue being faced is how to take this Hamiltonian and actually calculate the physical properties from it. Here approximations are generally needed due to the required size of the system's Hilbert space: If there are N_e electrons in a system and one considers N_o spin-orbitals or one-particle basis functions the dimension of the Hilbert space $\mathcal{H}$ scales as

$$|\mathcal{H}| = \binom{N_o}{N_e}. \tag{5.1}$$

Which increases exponentially with the number of electrons/orbitals. To illustrate this consider the simple molecule acetylene (C_2H_2): There are total of 14 electrons and if one takes a basis of 1s-,2s- and 2p-orbitals for the hydrogen and 1s-,2s-,3s-,2p- and 3p-orbitals for the carbon this already yields a many body Hilbert space of dimension $|\mathcal{H}| = 3245372870670 \approx 3.2 \cdot 10^{12}$. Considering that the molecule $[Cu_3(\mu_3\text{-}F)(TFA)_6(Py)_3]^-$ has a total 553 electrons, it becomes clear that a straight forward diagonalization of the full Hamiltonian is not traceable. However treating this many electrons on a mean-field level (like DFT) is quite doable at limited computational cost. But this comes with the drawback, that a lot of interesting physics attributed to correlations is lost by treating the system on a mean-field level. This leads to the idea behind the methods employed in this thesis: Orbitals which can be treated reasonably well on a mean-field level (like filled s and p shells) are treated on the level of DFT. Orbitals for which DFT is notoriously insufficient (like open d or f shells) should be treated on a full many body level. The scheme presented in this thesis will follow the steps outlined here:

1. A DFT calculation is performed to obtain a mean-field tight-binding Hamiltonian of the molecule and the atomic eigenstates of relevant atoms (like the transition metals).

2. This tight binding Hamiltonian is rotated to a basis which includes all those orbitals, which should be treated fully correlated. These are for example the d-shells of the transition metal ions. The Hamiltonian is block-band diagonalized with the correlated orbitals forming the first block. The other blocks form the corresponding n-th order Ligand orbitals. This perturbative expansion can be truncated to reduce computational costs to an acceptable level.

3. Correlations are added on the respective orbitals and the Hamiltonian is diagonalized.

4. A low energy effective Hamiltonian can then be constructed and physical observables calculated.

5.1 Density-Functional Theory Calculations

The DFT calculations discussed in this section were all performed using the *ORCA* software package (version: 5.0.3) [60]. *ORCA* was chosen due to it's wide adoption, usage of localized atom-centered basis functions and the possibility to access important quantities (like the overlap matrix) of the calculation.

Due to the large inter-molecular distances in CuΔ were inter-molecular interactions neglected. Also the solvent cation and copper complex anion were assumed to be fully ionic so that only the tri-nuclear complex was considered for the DFT calculations.

5.1.1 Choice of Functional and Basis Set

ORCA offers many choices of functionals. Calculations were conducted using HF[1], PWLDA[2], BP86[3], TPSS[4] and TPSSh[5]. The calculations were performed using the restricted-open-shell-kohn-sham (ROKS) option for DFT and the restricted-open-shell-Hartree-Fock (ROHF) option (first introduced in [65]) for HF. Using ROKS/ROHF yields molecular orbitals that spatially are the same for spin up and down. These orbitals are doubly filled as far as possible with the remaining shells being either singly occupied or unoccupied. That way open shells can be treated while still keeping the physical interpretation of the molecular orbitals (when compared to UHF/UKS and RHF/RKS, see the *ORCA* manual [66]). Since the magnetization data shows ferromagnetic coupling, ferromagnetic coupling is enforced in the DFT calculation by setting the spin multiplicity to four.

To compare the results between different functionals, the energies of the molecular orbitals are plotted in figure 5.1. The first thing to note is, that for all functionals tested, as well as, for HF the three singularly occupied molecular orbitals have a lower energy then some of the doubly occupied orbitals. This is somewhat counter intuitive for a mean-field solution, but in principle possible since the total energy of the system is minimized. This means, that a change in occupation changes the electron density and thereby the total electronic energy, leading to the possibility of converging to such a configuration. Some properties of the calculated electronic structure, such as the HOMO[6]-LUMO[7] gap ($E_g = E_{\mathrm{LUMO}} - E_{\mathrm{HOMO}}$), are shown in table 5.1. The HOMO-LUMO gap is drastically larger for HF than for DFT and E_g increases from PWLDA to BP86 to TPSS to TPSSh. This is generally to be expected due to the HF exchange present in hybrid functionals stabilizing the HOMO [67] by canceling some of the self-interaction error. Considering the Mulliken population analysis of the copper ions, one can observe that the ionicity of the bonds follow the general trend shown by the HOMO-LUMO gap, i.e. increasing from the LDA to the hybrid functional and HF. This is again not unexpected, due to the HF-exchange preferring localized electrons, while LDA functionals prefer a more uniform electron density, leading to an overestimation of the bonds' covalency.

Unfortunately hybrid (and double hybrid) functionals with a higher percentage of HF exchange could not be examined due to the SCF[8]-loop not converging for these functionals.

[1] Hartree-Fock
[2] Perdew-Wang parameterization of LDA [61]
[3] Becke 1988 GGA functional [62]
[4] Tao-Perdew-Staroverov-Scuseria meta-GGA functional [63]
[5] Hybrid version of TPSS [63, 64]
[6] Highest occupied molecular orbital
[7] Lowest unoccupied molecular orbital
[8] Self consistent field

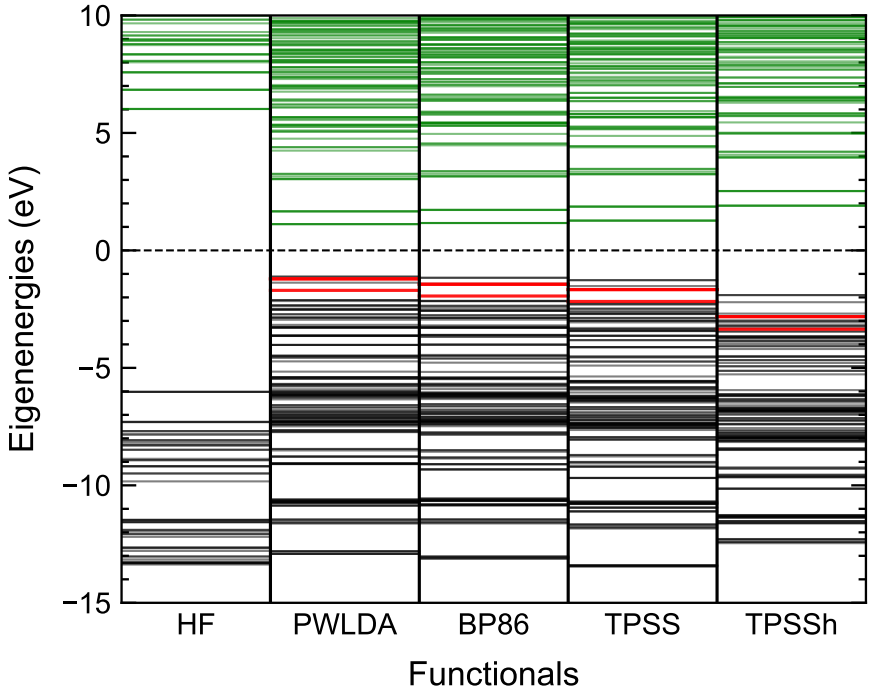


Figure 5.1: Eigenenergies calculated using different functionals and the *def2-TZVP* basis set for $[Cu_3(\mu_3\text{-}F)(TFA)_6(Py)_3]^-$. Doubly occupied molecular orbitals are displayed in black, singly occupied orbitals in red and unoccupied orbitals in green. The Fermi-energy is marked by the dashed line. The energies are shifted so that the fermi energy equals zero: $E_{\text{fermi}} := E_{\text{HOMO}} + E_g/2 = 0$. The calculations were performed using *ORCA* [60]. For more details refer to the text.

	HF	PWLDA	BP86	TPSS	TPSSh
Mulliken gross atomic population of the copper ions	28.05	28.85	28.77	28.72	28.64
HOMO-LUMO gap (eV)	12.0342	2.2334	2.3273	2.5315	3.8017

Table 5.1: Dependence of the HOMO-LUMO gap and the electronic population of the copper ions on the choice of functional. The *def2-TZVP* basis set was used and the single point SCF calculations performed using *ORCA* [60].

To ascertain the impact of the choice of basis set on the DFT results, single point calculations with the PWLDA functional for the basis sets *def2-SVP*[9], *def2-TZVP*[10], *def2-QZVP*[11] and *ANO-pVTZ*[12] were performed. The resulting energy level diagram is shown in figure 5.2. Going from *def2-SVP* to the triple zeta valance variant changes the spectrum most noticeably around −3eV where the states are more separated when compared to *def2-TZVP*, *def2-QZVP* and *ANO-pVTZ*. Going to the quadruple zeta variant, which is the largest basis set tested here (see table 5.2), yields only small changes: The HOMO-LUMO gap differs only by 0.01 eV. Also the remaining DOS is almost identical to *def2-TZVP*. This indicates that finite basis size effects are already quite limited at the triple zeta level considering that *def2-QZVP* has almost twice as many basis states as *def2-TZVP* for this system. Comparing the *def2-nZVP* (n$\in \{T, Q\}$) basis sets to the antomic natural orbitals set *ANO-pVTZ* again yields only small differences of the order of 0.01 eV. The results of the atomic natural orbital basis set is expected to

[9]Split valence basis sets by Ahlrichs et al. [68]
[10]Triple zeta valence basis sets by Ahlrichs et al. [68]
[11]Quadruple zeta valence basis sets by Ahlrichs et al. [68]
[12]Atomic natural orbitals basis set with triple zeta valence as implemented in *ORCA* [69]

superior the equivalent *def2-nZVP* (n$\in \{T, Q\}$) set, although they should become more relevant for heavy elements [69]. Considering all of this, the def2-TZVP basis set was chosen for further calculations, due to it's acceptable performance and small computational cost when compared to the larger *def2-QZVP* set and the ANO[13] set (see table 5.2).

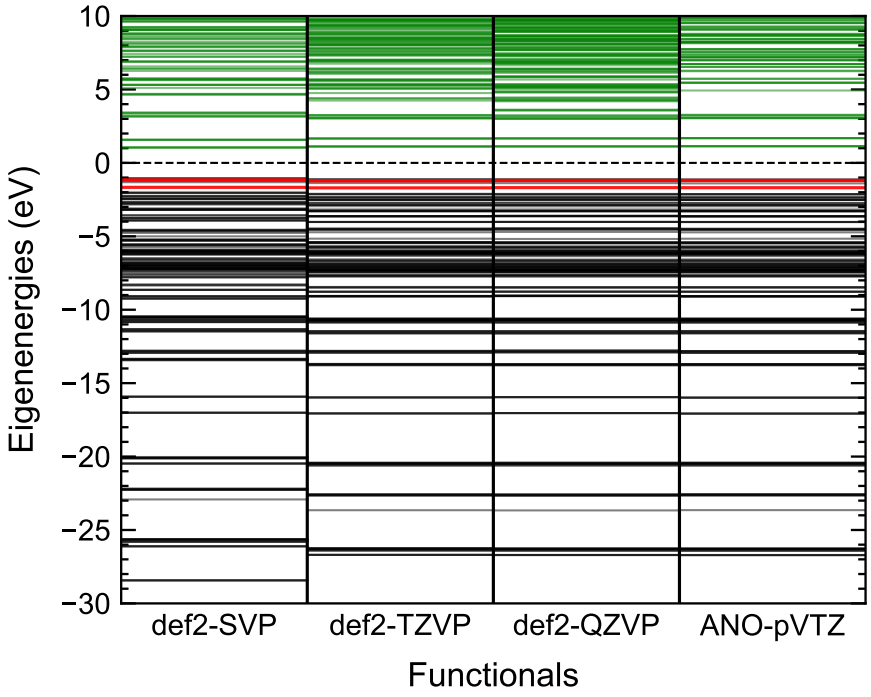


Figure 5.2: Eigenenergies calculated using different basis sets for $[Cu_3(\mu_3\text{-}F)(TFA)_6(Py)_3]^-$ with the PWLDA functional. Doubly occupied molecular orbitals are displayed in black, singly occupied orbitals in red and unoccupied orbitals in green. The Fermi-energy is marked by the dashed line. The energies are shifted so that the fermi energy equals zero: $E_{\text{fermi}} := E_{\text{HOMO}} + E_g/2 = 0$. The calculations were performed using *ORCA* [60]. For more details refer to the text.

	def2-SVP	*def2-TZVP*	*def2-OZVP*	*ANO-pVTZ*
Number of basis functions	1022	2116	4179	2217
Time to converge self consistency loop (s)	3623	6168	61010	99605
HOMO-LUMO gap (eV)	2.0921	2.2334	2.2423	2.2671

Table 5.2: Basis set dependence of the HOMO-LUMO gap and the runtime of the single point calculation with the PWLDA functional. The calculations were performed in a single thread of an *Intel®Core™ i5-7600* using *ORCA* [60].

5.1.2 Broken-Symmetry DFT

Broken-symmetry DFT (BS-DFT) can be used to estimate a systems magnetic properties [70]. The idea being to calculate the single point energies of different electronic configurations and calculate properties like the exchange coupling from there [70]. But first of all it has to be noted, that due to DFT being a mean-field method $\hat{S}^2$ is no longer a good quantum number. This leads to the approximation/association

[13] Atomic natural orbital

Functional	Type	$J_{\text{BS-DFT}}$ (K)	Coupling
PWLDA	LDA	972	AF
BP86	GGA	717	AF
TPSS	meta-GGA	573	AF
TPSSh	hybrid meta-GGA	275	AF

Table 5.3: Estimated spin-spin coupling based on the spin Hamiltonian $H_{\text{HDvV}} = JS_iS_j$ using broken-symmetry DFT with the given functionals and the *def2-TZVP* basis set.

of $\hat{S}_z$ with the total spin quantum number. One of the two states investigated here in BS-DFT is the $S_z = 3/2$ state, where there are three unpaired electrons in spin up orbitals. The second state is the broken-symmetry state where the spatial and $SU(2)$ symmetries are explicitly broken by flipping the spin of one unpaired electron. This yields an $S_z = 1/2$ state. The exchange coupling is then calculated as [60]

$$J_{\text{BS-DFT}} = 2\frac{E_{\text{HS}} - E_{\text{LS}}}{\langle S^2\rangle_{\text{HS}} - \langle S^2\rangle_{\text{LS}}}\,. \tag{5.2}$$

The exchange coupling J shown here is defined with respect to the spin Hamiltonian $H_{\text{HDvV;i,j}} = J_{i,j}S_iS_j$. The subscript HS (LS) refers to the high-(low-) spin states which were obtained by BS-DFT. The couplings calculated this way are shown in table 5.3 for different functionals. The couplings predicted by BS-DFT are strongly antiferromagnetic with the strength depending drastically on the choice of functional. TPSSh yields the smallest AF coupling while PWLDA yields the largest value. These results contradict the experimental results, where FM coupling was observed. This clearly shows, that DFT alone is insufficient to describe the magnetic properties of this particular transition metal complex.

5.1.3 DFT of Isolated Copper and Fluorine Atoms

For the implementation of the coulomb exchange, as well as, the basis transformations discussed in section 5.2 it is necessary to determine the atomic orbitals of copper and fluorine. This further enables the projection of the DOS[14] to those orbitals, yielding the respective pDOS[15]. Therefore a DFT calculation is performed for these two atoms and the energy level diagrams are plotted in figure 5.3(a) for copper and figure 5.3(b) for fluorine. The states shown for copper are from lowest to highest energy: 3d, 4s, 4p, 5s and 4d. The HOMO-LUMO gap follows the same behavior as for the complete molecule with respect to the choice of functional, i.e increasing E_{g} from LDA to Meta-Hybrid to HF. For fluorine the lowest state shown is 2s. Due to the p^5 configuration of atomic fluorine is the 2p shell split between doubly and singly occupied states. This splitting originates from the fact that the electron density is higher in doubly occupied orbitals than for singly occupied ones. This leads to an increased coulomb repulsion experienced by the electrons and therefore an increased onsite energy. This property of DFT calculations is called self-interaction, due to the electron interaction with it's own density. This is however irrelevant in this case, since only the shape of the molecular orbitals is needed, not their energy. The ROHF algorithm of *ORCA* supports partial occupations so that the 2p orbitals are filled by 5/3 electrons. This prevents the splitting seen for DFT.

[14] Density of states
[15] Projected density of states

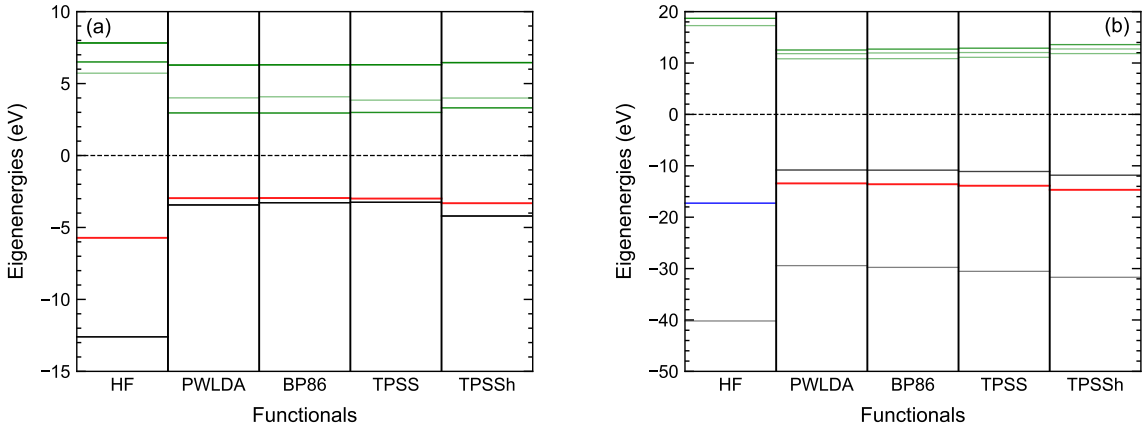


Figure 5.3: Energy level diagram for (a) copper and (b) fluorine as calculated in *ORCA* [60] for different functionals. The *def2-TZVP* basis set was used. Doubly occupied molecular orbitals are displayed in black, singly occupied orbitals in red and unoccupied orbitals in green. Orbitals with a partial occupation of 5/3 are marked by blue. The Fermi-energy is marked by the dashed line. The energies are shifted so that the fermi energy equals zero: $E_{\text{fermi}} := E_{\text{HOMO}} + E_g/2 = 0$.

5.1.4 Partial Density of States and Molecular Orbitals

The atomic orbitals of fluorine and copper allow for the projection of the DOS[16] to those orbitals, yielding their respective pDOS. The pDOS of the μ_3-F2s and 2p orbitals and the Cu 3d orbitals are plotted in figures 5.4(a) and 5.4(b) with a linear and a logarithmic scale respectively. The pDOS shown was calculated using the TSPPh functional with the *def2-TZVP* basis set. The fluorine's 2s pDOS is mostly localized at an energy of $\omega = -26.6\,\text{eV}$ with some contributions at $\omega \approx -9\,\text{eV}$ and $\omega \approx -5\,\text{eV}$. These two energies roughly correspond to the energies at which the fluorine's 2p and coppers' 3d shells have their highest pDOS. In the energy range $-10\,\text{eV} \lesssim \omega \lesssim -3\,\text{eV}$ there is a significant overlap between the pDOS of the fluorine's 2p and coppers' 3d shells, suggesting that those orbitals hybridize in this energy range. As stated before, there is also some hybridization of the 2s and 3d shells with the fluorine's 2s orbitals. Except for the splitting of the coppers' 3d shells' pDOS at $\omega \approx -7.4\,\text{eV}$ there are no large gaps between the 3d orbitals for $\omega \gtrsim -10\,\text{eV}$. This lack of clear separation of the orbitals is consistent with the low local spatial symmetry around the copper ions, resulting in a total lifting of their SO(3) induced degeneracy. At energies larger than the LUMO energy there is a small tail with contributions of all the shells discussed previously, however almost the entire copper 3d pDOS is located at energies in the range of $-35\,\text{eV} < \omega < -1\,\text{eV}$.

The LUMO, highest energy singly- and doubly-occupied MOs[17] and their eigenenergies are shown in figure 5.5. The plot shows the isosurface containing 80% of the orbitals density. The three LUMOs (fist row) are mainly located on the pyridine-groups, with little hybridization with the Cu 3d orbitals as discussed previously. The three doubly occupied HOMOs (second row) and the three singly occupied HOMOs (third row) consist mainly of the coppers' 3d orbitals hybridized with the 2p orbitals of the surrounding oxygen atoms. Some admixture of the μ_3-F2p and shells from the nitrogen atoms is present as well. The orientation of the contributing Cu 3d orbitals flips by approximately 90° between the differently occupied HOMOs. For both occupations these 3d orbitals are oriented along one of the two O-Cu-O bonds on each side of the triangle and the μ_3-F-Cu-N bonds. Another difference between the singly and doubly occupied orbitals shown here is their spatial extent, with the singly occupied MOs significantly

[16] Density of states
[17] Molecular orbitals

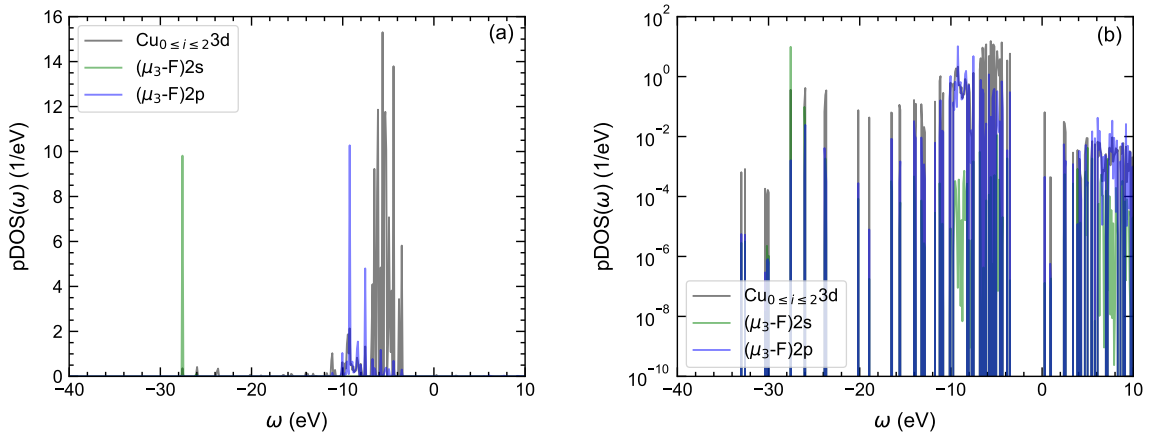


Figure 5.4: Projected-DOS-plot of the coppers' 3d and μ_3-F's 2s and 2p shells calculated with DFT (TPSSh functional, *def2-TZVP* basis set) for CuΔ . The pDOS for the coppers' 3d orbitals shown in gray, for the fluorine's 2s shell in green and for the fluorine's 2p shell in blue. The scale of the ordinate is chosen to be (a) linear and (b) logarithmic.

more localized than the doubly occupied orbitals.

The plots nicely show one problem of the *ORCA* DFT calculations, namely that the molecules symmetry is not enforced and that states, that should be degenerate due to symmetry, differ slightly in energy. Examples of these are the shown LUMOs and the two energetically higher lying singly and doubly occupied HOMOs respectively (see figure 5.5). These states have an energy difference on the order of $\delta \approx 1\,\mathrm{meV}$.

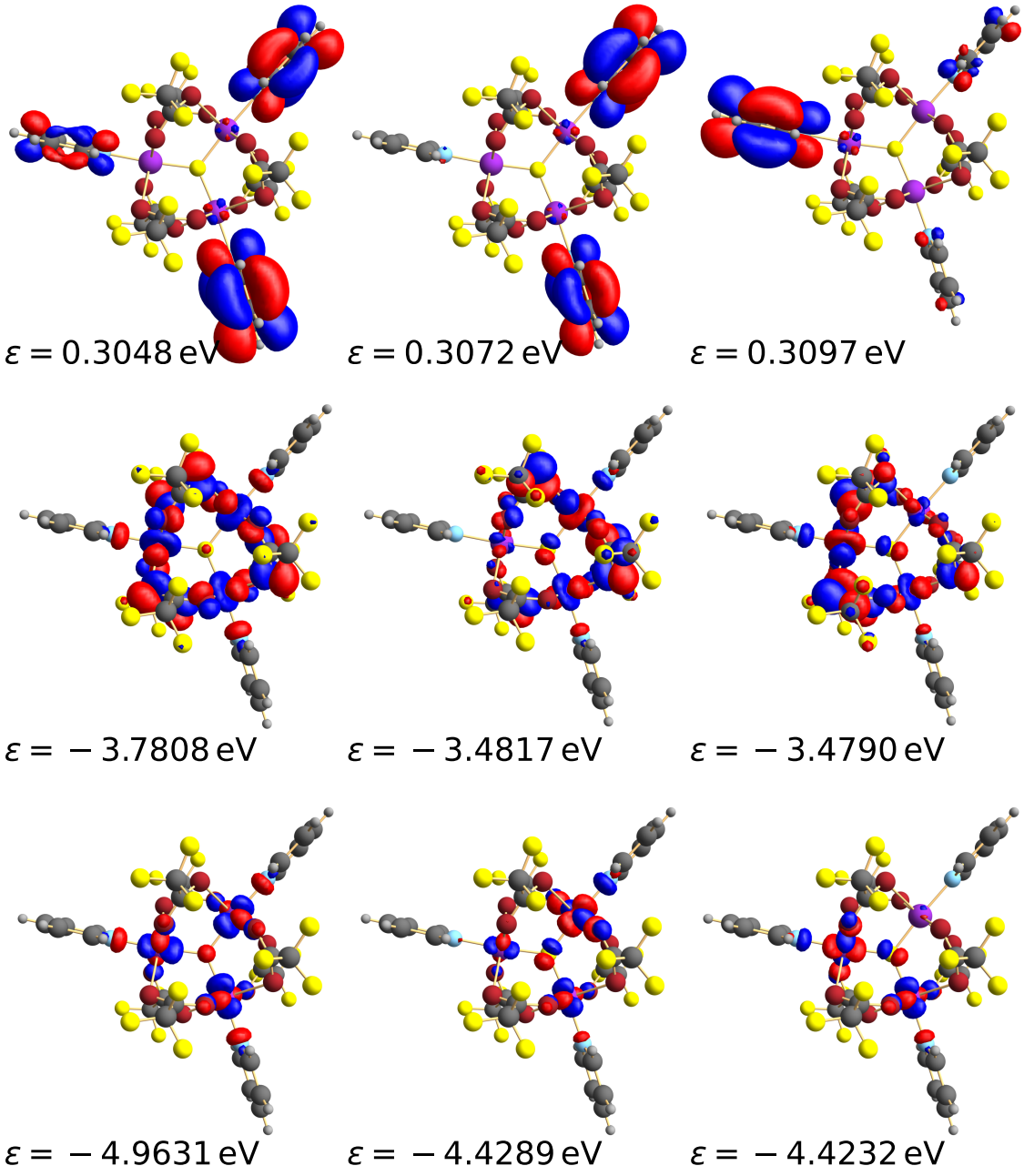


Figure 5.5: Isosurface-plot of the molecular orbitals constructed with DFT (TPSSh functional, *def2-TZVP* basis set) for CuΔ. The isosurface contains 80% of the orbitals density. The eigenenergies ϵ of the MOs is written below each subplot. The first row depicts the three LUMOs, the second row depicts the three doubly occupied HOMOs and the third row shows the three singly occupied HOMOs. The color of the MOs indicated their phase at that point in space.

5.2 From a Mean-Field Hamiltonian to a Ligand-Field Theory Model

5.2.1 Reduction of Hilberspace size

For usage as a basis for a full many body calculation the Hamiltonian $\mathcal{H}_{\mathrm{DFT}}$, obtained by DFT with the *def2-TZVP* basis set, is too large as $|\mathcal{H}_{\mathrm{DFT}}| = 2 \cdot 2116 = 4232$ spin orbitals (see table 5.2). These are too many basis states, since this would yield a many-body Hilbert space $\mathcal{H}^{\mathrm{MB}}$ of dimension

$$|\mathcal{H}^{\mathrm{MB}}| = \binom{|\mathcal{H}_{\mathrm{DFT}}|}{N_{\mathrm{e}}} = \binom{2 \cdot 2116}{553} > 5 \cdot 10^{710}\,, \tag{5.3}$$

where N_{e} denotes the number of electrons in the system. In order to be able to proceed, requires the Hilbert space a reduction of the number of basis states.

The first step is to cut the number of basis states in the MO basis obtained by DFT. This is done by discarding all MOs, whose eigenenergy ϵ lies outside of a given energy window $\epsilon_{\mathrm{l}} \leq \epsilon \leq \epsilon_{\mathrm{u}}$. To determine the bounds of this interval, the pDOS discussed in section 5.1.4 and shown in figure 5.4(b) is considered. $\epsilon\mathrm{u} = -1\,\mathrm{eV}$ is chosen, such that it resides within the HOMO-LUMO gap. This avoids contamination by unoccupied MOs of the ligand orbitals, which are constructed later. The lower bound is chosen, such that most of the coppers' 3d and μ_3-F2s and 2p shells are contained within this energy window. Core excitations at $\omega \approx -75\,\mathrm{eV}$ are excluded by setting $\epsilon_{\mathrm{u}} = -33\,\mathrm{eV}$. After this initial step 380 spin orbitals (190 single particle orbitals) remain out of the initial 4232. The number of electrons in this energy range corresponds to three holes, yielding a many body Hilbert space of size

$$|\mathcal{H}_1^{\mathrm{MB}}| = \binom{380}{377} \approx 9 \cdot 10^6\,, \tag{5.4}$$

which is much more traceable than before, but it it still possible to reasonably reduce this number further.

The next step is to rotate the new basis into one where unimportant basis functions can be easily discarded. The first part of this basis transformation is to rotate the basis, such that the shells for which correlations are important

$$\mathcal{B}_{\mathrm{corr}} = \mathcal{B}_{\mathrm{3d}} \cup \mathcal{B}_{\mathrm{2s}} \cup \mathcal{B}_{\mathrm{2p}}\,, \tag{5.5}$$

form the first block of basis states. In the case of $[Cu_3(\mu_3\text{-F})(TFA)_6(Py)_3]^-$ these orbitals are the coppers' 3d ($\mathcal{B}_{\mathrm{3d}}$), the μ_3-F's 2s ($\mathcal{B}_{\mathrm{2s}}$) and 2p ($\mathcal{B}_{\mathrm{2p}}$) shells. Due to these basis states not being othonormal, this first set of states is orthonormalized using Löwdin symmetric orthonormalisation [71, 72]. This method of orthogonalization is chosen, because it changes the original orbitals minimally [71] and does so symmetrically. The latter point meaning, that all orbitals are changed equally, which is in contrast to Gram-Schmidt orthogonalization [73], where the functions are progressively altered more the later they are processed. The symmetric orthonormalization is implemented as

$$S := W \times W^\dagger = D \times \mathrm{diag}(\{\sqrt{\lambda_i}\}_{0 \leq i < |S|}) \times D^\dagger\,, \tag{5.6}$$

$$S^{-\frac{1}{2}} = D \times \mathrm{diag}(\{\frac{1}{\sqrt{\lambda_i}}\}_{0 \leq i < |S|}) \times D^\dagger\,, \tag{5.7}$$

$$W_{\mathrm{ON}} = S^{-\frac{1}{2}} \times W\,, \tag{5.8}$$

where W is the matrix containing the vectors, that should to be orthogonalized and λ, D denote the eigenvalues and matrix containing the eigenvectors of the overlap matrix S respectively. Next the remaining basis states are orthogonalized with respect to this first block of states, spanned by $\mathcal{B}_{\mathrm{corr}}$, and to

each other using the Gram-Schmidt orthonormalization scheme. The basis is now fully orthonormalized and contains the orbitals $\mathcal{B}_{\text{corr}}$ for which coulomb repulsion will be added explicitly later. To construct the ligand orbitals the Hamiltonian is block-band diagonalized with respect to $\mathcal{B}_{\text{corr}}$. This is done by calculating a Krylov basis with the n-th order ligands being given as

$$\mathcal{L}_n^0 := H_{\text{DFT}}^n \mathcal{B}_{\text{corr}} \,. \tag{5.9}$$

These orbitals are not orthonormal after the block band diagonalization and therefore orthonormalized again using Gram-Schmidt orthonormalization. The DFT-Hamiltonian is transformed to this basis and the sub-Hamiltonian acting within each set of ligands is diagonalized individually, yielding the final ligand orbitals $\mathcal{L}_n$. The DFT-Hamiltonian in this basis is shown in figure 5.6, where the structure of the Krylov basis is well visible. The average onsite energies of coppers' 3d and central fluorine's 2s and 2p orbitals, as well as of all sets ligand orbitals $\mathcal{L}_{1\leq i\leq 9}$ are shown in table 5.4. The first set of 19 ligand orbitals is plotted in figure 5.7.

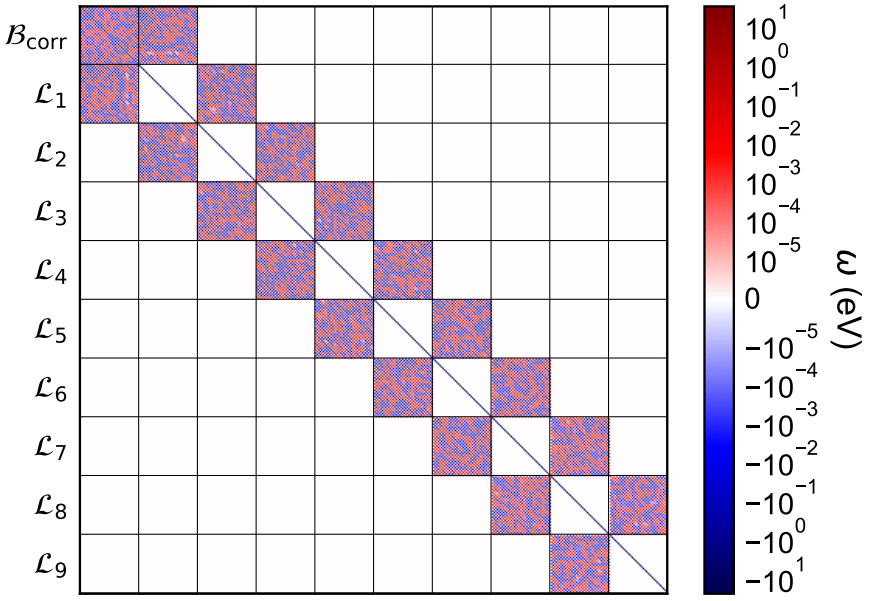


Figure 5.6: Matrix plot of the Hamiltonian obtained by DFT (TPSSh,*def2-TZVP*) in the ligand basis described in the text. $\mathcal{B}_{\text{corr}}$ encompasses the Cu 3d, μ_3−F2s and 2p orbitals. $\mathcal{L}_n$ denotes the set of n-th order ligand orbitals.

Orbitals	$\langle\epsilon\rangle_{\mathcal{B}}$ (eV)	Orbitals	$\langle\epsilon\rangle_{\mathcal{B}}$ (eV)
Cu 3d	−6.0437	$\mathcal{L}_4$	−19.2434
μ_3−F 2s	−27.2195	$\mathcal{L}_5$	−17.2899
μ_3−F 2p	−8.1346	$\mathcal{L}_6$	−13.0901
$\mathcal{L}_1$	−13.4377	$\mathcal{L}_7$	−10.4065
$\mathcal{L}_2$	−15.2388	$\mathcal{L}_8$	−9.8620
$\mathcal{L}_3$	−14.2075	$\mathcal{L}_9$	−9.2393

Table 5.4: Average onsite energy $\langle\epsilon\rangle_{\mathcal{B}}$ of the coppers' 3d, central fluorine's 2s and 2p shell, as well as, of the all sets of ligand orbitals.

5.2.2 Calculation of Slater-Integrals for the Coulomb Interaction

To determine the matrix elements of the coulomb interaction U_{ijkl} between electrons, which are initially in states i, j and scatter to states k and l, one has to perform the 6-dimensional integral

$$U_{ijkl} = \langle ij| \frac{\mathrm{e}^2}{|r_1 - r_2|} |kl\rangle \,, \tag{5.10}$$

where the position of the electrons is denoted by r_1 and r_2. On a basis of spherical harmonics times a radial wavefunction, this integral can be simplified by separating it's angular and radial parts [45]. The angular parts can be solved analytically, reducing the numerical complexity to a 1-dimensional integral [45, 74]. For the coulomb interaction within a single shell with angular momentum l, such as the copper's 3d shell, this radial integral is denoted by F^k_{ll}, where k denotes the angular momentum exchanged by the electrons. In the case of two shells (with angular momentum l_1 and l_2) and conservation of their respective occupations, the slater integrals can be separated into two categories. The first one being the direct exchange $F^k_{l_1 l_2}$, where both electrons stay in their initial shells and the second category is the indirect exchange $G^k_{l_1 l_2}$, where said electrons exchange places. The possible values for k are limited by conservation of angular momentum. For direct exchange (and therefore also F^k_{ll} with $l_1 = l_2 = l$) $k \in \{2 \cdot n | n \in \mathbb{N}_0 \wedge 0 \leq n \leq \mathrm{Min}(\mathrm{l}_1, \mathrm{l}_2)\}$ and for indirect exchange $k \in \mathbb{N}_0 \wedge |l_1 - l_2| \leq k \leq |l_1 + l_2|$, where the parity of k is the same as for $l_1 + l_2$.

To calculate the required Slater-integrals the atomic eigenstates of copper and fluorine are needed. These were constructed by means of DFT using *FPLO* (version 21.00-61) [75, 76]. The Perdew Wang 92 LDA functional was used, together with the internal basis set of *FPLO*, for the DFT calculations. These atomic orbitals were then input into a *quanty* [77] script and the Slater-integrals were calculated. The resulting integrals are shown in table 5.5. To combine the Slater-integrals with the basis functions in $\mathcal{B}_{\mathrm{corr}}$ to a many-body Hamiltonian, the values of the integrals have to be slightly adjusted. This need arises from cutting off states outside the energy window specified in section 5.2.1 and the orthonormalization of these orbitals. These changes lead to a reduced atomic character for these states and therefore the applied coulomb interaction has, in principle, to be reduced as well. This adjustment of the Slater-integrals amount to 0.27% for Cu, 0.50% for F 2s and 1.39% for F 2s.

Atom	Cu			F				
Slater-Integral	F^0_{dd}	F^2_{dd}	F^4_{dd}	F^0_{ss}	F^0_{pp}	F^2_{pp}	F^0_{sp}	G^1_{sp}
Value (eV)	25.24319	11.12082	6.82548	24.55740	23.16938	10.13673	23.76858	14.25107

Table 5.5: Slater-Integrals of the Coulomb interaction on Cu 3d, F 2s and 2p shells. The calculation was performed using *FPLO* (version 21.00-61) [75, 76] and *quanty* [77]. For more details see the text.

5.2.3 Coulomb Screening and Charge Transfer Energy

The Coulomb interaction calculated in section 5.2.2 only describes two electrons, for example in a 3d shell, but these two electrons are also affected by all the other electrons on the copper and the coordinating ligands. These other electrons cannot be included explicitly in the many-body calculation, due to computational costs, and therefore have to be described as an effective screening reducing the coulomb exchange between the two electrons. This screening cannot be calculated sufficiently accurate and therefore has to be taken as a free parameter, which is implemented as the Hubbard U_{H} [78]. U_{H} can be expressed in terms of the Slater-integrals for a 3d shell as

$$U^{\mathrm{3d}}_{\mathrm{H}} = F^0_{\mathrm{dd}} - \frac{2}{63}(F^2_{\mathrm{dd}} + F^4_{\mathrm{dd}}) \,. \tag{5.11}$$

The multipole parts of the coulomb interaction F^2_{dd} and F^4_{dd} are supposed to be less affected by the screening than the monopole part F^0_{dd} and therefore taken as fixed, leading F^0_{dd} to be varied as

$$F^0_{\mathrm{dd}} = U^{3\mathrm{d}}_{\mathrm{H}} + \frac{2}{63}(F^2_{\mathrm{dd}} + F^4_{\mathrm{dd}})\,. \tag{5.12}$$

For copper in the 2+ ionization state the Hubbard U_{H} usually as a value of $U_{\mathrm{H}}^{\mathrm{Cu}^{2+}3d} \approx 7.0\,\mathrm{eV}$ [79]. For the filled μ_3-F 2s and 2p shells it is assumed that the monopole part of the coulomb repulsion is sufficiently described by the DFT potential, so that only the multipole parts will be included explicitly in the many-body Hamiltonian.

Up to this point, only for the orbitals in $\mathcal{B}_{\mathrm{corr}}$ has Coulomb repulsion been included explicitly, which leads to an effective shift of the onsite energy of the affected orbitals. To compensate for this the charge-transfer energy Δ_{CT} is introduced as a second free parameter. For a given shell l with the electronic configuration l^n this energy is defined as

$$\Delta_{\mathrm{CT}} = E(l^{n+1}\underline{L}) - E(l^n)\,, \tag{5.13}$$

where $E(l^n)$ denotes the energy of the l^n configuration and $E(l^{n+1}\underline{L})$ the energy of the configuration with an additional electron on l and a hole on the ligand shell. With the average onsite energy ϵ_l of l and ϵ_L of the ligand shell Δ_{CT} can be expressed as

$$\Delta_{\mathrm{CT}} = \epsilon_l - \epsilon_L + n \cdot U_{\mathrm{H}}\,. \tag{5.14}$$

From equation 5.14 it can be ascertained, that Δ_{CT} fixes the the energy difference between the correlated shell l and the ligands L

$$\epsilon_l - \epsilon_L = \Delta_{\mathrm{CT}} - n \cdot U_{\mathrm{H}}\,. \tag{5.15}$$

This correction is only applied for the coppers' 3d shell, due to the monopole part of the coulomb interaction on the fluorine being neglected.

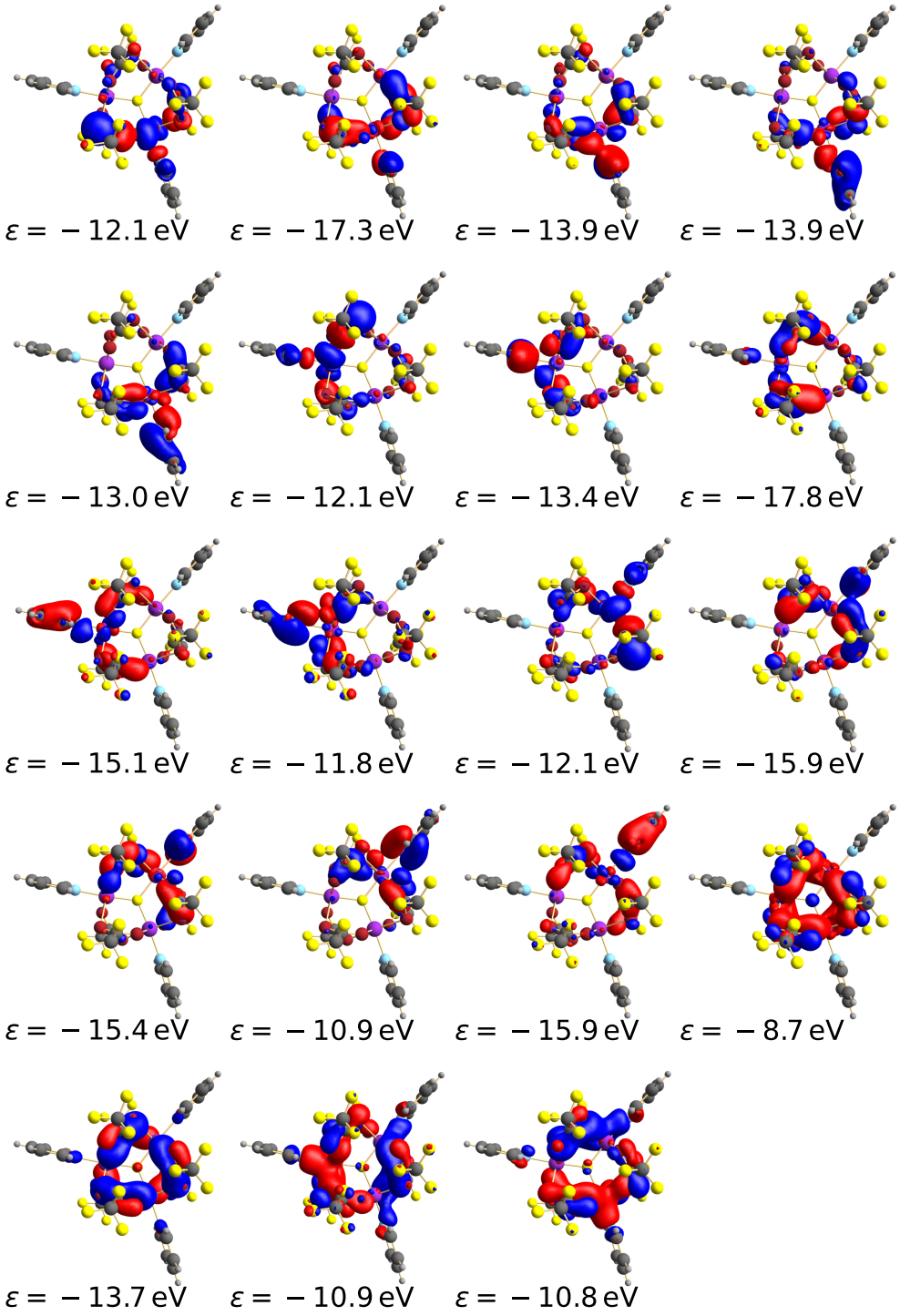


Figure 5.7: Isosurface plot of the first set of ligand orbitals constructed with DFT (TPSSh functional, *def2-TZVP* basis set) for CuΔ. The isosurface contains 80% of the orbitals density. The energy expectation value ϵ of the ligand with respect to the DFT-Hamiltonian is written below each subplot.

5.3 Full Many-Body Calculation of the Low Lying Multiplets

Performing the many-body calculations to determine the magnetic properties of CuΔ, requires restricting the one particle basis $\mathcal{B}_{\text{so}}$ to the correlated orbitals and ligands up to order n_{L} as indicated in section 5.2.1

$$\mathcal{B}_{\text{so}} = \mathcal{B}_{\text{coor}} \cup \bigcup_{n=1}^{n_{\text{L}}} \mathcal{L}_n \,, \tag{5.16}$$

yielding the total number of spin orbitals

$$N_{\text{so}} = |\mathcal{B}_{\text{corr}}| + \sum_{n=1}^{n_{\text{L}}} |\mathcal{L}_n| = (1 + n_{\text{L}}) \cdot |\mathcal{B}_{\text{corr}}| = 38(1 + n_{\text{L}}) \,. \tag{5.17}$$

In the energy window considered for the molecular orbitals (see section section 5.2.1) there are three holes in the MOs. This allows for the restriction of the many-body Hilbert space $\mathcal{H}_{\text{MB}}$ to those fock-states containing $N_{\text{so}} - 3$ electrons. The resulting Hilbert space has dimension

$$|\mathcal{H}_{\text{MB}}| = \binom{N_{\text{so}}}{N_{\text{so}} - 3} = \binom{N_{\text{so}}}{3} = \binom{38(1 + n_{\text{L}})}{3} \,. \tag{5.18}$$

In case of one ligand shell $|\mathcal{H}_{\text{MB}}| = 70300$ and in case of two ligand shells $|\mathcal{H}_{\text{MB}}| = 240464$.

The many-body Hamiltonian including the coulomb repulsion is given by

$$H_{\text{MB}} = \sum_{i,j \in \mathcal{B}_{\text{so}}} (H_{\text{DFT}})_{i,j} \, a_i^\dagger a_j + \sum_{i,j,k,l \in \mathcal{B}_{\text{corr}}} U_{i,j,k,l} a_i^\dagger a_j^\dagger a_k a_l + H_{\text{CT}} + H_{\text{SOC}} - H_{\text{DC}} \,, \tag{5.19}$$

where $a_{i \in \mathcal{B}_{\text{so}}}$ denotes the fermionic annihilation operator[18] acting on the spin orbital i and H_{DC} represents the double counting correction term discussed in section 5.3.1. H_{SOC} denotes the spin-orbit coupling acting on each Cu 3d and μ_3-F2p shell.

$$H_{\text{SOC}} = \xi_{\text{Cu3d}^9} \sum_{i \in \mathcal{B}_{\text{3d}}} \vec{l_i} \vec{s_i} + \xi_{\text{F2p}} \sum_{i \in \mathcal{B}_{\text{2p}}} \vec{l_i} \vec{s_i} \,, \tag{5.20}$$

where $\vec{l_i}$ and $\vec{s_i}$ denote the one electron orbital and spin operators acting on spin-orbital i respectively. The SOC coupling constant for copper is taken as $\xi_{\text{Cu3d}^9} = 0.102\,\text{eV}$ [31] and for the fluorine's 2p shell it is approximated as $\xi_{\text{F2p}} = 0.034\,\text{eV}$ [80]. However SOC is insignificant for F^- since the 2p shell is completely filled, therefore is the impact of ξ_{F2p} negligible. The charge-transfer correction (see equation 5.15) is contained in H_{CT} and it is given by

$$H_{\text{CT}} = \left(\frac{\text{Tr}((H_{\text{MB}} - H_{\text{CT}})|_{B_{\text{so}} \setminus B_{\text{3d}}})}{N_{\text{so}} - |\mathcal{B}_{\text{3d}}|} - \frac{\text{Tr}((H_{\text{MB}} - H_{\text{CT}})|_{\mathcal{B}_{\text{3d}}})}{|\mathcal{B}_{\text{3d}}|} + \Delta_{\text{CT}} - 9U_{\text{H}} \right) \sum_{i \in \mathcal{B}_{\text{3d}}} a_i^\dagger a_i \,. \tag{5.21}$$

The tight binding Hamiltonian, given by H_{DFT}, can also be expressed in it's canonical form as

$$H_{\text{DFT}} = \sum_{i \in \mathcal{B}_{\text{so}}} \epsilon_i a_i^\dagger a_i + \sum_{i,j \in \mathcal{B}_{\text{so}}, i \neq j} t_{i,j} a_i^\dagger a_j \,, \tag{5.22}$$

where ϵ_i denotes the onsite energy of orbital i and $t_{i,j}$ represents the hopping from orbital j to i.

Calculating the magnetic properties of CuΔ, which were measured in section 4.2, only requires the systems ground state as well as the first set of spin excitation. This amounts to the lowest eight eigenstates, due to the presence of three holes. This set of eigenstates was calculated using the quantum script language *quanty* [77]. Initially only the mean-field Hamiltonian is diagonalized, to obtain a set of initial guesses

[18] $a_{i \in \mathcal{B}_{\text{so}}}$ fulfills the anti-commutation relations: $\{a_i, a_j^\dagger\} = a_i a_j^\dagger + a_j^\dagger a_i = \delta_{i,j}$ and $\{a_i, a_j\} = \{a_i^\dagger, a_j^\dagger\} = 0$.

for the diagonalization of the many-body Hamiltonian with $U_{i,j,k,l} \neq 0$. The parameters U_{H} and Δ_{CT} are then varied and the corresponding eigenfunctions are used as a starting vector for *quanty's* "Eigensystem" function. Using the wavefunctions from previous iterations can significantly reduce the computational cost of determining the next set of eigenstates. The convergence limit is given by the relative variance of the energy and it is set to $\langle (H_{\mathrm{MB}} - \langle H_{\mathrm{MB}} \rangle)^2 \rangle / \langle H_{\mathrm{MB}} \rangle^2 \leq 10^{-10}$. Additionally before each calculation the trace of the Hamiltonian is shifted, such that the ground state has an energy of $E_0 \approx -5\,\mathrm{eV}$, ensuring a consistent accuracy goal. Thus the absolute variance for convergence is $\langle (H_{\mathrm{MB}} - \langle H_{\mathrm{MB}} \rangle)^2 \rangle \lesssim 2.5 \cdot 10^{-9}\,\mathrm{eV}$. With these settings a typical calculation of the eight lowest eigenstates for a given set of parameters takes $t^1_{\mathrm{CPU}} \approx 30\,\mathrm{min}$ for $n_{\mathrm{L}} = 1$ and $t^2_{\mathrm{CPU}} \approx 200\,\mathrm{min}$ for $n_{\mathrm{L}} = 2$ on 20 threads of an Intel® E5-2697 processor.

5.3.1 Double-Counting and Self-Interaction Correction

The influence of the Coulomb-interaction is treated on a mean-field level in DFT, therefore adding Coulomb interaction explicitly as well effectively leads to the problem of double counting the Coulomb-repulsion between electrons. It is therefore necessary to subtract the double counted contribution to the Hamiltonian.

The simplest possibility is to consider the shift in onsite energy induced by U_{H} and subtract the double counted part

$$H_{\mathrm{DC,OS}} = \left(\frac{1}{2} U_{\mathrm{H}} - \delta_{\mathrm{CT}} \right) \sum_{i \in \mathcal{B}_{3\mathrm{d}}} a_i^\dagger a_i \,, \tag{5.23}$$

where some correction δ_{CT} is included for the specific implementation of the exchange-correlation functional in the DFT calculation. This kind of double counting correction does little more, than shift the energy of the correlated orbitals with respect to the ligands. The charge-transfer energy Δ_{CT} does exactly the same and therefore is this correction already included in H_{CT}.

Another possibility is to subtract mean-field versions of the coulomb operator from the total Hamiltonian. In *quanty* this is done by replacing the two-particle operators using the Hatree-Fock approximation [77]

$$\begin{aligned} a_i^\dagger a_j^\dagger a_k a_m \mapsto \mathrm{HFO}(a_i^\dagger a_j^\dagger a_k a_m) := \\ \left(\sum_{\substack{\sigma_1 \in \pi(\{i,j\}) \\ \sigma_2 \in \pi(\{k,l\})}} -\mathrm{sgn}(\sigma_1)\mathrm{sgn}(\sigma_2) a^\dagger_{\sigma_1(1)} a_{\sigma_2(1)} \langle a^\dagger_{\sigma_1(2)} a_{\sigma_2(2)} \rangle \right) - \langle a_i^\dagger a_m \rangle \langle a_j^\dagger a_k \rangle + \langle a_i^\dagger a_k \rangle \langle a_j^\dagger a_m \rangle \,, \end{aligned} \tag{5.24}$$

where $\pi(M)$ denotes the set of all permutations of the set M and $\langle a_i^\dagger a_j \rangle$ represents the i,j-th element of the electron density matrix obtained through the DFT calculation. Additionally one can correct for the self-interaction present in the DFT-calculation by subtracting the self-interaction energy [81, 82]. In the formalism used by *quanty* this is achieved by subtracting the average Coulomb-interaction and indirect exchange among the electrons of the affected orbitals. For a given Coulomb-operator $U = (U_{ijkl})_{i,j,k,l \in \mathcal{M}} : \mathcal{M}^2 \to \mathcal{M}^2$, $\mathcal{M} \cong \mathbb{C}^{n \in \mathbb{N}}$ this takes the form of [77]

$$H_{\mathrm{SIC}}(\mathcal{M}, U) = \left(\frac{2}{\langle n_{\mathrm{e}} \rangle (\langle n_{\mathrm{e}} \rangle - 1)} \sum_{k,l \in \mathcal{M}} (U_{kllk} - U_{klkl}) \right) \sum_{m,m' \in \mathcal{M}} \langle a_m^\dagger a_{m'} \rangle a_m^\dagger a_{m'} \,, \tag{5.25}$$

where $\langle n_{\mathrm{e}} \rangle$ denotes the total electronic occupation of the orbitals in consideration contained in $\mathcal{M}$. The total double counting and self-interaction correction is then given by

$$H_{\mathrm{DC,MF-SIC}}(U) = \sum_{\mathcal{M} \in \{\mathcal{B}_{3\mathrm{d,i}} | i=0,1,2\}} \left(\sum_{i,j,k,l \in \mathcal{M}} U_{ijkl} \cdot \mathrm{HFO}(a_i^\dagger a_j^\dagger a_k a_m) + H_{\mathrm{SIC}}(\mathcal{M}, U) \right) . \tag{5.26}$$

Here $\mathcal{B}_{3d,i}$ denotes the set of 3d orbitals of copper ion $i \in \{0,1,2\}$ and U the Coulomb-operator for which the correction should be applied. There is however an error in the 2022 autumn version of *quanty*, which meant, that only the diagonal terms, i.e $m = m'$ of equation 5.25 were included in the calculation of the self-interaction correction. This error leads to the loss of invariance under basis rotations of H_{SIC} and therefore a basis-dependent correction. This becomes most prevalent in low symmetry environments such as the copper ions in CuΔ. In the case of CuΔ this error indeed yields implausible results, as can be seen in figure 5.8(b). Here the hole density of the ground state multiplet is superimposed over the molecular structure of CuΔ. The lobes of the hole density point in between the coordinating anions, when it should be energetically more beneficial to have the lobes pointing towards the negatively charged ions, as observed without applying equation 5.26 (see figure 5.8(a)). Therefore the double counting correction given by equation 5.26 was omitted from further calculations.

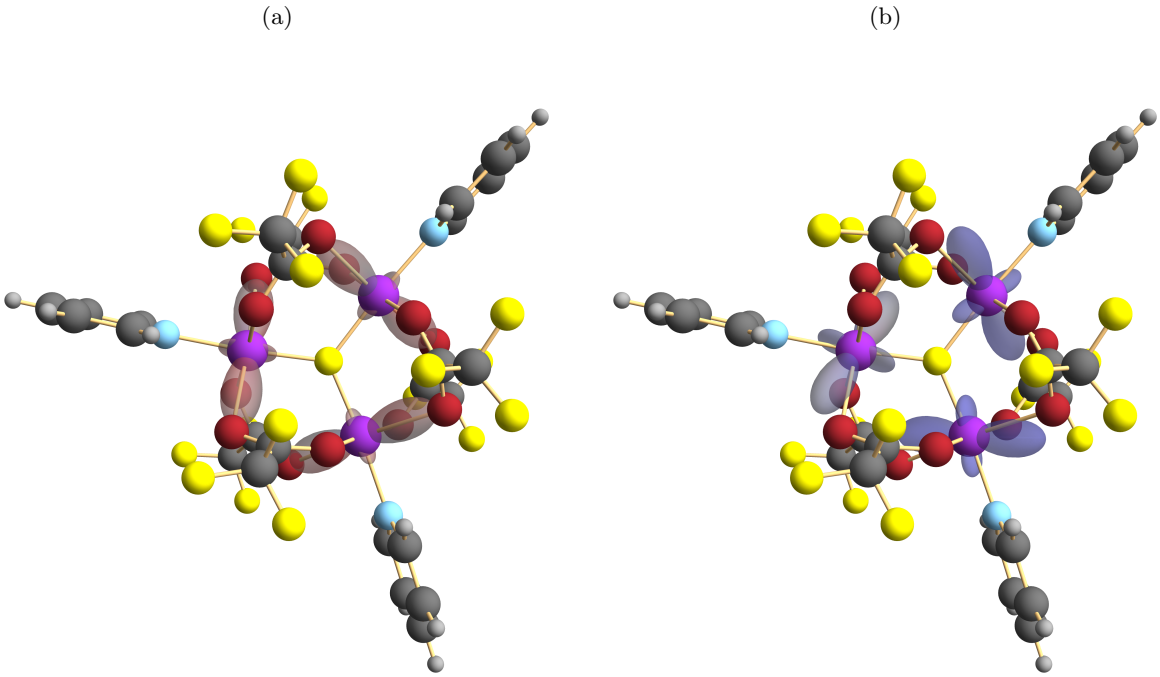


Figure 5.8: ground state hole-density at zero field ($B = 0\,\text{T}$) superimposed over the molecular structure of CuΔ for parameters $U_{\text{H}} = 6\,\text{eV}$ and $\Delta_{\text{CT}} = 9\,\text{eV}$. The double counting and self-interaction correction (equation 5.26) was applied for (b) and omitted for (a). The color of the density lobes indicate the spin orientation along the c-axis with red denoting completely spin up and blue spin down. Due to $B = 0\,\text{T}$ however is this coloring relatively meaningless, due to the degenerate nature of the ground state. The hole-density is enlarged by a factor of 6 for better visibility.

5.3.2 Influence of Correlations of $\mu_3-\text{F}$

The coulomb exchange was successively included on the μ_3-F2s and 2p shells to quantify the influence of correlations on these shells on the spin-spin exchange. Four calculations were performed with F^2_{pp} and G^1_{sp} being either zero or their calculated values (see section 5.2.2). The eigenenergies at zero field for $U_{\text{H}} = 6\,\text{eV}$ and $\Delta_{\text{CT}} = 9\,\text{eV}$, as well as the spin expectation values are plotted in figure 5.9. Without Coulomb exchange on the central fluorine the spins are coupled strongly antiferromagnetic with a High-Spin/Low-Spin gap of $E_{\text{HS}-\text{LS}} \approx 1100\,\text{GHz}$. Turning on the Coulomb exchange on the 2p shell promotes ferromagnetic couplings. The indirect exchange between the 2s and 2p shell decreases $|E_{\text{HS}-\text{LS}}|$ drastically for $F^2_{\text{pp}} = 0\,\text{eV}$ and $F^2_{\text{pp}} = 10.09\,\text{eV}$. The significance of explicit Coulomb-exchange for the magnetic

interactions can be understood in the context of the GKA[19]-rules (chapter 7 of [87]). For a Hubbard type model of a 180° super-exchange path between half filled orbitals, second order perturbation theory yields the spin-spin interaction (equation 42 in [87])

$$J = \frac{4t_{\mathrm{pd}}^4}{(U_{\mathrm{d}} + \Delta_{\mathrm{pd}})^2} \left(\frac{1}{U_{\mathrm{d}}} + \frac{1}{U_{\mathrm{d}} + \Delta_{\mathrm{pd}}} \right) , \tag{5.27}$$

where t_{pd} denotes the hopping and $\Delta_{\mathrm{pd}} = \epsilon_{\mathrm{d}} - \epsilon_{\mathrm{p}}$ represents the onsite-energy difference between the connecting p-orbital and the half filled d-orbital. U_{d} denotes the Hubbard-U acting on the d-shell. This coupling is usually antiferromagnetic. However for right-angled superexchange paths the spin-spin interaction is given by equation 47 in [87]

$$J = -\frac{4t_{\mathrm{pd}}^4}{(U_{\mathrm{d}} + \Delta_{\mathrm{pd}})^2} \frac{2J_{\mathrm{xy}}}{4(U_{\mathrm{d}} + \Delta_{\mathrm{pd}})^2 - J_{\mathrm{xy}}^2} , \tag{5.28}$$

where J_{xy} denotes the Coulomb-exchange integral between the connecting $\mathrm{p_x}$ and $\mathrm{p_y}$ orbitals (see equation 11 in [87]). This exchange is mediated by the Coulomb-interaction between the two p shells involved. For angles $90° < \alpha < 180°$ both mechanism (equations 5.27 and 5.28) compete since hopping between both d-orbitals and p-orbitals becomes possible. However the 180° antiferromagnetic superexchange usually is significantly stronger than the ferromagnetic 90° superexchange [87, 88, 89], leading to the assumption, that ferromagnetism would only dominate for angles close to $\alpha \approx 90°$. On one hand, in the case of CuΔ and other μ_3-H (where H denotes a halogen atom) bonded Cu(II) tri-nuclear complexes [10], this apparently does not hold. On the other hand there exist several similiarly structured molecules with a μ_3-bridging OH instead of fluorine or chlorine [10], that exhibit antiferromagnetic coupling [59]. This leads to the conclusion that these kinds of TM[20]-(μ_3-X)-TM bonds offer much more nuanced effects than DFT or the GKA-rules imply. For the understanding of these effects Coulomb-interaction and therefore correlations appear to play a crucial role. There is, for example, the aspect that not only the holes of two TM-ions interact in the μ_3-X 2s and 2p shell, but also a third hole from the remaining TM-ion in the triangle. Similar bonds occur for example in Magnetite [90].

5.3.3 Influence of the Charge Transfer Energy Δ_{CT} and Hubbard U_{H}

To understand the influence of the Hubbard $U_{\mathrm{H}}^{\mathrm{3d}}$ and change-transfer energy Δ_{CT} on the Hamiltonian's zero field spectrum, several calculations with differing parameters were performed. U_{H} was swept in the range $5\,\mathrm{eV} \leq U_{\mathrm{H}} \leq 9\,\mathrm{eV}$ and Δ_{CT} was varied in the range $7\,\mathrm{eV} \leq \Delta_{\mathrm{CT}} \leq 12\,\mathrm{eV}$. The eigenenrgies and the spin state $\langle S^2 \rangle$ of the respective states are plotted in figure 5.10. Here one can observe, that U_{H} stabilizes the low-spin states with respect to the high-spin states, meaning that the energy of the predominantly antiferromagnetically coupled states decreases with increasing U_{H}. The charge-transfer energy stabilizes the ferromagnetic states, while simultaneously increasing the ionicity of the copper ions, as can be observed in figure 5.11. This decrease of covalency results in a decrease of the overall interaction strength, which is indicated by a reduction of the total splitting of the spin-multiplet. It has to be noted here, that the effective charge-transfer energy for the μ_3-F2p shell $\Delta_{\mathrm{CT}}^{\mathrm{2p}}$ is $\delta_1 = 5.2106\,\mathrm{eV}$ smaller than Δ_{CT} for one ligand shell and $\delta_2 = 6.0672\,\mathrm{eV}$ smaller for two ligand shells, i.e.

$$\Delta_{\mathrm{CT}}^{2p} = \Delta_{\mathrm{CT}} - \delta_{i \in \{1,2\}} . \tag{5.29}$$

This difference arises from the to the energy separation between the ligand shells and the μ_3-F2p shell.

[19] Goodenough[83, 84]-Kanomori[85]-Anderson[86]
[20] Transition metal

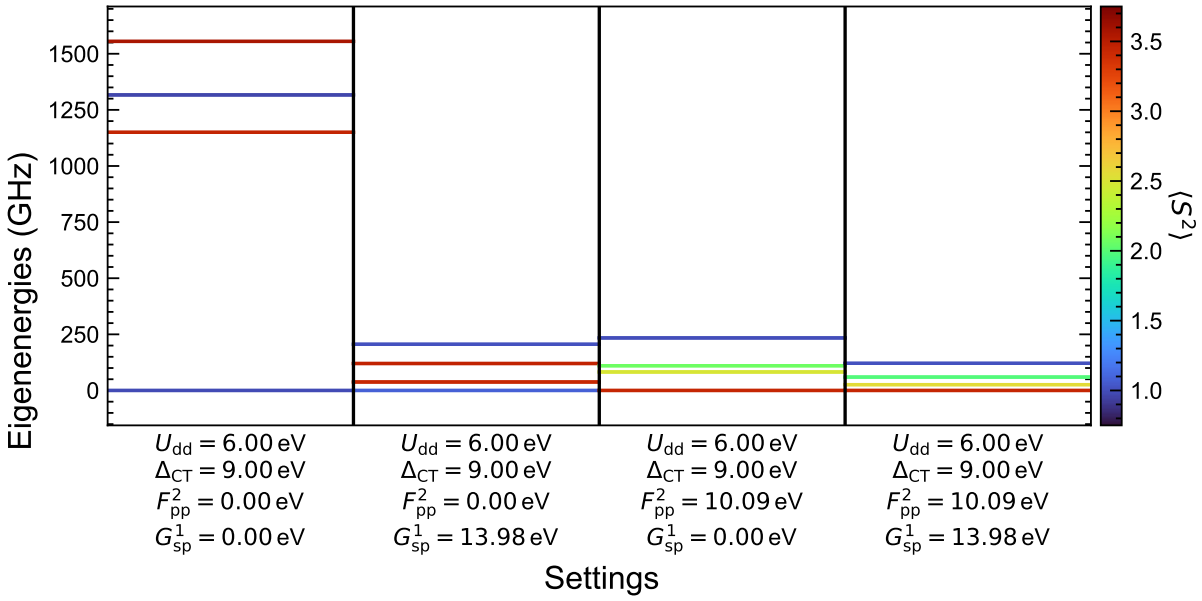


Figure 5.9: Energy level diagram for CuΔ at $B = 0\,\mathrm{T}$ calculated with one set of ligands and $U_\mathrm{H} = 6\,\mathrm{eV}$ and $\Delta_\mathrm{CT} = 9\,\mathrm{eV}$. The spin-expectation value $\langle S^2 \rangle$ of the individual states is indicated by coloring of the levels (see color-bar on the side). The multiple parts of the coulomb interactions for μ_3−F are successively activated.

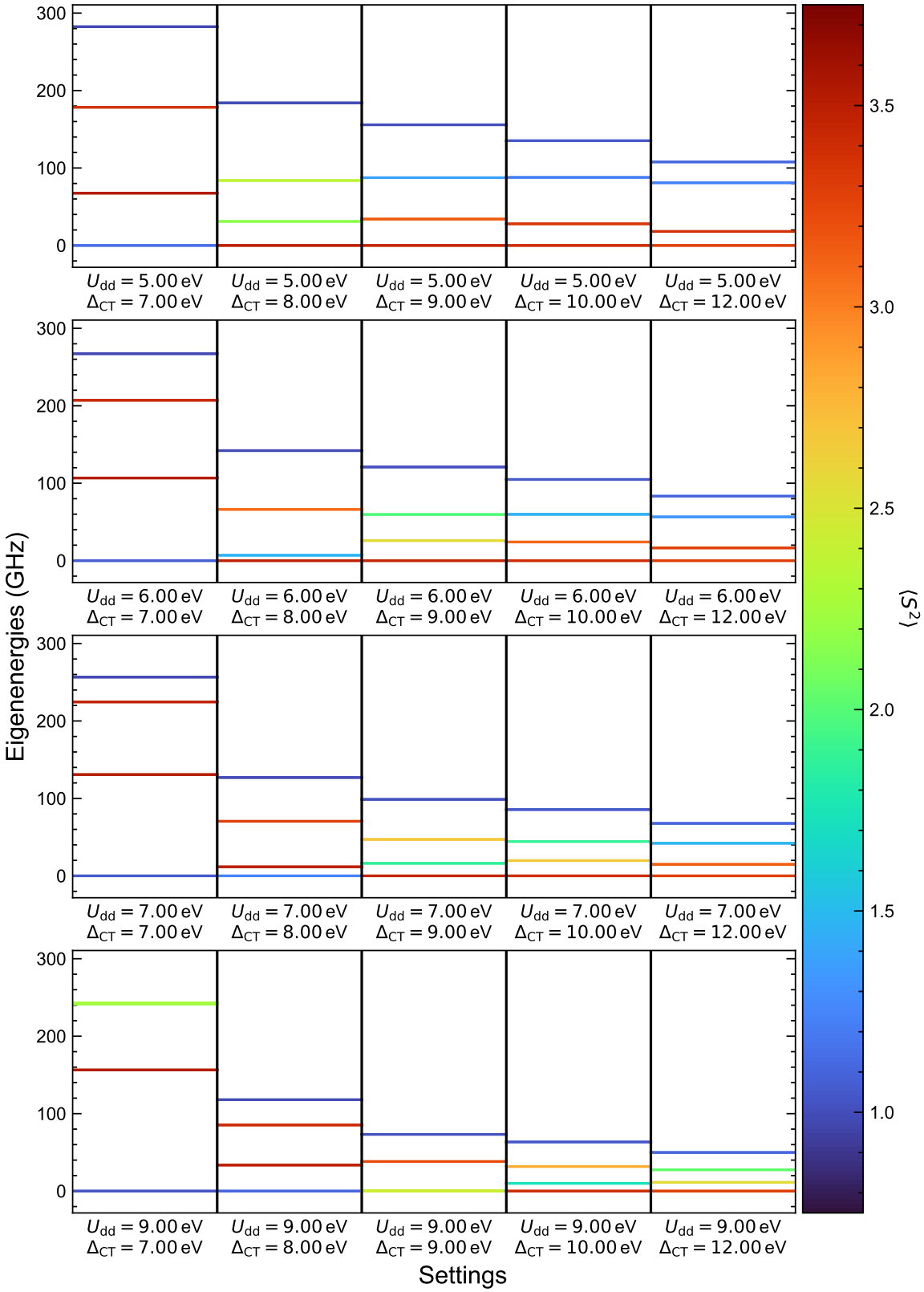


Figure 5.10: Energy level diagram for CuΔ at $B = 0\,\mathrm{T}$ calculated with one set of ligands and $5\,\mathrm{eV} \leq U_{\mathrm{H}} \leq 9\,\mathrm{eV}$ and $7\,\mathrm{eV} \leq \Delta_{\mathrm{CT}} \leq 12\,\mathrm{eV}$. The spin-expectation value $\langle S^2 \rangle$ of the individual states is indicated by coloring of the levels (see color-bar on the side).

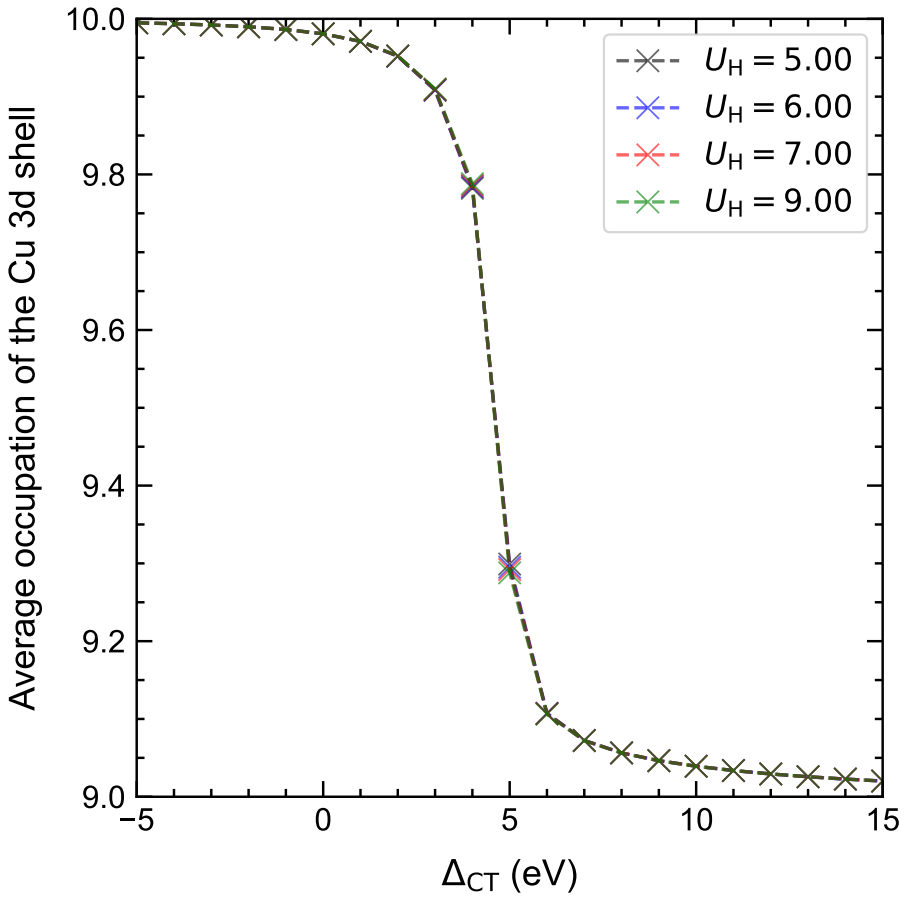


Figure 5.11: Average occupation of the coppers' 3d shell as a function of the applied charge transfer energy Δ_{CT} for $U_H \in \{5\,eV, 6\,eV, 7\,eV, 9\,eV\}$.

5.4 Projection of the Many-Body Results to an Effective Spin Hamiltonian

The calculation of magnetic properties, such as resonance-fields and magnetization, require multiple diagonalizations at different strengths and orientations of the external magnetic field. Repeating the full many-body calculations for each of the different field configurations is computationally very expensive and thus impractical. These costs can be drastically lowered however, by constructing a low energy effective model for any given parameter configuration (U_H and Δ_CT). The idea behind this construction is outlined in section 3.1.4. The first step is to project all relevant operators $O \in \mathcal{L}(\mathcal{H}_\mathrm{MB})$ defined in the many-body Hilbert space $\mathcal{H}_\mathrm{MB}$ to the Hilbert space $\mathcal{H}_\mathrm{SM}$ spanned by the lowest spin-multiplet. In the case of CuΔ these are the lowest eight eigenstates of the full Hamiltonian. The Operators are projected to $\mathcal{H}_\mathrm{SM}$ by recalculating their matrix elements for the wave functions contained in $\mathcal{H}_\mathrm{SM}$

$$(O|_{\mathcal{H}_\mathrm{SM}})_{i,j\in\mathcal{H}_\mathrm{SM}} = \langle i|O|j\rangle\,. \tag{5.30}$$

It has to be noted, that this projection is also quite expensive, due to the size of the involved wavefunctions. However then using these new operators reduces the complexity to the diagonalization of a complex eight-by-eight matrix for each field configuration. The total computational cost per parameter set consists of one many-body calculation, the actual projection and several diagonalizations of small matrices. The latter part being insignificant compared to the first two steps.

5.4.1 Calculation of Static Magnetic Properties and Resonance-Fields

To calculate the static magnetization $M(B,T)$ at a given temperature T and magnetic field B, the effective Hamiltonian H_eff, constructed before, is appended by adding the Zeeman-term $H_\mathrm{Zeeman} := \vec{G}\vec{B}$

$$H_\mathrm{eff} = H_{B=0\,\mathrm{T}} + \vec{G}\vec{B} = H_{B=0\,\mathrm{T}} + \sum_k \mu_\mathrm{B}(L_k|_{\mathcal{H}_\mathrm{SM}} + 2S_k|_{\mathcal{H}_\mathrm{SM}})\cdot B_k\,. \tag{5.31}$$

The resulting Hamiltonian is then diagonalized and the thermal expectation value of the magnetic moment parallel to the external B-field is calculated

$$\langle m(\vec{B})\rangle_T = \frac{\sum_i \langle i|m(\vec{B})|i\rangle \exp\left(-\frac{E_i}{k_\mathrm{B}T}\right)}{\sum_i \exp\left(-\frac{E_i}{k_\mathrm{B}T}\right)} = \frac{\sum_i \langle i|\vec{G}\frac{\vec{B}}{|\vec{B}|}|i\rangle \exp\left(-\frac{E_i}{k_\mathrm{B}T}\right)}{\sum_i \exp\left(-\frac{E_i}{k_\mathrm{B}T}\right)}\,, \tag{5.32}$$

with $E_i := \langle i|H_\mathrm{eff}|i\rangle$. In order to construct the solid-angle averaged magnetization, the angles are sampled in a range of $0° \le \theta \le 180°$ for the polar angle and $0° \le \varphi \le 120°$ for the azimuthal angle. The azimuthal angle only has to be sampled on a third of the total azimuth due to the C_3 symmetry of the molecule. This step is repeated for all sampled field directions and the resulting magnetization is averaged. This averaging is weighted by the appropriate spherical area element corresponding to each solid angle.

For $U_\mathrm{H} = 6\,\mathrm{eV}$ ($U_\mathrm{H} = 7\,\mathrm{eV}$) and $\Delta_\mathrm{CT} = 9\,\mathrm{eV}$ calculated isothermal magnetization curves at 2 K, 5 K and 10 K are shown in figure 5.13(a) (5.12(a)). The slope of the calculated curves is larger compared to the slope of the measured curves (figure 4.19(a)), indicating an underestimation of the anisotropc exchange relative to the isotropic exchange. This is supported by the static susceptibility times temperature (plotted in figures 5.13(b) and 5.12(b)). Here the observed maximum sits well below the measured position (see figure 4.18). It can also be observed, that increasing U_H suppresses the peak in the calculated $\chi T = \frac{MT}{B}|_{B=\mathrm{const}}$ curves.

To construct resonance-field diagrams from the Hamiltonian (equation 5.31), eigenenergies at different field configurations $\vec{B}$ are first calculated. Due to all measured resonance-features being deemed ground

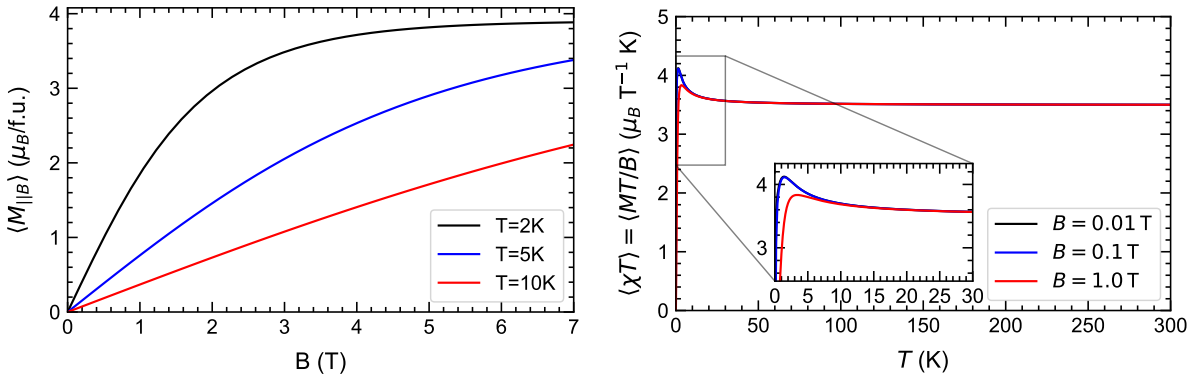


Figure 5.12: Calculated (a) isothermal magnetization and (b) static susceptibility curves for CuΔ at $U_H = 7\,\text{eV}$ and $\Delta_{CT} = 9\,\text{eV}$.

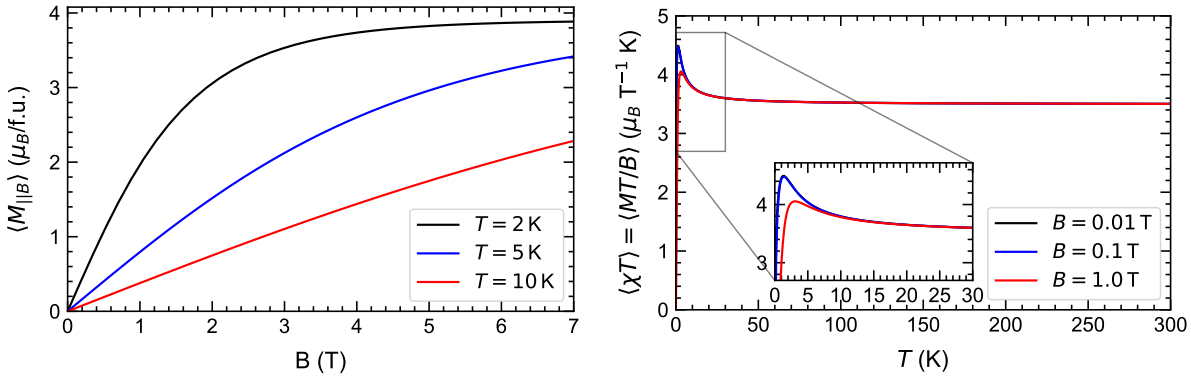


Figure 5.13: Calculated (a) isothermal magnetization and (b) static susceptibility curves for CuΔ at $U_H = 6\,\text{eV}$ and $\Delta_{CT} = 9\,\text{eV}$.

state transitions, are the resonance branches given by the energy difference between the ground state and remaining states. For the parameters $U_H = 6\,\text{eV}$ and $\Delta_{CT} = 9\,\text{eV}$ such resonance field diagrams are plotted in figure 5.14 at various angles φ and θ of the external magnetic field. The angles φ (θ) are defined with respect to the a-axis (c-axis) as the azimuthal (polar) angles. The corresponding energy-level diagrams are plotted in figure 5.15 alongside the spin expectation value $\langle S^2 \rangle(B)$ for each eigenstate at all values of $|B|$. The lowest three calculated resonance branches generally exhibit some features of the experimental branches. Namely that they undergo a similar reduction of their slope for increasing fields. The origin of this behavior is explained as follows: The spin-multiplet is split into four doublets at $B = 0\,\text{T}$, where the ground state doublet is formed by two high-spin states. One of these two states mixes at $B \approx 0.8\,\text{T}$ with states from the two next doublets, leading to a reduction of the resonance frequency of the first transition as B increases further. The states of these two doublets also mix, forming the second and third resonance branches. At $\varphi = 0°$ and $\theta = 67.5°$ (figure 5.14(d)) the second and third resonance branches start at different slopes for $B \lesssim 3\,\text{T}$ and continue parallel to higher fields. This behavior analogous to the one observed experimentally for branches A and D. Although the most prevalent resonances and the behavior, indicated before, could be reproduced qualitatively, there are significant quantitative differences. First and foremost that the calculated effective g-factors are to large for all branches and angles, except for branch F at $\varphi = 0°$ and $45° \lesssim \theta \lesssim 67.5°$ (figures 5.14(c) and 5.14(d)). This overestimation of effective g-factors can be explained by an underestimation of the effective crystal-field splitting, as discussed in section 3.1.1. A possible reason for this could be the missing double-counting/self-interaction correction, as discussed in section 5.3.1.

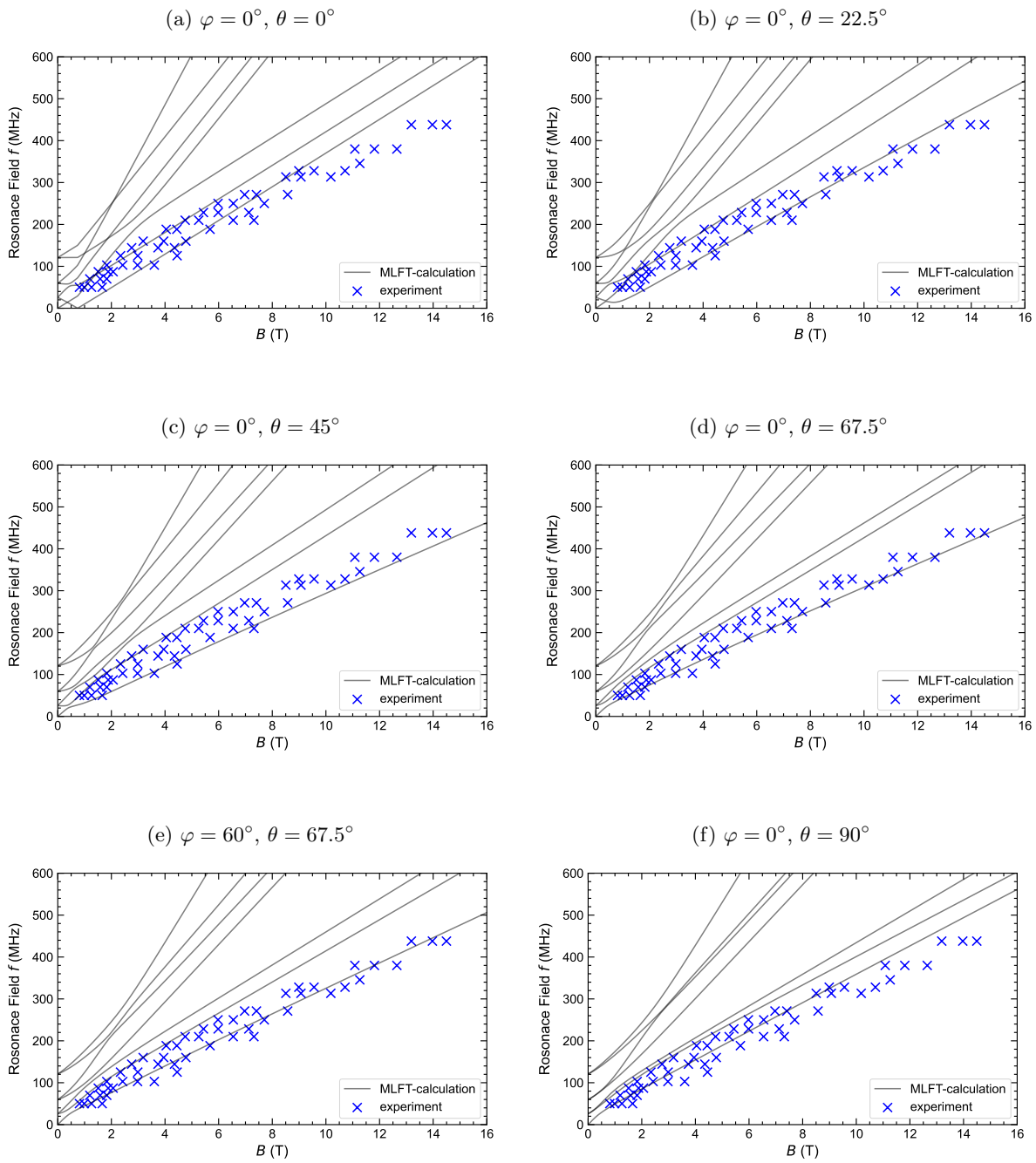


Figure 5.14: Calculated ground state resonance branches overlayed over the experimentally observed resonances. The resonance branches were calculated with respect different orientations of the magnetic field marked by the angles φ and θ. The angle φ (θ) is defined with respect to the a-axis (c-axis). The parameters $U_{\mathrm{H}} = 6\,\mathrm{eV}$ and Δ_{CT} were used for the many-body calculation.

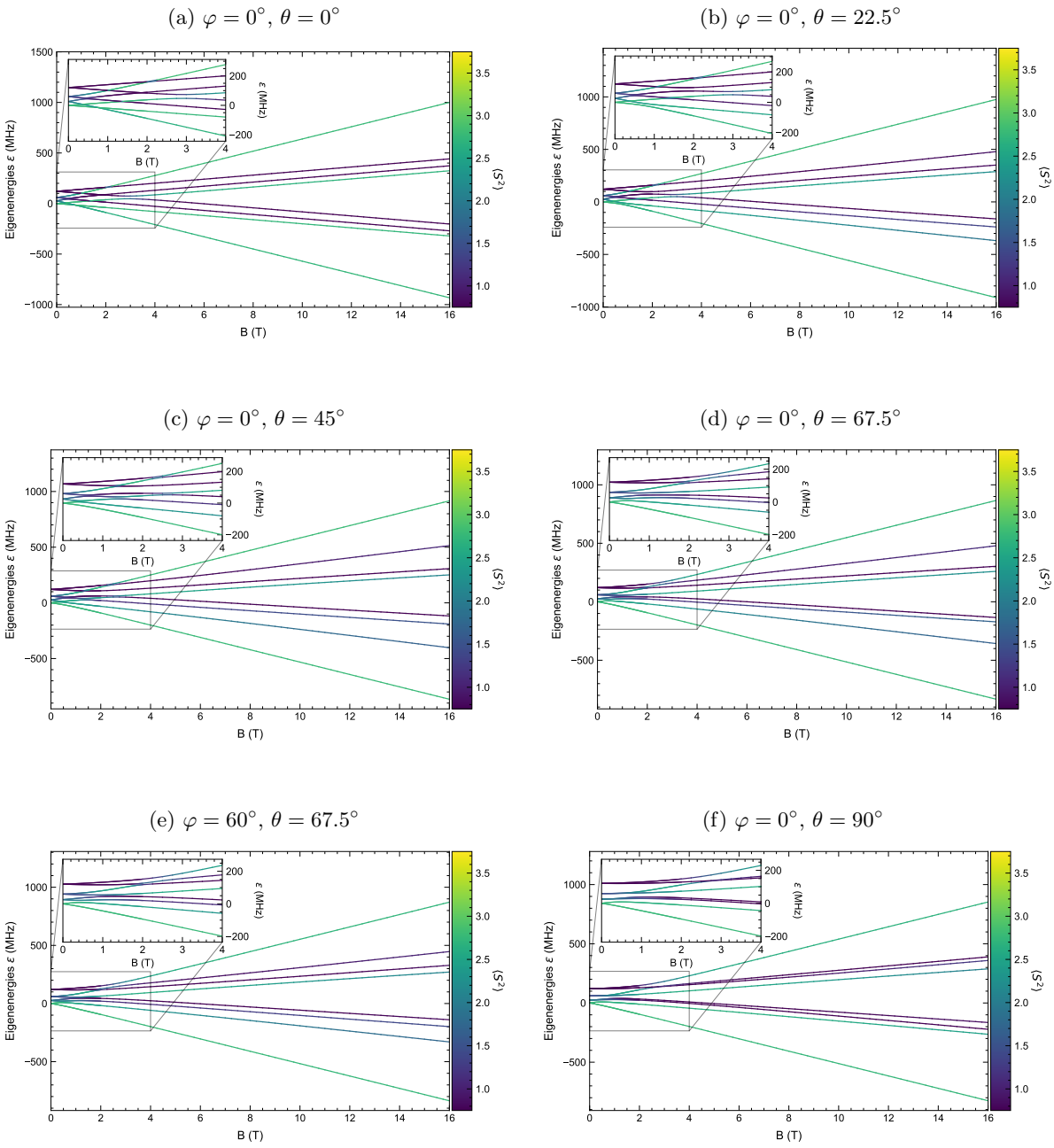


Figure 5.15: Calculated ground state resonance branches, that were calculated with respect different orientations of the magnetic field marked by the angles φ and θ. The angle φ (θ) is defined with respect to the a-axis (c-axis). The color of the plotted lines, indicates the expectation value of $\langle S^2 \rangle$ at that field strength $|B|$. The parameters $U_H = 6\,\text{eV}$ and Δ_{CT} were used for the many-body calculation.

5.4.2 Construction of a Spin-Hamiltonian

To quantify the contributions of isotropic exchange, DM- and Kitaev-interaction to the total spin-spin exchange, as well as the the local g-factors, the effective low energy Hamiltonian H_{eff} is mapped to a spin-Hamiltonian H_{SH}. This is achieved by first projecting H_{eff} to permutations of the projected spin-Operators $S|_{\mathcal{H}_{\text{SM}}}$ as described in section 3.1.4. However these projected spin-Operators need to be conditioned, before a meaningful result can be obtained. This starts by removing any non-hermitian parts of $S|_{\mathcal{H}_{\text{SM}}}$, which could be present due to, for example, floating point errors

$$(S_i^{k_i})' = \frac{S_i^{k_i}|_{\mathcal{H}_{\text{SM}}} + S_i^{k_i}|_{\mathcal{H}_{\text{SM}}}^\dagger}{2}\,, \tag{5.33}$$

where i denotes the site and k_i the direction of which the spin operator $S_i^{k_i}$ acts. Next the spin operators are scaled, such that they have eigenvalues $\lambda \approx \pm\frac{1}{2}$, as their magnitude is reduced as stated in section 3.1.4. In the next step for non-local two-spin operators the canonical commutation relations are enforced by taking the anti-commutator instead of the direct product

$$(S_i^{k_i} S_j^{k_j})'' = \frac{\{(S_i^{k_i})', (S_j^{k_j})'\}}{2} = \frac{(S_i^{k_i})'(S_j^{k_j})' + (S_j^{k_j})'(S_i^{k_i})'}{2} = (S_j^{k_j} S_i^{k_i})''\,. \tag{5.34}$$

This is necessary, because $[(S_i^{k_i})', (S_j^{k_j})'] \neq 0$ for the projected spin-Operators at two sites $i \neq j$ and for directions k_i and k_j respectively, which arises from projecting to an incomplete basis. In general does the commutation of two block matrices not imply that their sub-matrices commute as well

$$0 = \left[\begin{pmatrix} A & B \\ C & D \end{pmatrix}, \begin{pmatrix} A' & B' \\ C' & D' \end{pmatrix}\right] = \begin{pmatrix} AA' - A'A + BC' - B'C & ... \\ ... & ... \end{pmatrix} \tag{5.35}$$

$$\nRightarrow AA' - A'A = [A, A'] = 0\,, \tag{5.36}$$

where $A, A' \in \mathbb{C}^{n_A \times n_A}$, $B, B' \in \mathbb{C}^{n_A \times n_D}$, $C, C' \in \mathbb{C}^{n_D \times n_A}$ and $D, D' \in \mathbb{C}^{n_D \times n_D}$. The last necessary step is to orthogonalize all $1, 2, ...n$-spin-Operators, because non-orthogonal projections loose their meaning and potentially their uniqueness. This step has the potential to significantly change the spin operators, due to this a hierarchy for the orthogonalization is enforced, with the Operators deemed more significant being given priority. In the case of CuΔ only 1-,2- and 3-spin-Operators can play a role and since one is usually most interested in the g-factors and spin-spin exchange these operators are placed above the three spin operators in this hierarchy. Therefore the 1- and 2-spin operators are first Löwdin orthogonalized individually and then to one another. Lastly are the 3-Spin operators added and all operators are Gram-Schmidt orthogonalized, with the 1- and 2-spin-operators constituting the fist block. These conditioned operators $\overline{S_i^{k_i}}$, $\overline{S_i^{k_i} S_j^{k_j}}$ and $\overline{S_i^{k_i} S_j^{k_j} S_l^{k_l}}$ now form a cpmplete orthogonal basis of $\mathbb{C}^{64} \cong \mathbb{C}^{8\times 8} \ni H_{\text{eff}}$. Rotating H_{eff} to this basis yields the parameters for the spin-Hamiltonian. It has to be noted that in order to gain access to the g-tensors this projection has to be repeated for three orthogonal orientations for $B > 0$, each of these orientations yield three entries of a local g-tensor. For example considering $\vec{B} = (B_0, 0, 0)^T$ the Zeeman-term, encompassing the 1-spin-operators, is reduced to

$$\vec{G}\vec{B} = \mu_{\text{B}} B_0 \left(S^x g_{xx} + S^y g_{yx} + S^z g_{zx}\right)\,. \tag{5.37}$$

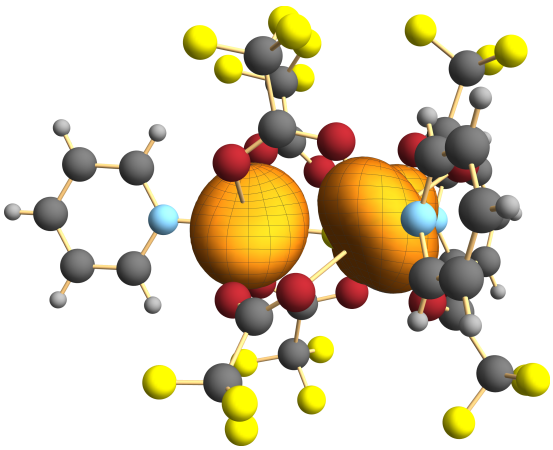
So that only g_{xx}, g_{yx} and g_{zx} can be obtained.

The resulting parameters for CuΔ and different parameter sets are shown in table 5.6. Here the principle values of the g-tensor, the isotropic exchange and the magnitude of DMI ant the Kitaev-interaction are included. The same trends as in section 5.3.3 can be observed. Δ_{CT} stabilizes the ferromagnetic states, while U_{H} stabilizes the antiferromagnetic states. There is indeed a phase-boundary between dominant antiferromagnetic and ferromagnetic interactions, also implying that decreasing Δ_{CT} far enough leads

to strong AF exchange, as indicated in table 5.6. In the ferromagnetic regime DMI is suppressed and Kiteaev-exchange promoted by Δ_{CT}, while U_H suppresses $\underline{\underline{K}}$ and promotes DMI. The principle values of the g-tensor are mainly impacted by the charge transfer energy. The shapes of the local g-tensor and total g-tensor are sketched in figures 5.16 and 5.17 respectively. Here one can observe, that the principle axes of the local g-tensor roughly correspond to the bonds around the copper ions. The two higher principle g-factors are oriented like the singly occupied HOMOs from the DFT-calculations. The total g-tensor is the sum of all local g-factors and therefore is shaped like and elongated ellipsoid with two roughly identical axes and a larger axis, that is oriented along the c-axis. The calculated g-tensors are highly anisotropic and have principle g-factors not in the usual range for Cu^{2+} [57, 58, 59, 10], which stem from wrong effective crystal field splittings. This could potentially be attributed to the missing double-counting/self-interaction correction, as stated in section 5.4.1.

The spin expectation values, plotted as a classical vector $\langle \vec{S}_i \rangle|_{i=0,1,2}$, are shown superimposed over the hole density on the copper ions and molecular structure in figure 5.18. To relieve the spin-degeneracy at zero field, a small field of $B = 1\,\mathrm{mT}$ was applied along the c-axis. The plot was constructed directly from the many-body calculation. In figure 5.18 the influence of the anisotropic exchange can be observed in the orientation of the individual spins, which are arranged in a chiral manner. The preferred direction is similar to the highest principle value of the g-tensor (see figure 5.16).

(a) View along a-axis



(b) View along c-axis

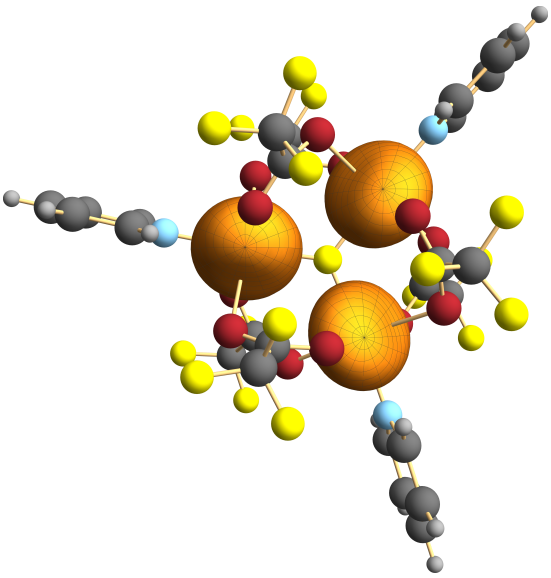


Figure 5.16: Contour plot illustrating the local g-tensors of CuΔ, as calculated with the parameters $U_H = 6\,\mathrm{eV}$ and $\Delta_{CT} = 9\,\mathrm{eV}$. The distance of the contour to the corresponding copper ion is proportional to the g-factor along that axis. CuΔ (a) viewed along the a-axis and (b) viewed along the c-axis.

U_{H} (eV)	Δ_{CT} (eV)	g_1	g_2	g_3	J_{iso} (K)	$\|\|\underline{\underline{D}}\|\|_2$ (K)	$\|\|\underline{\underline{K}}\|\|_2$
3.0	5.0	1.32	1.78	2.08	126.12	43.98	19.63
3.0	7.0	1.78	2.69	2.80	−17.85	1.13	1.48
3.0	8.0	1.82	2.69	2.96	−16.34	0.58	1.69
3.0	9.0	1.84	2.69	3.09	−15.28	0.63	1.94
3.0	15.0	1.85	2.61	3.56	−17.08	0.48	6.31
5.0	5.0	1.36	1.83	2.15	131.73	30.11	21.05
5.0	7.0	1.78	2.70	2.80	−3.60	1.59	0.95
5.0	8.0	1.82	2.70	2.96	−4.71	0.58	0.80
5.0	9.0	1.85	2.69	3.09	−4.79	0.18	0.80
5.0	15.0	1.85	2.62	3.56	−5.44	0.19	2.74
6.0	5.0	1.37	1.84	2.16	131.30	26.73	21.43
6.0	7.0	1.79	2.69	2.80	−1.03	1.64	0.85
6.0	8.0	1.82	2.69	2.96	−2.65	0.64	0.63
6.0	9.0	1.85	2.69	3.09	−2.96	0.25	0.61
6.0	15.0	1.85	2.62	3.56	−3.50	0.31	2.12
7.0	5.0	1.37	1.84	2.20	130.37	18.65	21.57
7.0	7.0	1.78	2.70	2.80	0.52	1.69	0.80
7.0	8.0	1.83	2.70	2.96	−1.40	0.68	0.53
7.0	9.0	1.85	2.69	3.09	−1.85	0.29	0.52
7.0	15.0	1.85	2.62	3.56	−2.36	0.27	1.73
9.0	5.0	1.39	1.86	2.20	128.25	18.65	22.21
9.0	7.0	1.78	2.70	2.80	2.23	1.67	0.72
9.0	8.0	1.83	2.70	2.96	−0.01	0.71	0.42
9.0	9.0	1.85	2.69	3.09	−0.63	0.33	0.41
9.0	15.0	1.85	2.62	3.56	−1.12	0.34	0.72

Table 5.6: Principle g-factors g_1, g_2 and g_3, as well as the isotropic exchange J_{iso} and the magnitude of the DMI $||\underline{\underline{D}}||_2$ and Kitaev-interaction $||\underline{\underline{K}}||_2$ calculated for varying set of parameters U_{H} and Δ_{CT} for CuΔ.

(a) View along a-axis

(b) View along c-axis

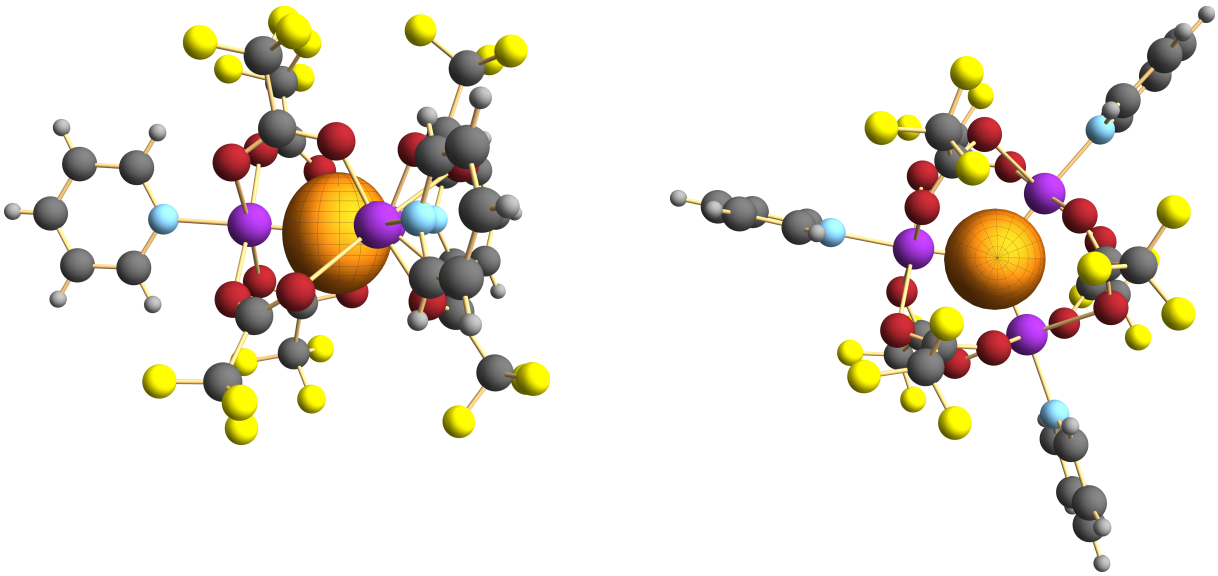


Figure 5.17: Contour plot illustrating the total g-tensor of CuΔ, as calculated with the parameters $U_H = 6\,eV$ and $\Delta_{CT} = 9\,eV$. The distance of the contour to μ_3-Fis proportional to the g-factor along that axis. CuΔ (a) viewed along the a-axis and (b) viewed along the c-axis.

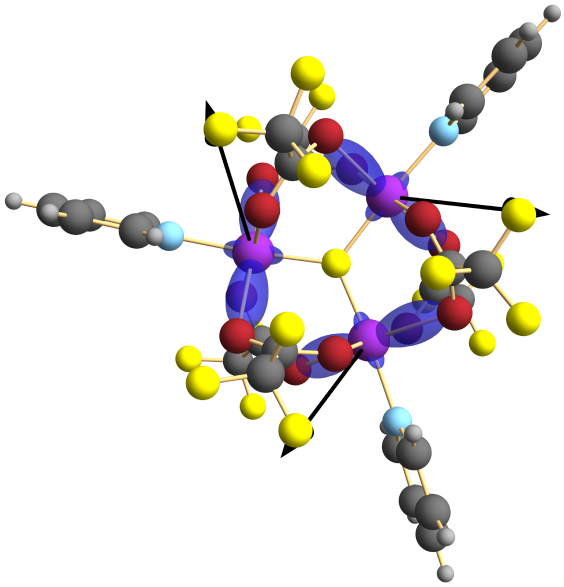


Figure 5.18: Hole density and classical representation of the local copper spin $\langle \vec{S}_i \rangle|_{i=0,1,2}$ superimposed over the molecular structure of CuΔ. The hole density is depicted as colored lobes, with blue representing spin up with respect to the c-axis. The spin expectation values are plotted as black arrows. The calculation was performed using $U_H = 6\,eV$ and $\Delta_{CT} = 9\,eV$. Additionally a small magnetic field of strength $B = 1\,mT$ was applied along the c-axis to lift the spin-degeneracy as zero field.

5.5 Conclusion

A significant issue of the kind of one-shot methods presented in this work is that their foundation is formed by some sort of mean-field calculation, for example DFT or Hatree-Fock, which have notorious difficulties accurately predicting properties of a correlated system, as shown in this thesis. Therefore some of the issues of the DFT calculation are carried over to the many-body calculations, such as the over-delocalization caused by the self-interaction error present in DFT. However these can be corrected to some extend.

A first step to improve the calculations on CuΔ quantitatively is to implement a corrected version of the self-interaction correction given in equation 5.25. This could not already be done due to time constraints, but this represents a simple, inexpensive improvement on the numerical accuracy of the calculations. The step is to improve the initial DFT-calculation itself, by for example employing the DFT+U method, where the inclusion of a mean-field Hubbard U counteracts the underestimated localization of electrons caused by the self-interaction error in standalone DFT [91]. The Hubbard U parameter for the DFT+U calculation can be estimated, for example, by means of linear-response constrained DFT [91] or density-functional perturbation theory [92, 93]. This allows for improvements of the performance of DFT for correlated electrons without introducing another empirical parameter. It could also prove beneficial to condition the DFT results obtained by *ORCA* with regards to the symmetries present in CuΔ , like the C_3 principal axis running along the c-axis through the central fluorine. This would entail symmetrizing the *ORCA*-Hamiltonian after the SCF-loop has concluded.

A simple and commonly used alternative method for the calculation of magnetic properties is broken symmetry-DFT (BS-DFT) [70], which was previously discussed in section 5.1.2. There it was shown that this method, using pure DFT, is insufficient for the description of the exchange coupling in CuΔ. This qualitative failure stems from the same errors already discussed for DFT, like the self-interaction error and the fact that spin is not a good quantum number, due to the single Slater-determinant nature of DFT. Adding the Hubbard U correction improves this scheme and allows for the description of the ordered ground state of Mott/Charge-transfer insulators, such as Cu_4O_3 and CuO [94]. However other copper derivatives such as Cu_2O can only be described poorly by DFT+U as well as the correlations themselves.

One of the most prevalent and successful methods for describing electronic and magnetic properties for correlated systems is the CASSCF[21] method [95]. In CASSCF the orbitals are divided into internal orbitals which will be fully occupied, virtual orbitals that will remain empty and the active space. CASSCF is a multi-refrence method with Slater-determinants being constructed from the active space, which is partially filled [95, 60]. This allows for the treatment of static correlations within the active space. The main disadvantage is the limited size of possible active spaces, which is restricted to the order of 10-15 orbitals [95, 60] or one million determinants. All copper 3d shells on CuΔ could therefore principally be treated with CASSCF, but for CoΔ there are around 14 million determinants needed for the d shells alone, which is not easily traceable using CASSCF. Here one-shot methods, as the one described in this thesis, have a clear advantage, as they do not rely on a self-consistency loop, like CASSCF for example. Due to the rigid separation of orbitals into different spaces, additional steps need to be taken to describe, for example charge transfer excitations. Therefore CASSCF calculations are usually used to construct optimized orbitals, which are to be used as starting points for other methods, such as CI[22], CC[23] or perturbation calculation [95]. Another difference is on one hand the lack of free parameters in a CASSCF

[21] Complete-active-space-self-consistent-field
[22] Configuration-interaction
[23] Coupled-cluster

calculation, but on the other hand CASSCF calculations are very sensitive to the chosen active space [60, 66]. Multireference methods, such as CASSCF, are needed to obtain quantitatively good results for properties like g-factors for copper derivatives containing more than two interacting sites, as illustrated on the example of multicopper oxidases by *Vancoillie, et al* [96]. In general there is no straight forward recipe for electronic/magnetic calculations for transition metal complexes and the chosen method and settings need to reflect the system and desired properties at hand [96].

Chapter 6

Summary

In the present work, the magnetic properties of the two novel molecular magnets CoΔ[1] [23] and CuΔ[2] [22, 46] were investigated by means of isothermal magnetization [48], static susceptibility [48] and electron-spin-resonance measurements. For $NMe_4[Cu_3(\mu_3\text{-F})(TFA)_6(Py)_3]$ the post-DFT multiplet ligand-field theory method was employed to qualitatively reproduce the experimental data, as well as to show the influence of correlations on the super-exchange path between the transition metal ions via the bridging μ_3-fluorine.

For CoΔ the static susceptibility $\chi = \frac{M(B=\text{const},T)}{B}$ [48] indicates dominant antiferromagnetic spin-spin interactions, which is supported by the isothmermal magnetization curves at low temperatures ($t \lesssim 10\,\text{K}$) exhibiting step-like features. The derivative of $M(B, T = \text{const})$ has a maximum at $B_c \approx 8.3\,\text{T}$, implying that the molecule's groundstate transitions at roughly B_c to a higher spin state as Bincreases. A spin-Hamiltonian including single-ion anisotropy and isotropic exchange interaction yields an antiferromagnetic coupling of $J = 92.0(1.2)\,\text{GHz}$, as well as an axial g-factor of $g_{||} = 2.400(16)$ and a planar g-factor of $g_\perp = 2.117(12)$. High-field/high-frequency electron spin resonance measurements at $T = 10\,\text{K}$ reveal a plethora of, namely 8, resonance branches. These experience some bending in the field range around B_c and change their nature for increasing B. From two groundstate transitions at frequencies $\nu = 75.9\,\text{GHz}$ and $\nu = 312.8\,\text{GHz}$ increases their number to six at $\nu = 522.0\,\text{GHz}$. This behavior is attributed to the suspected change of groundstates in the vicinity of B_c. The effective g-factors of the observed resonance branches are of the order of $g_{\text{eff}} \approx 4$ hinting that forbidden transitions were observed.

For CuΔ room temperature X-band ESR spectrum was recorded and a spin Hamiltonian, corresponding to a single copper ion with axial anisotropy, was fitted to the spectrum. This yielded an axial g-factor of $g_{||} = 2.3181(13)$ and a planar g-factor of $g_\perp = 2.065(7)$, as well as the hyperfine couplings $A_{||} = -495(5)\,\text{MHz}$ and $54(3)\,\text{MHz}$. There was an additional feature observed at an effective g-factor of $g_{\text{eff}} = 4.4$ whose origin could not be found. The static susceptibility curves [48] indicate the presence of ferromagnetic isotropic exchange between the spins on the copper ions. However both χT and the isothermal magnetization show significant contributions from anisotropic exchange interactions, such as the Dzyaloshinskii-Moriya and Kitaev-interactions. This conclusion is drawn from the fact that χT peaks before approaching a constant value for $T \nearrow 300\,\text{K}$ and that the slope of $M(B, T = \text{const})$ is lower than would be expected for free spins. Fitting of an spin-Hamiltonian, whose symmetry was fixed by the *ab-initio* calculations, yielded a ferromagnetic isotropic exchange of $J_{\text{iso}} = -6.24(16)\,\text{K}$ and magnitudes for DMI and Kitaev-interaction of $||\underline{\underline{D}}||_2 = 4.5(4)\,\text{K}$ and $||\underline{\underline{K}}||_2 = 25.3(4)\,\text{K}$. The Kitaev-interaction is

[1] $NMe_4[Co_3(\mu_3\text{-F})(TFA)_6(Py)_3]$
[2] $NMe_4[Cu_3(\mu_3\text{-F})(TFA)_6(Py)_3]$

therefore approximately four times stronger than the isotropic exchange, elucidating the low slope of the isothermal magnetization curve, as well as the peak observed in χT. Using loose powder high-field/high-frequency ESR measurements six resonance branches were observed at $T = 2\,\mathrm{K}$. Three of these branches exhibit a significant decrease in their slope around $B \approx 5\,\mathrm{T}$. This was attributed to mixing between the final states of the transitions giving rise to the resonance features and states from the two antiferromagnetically coupled doublets. Two of the observed six resonance branches were attributed to a misalignment the kernels.

Broken symmetry density functional calculations yielded strong antiferromagnetic coupling for CuΔ, contrary to the observations, showing the insufficiency of DFT when treating open-shell transition metals. Standalone DFT calculations were performed for several common functional of LDA, GGA, meta-GGA and hybrid type using *ORCA* [60]. As expected was the HOMO-LUMO gap largest for the hybrid-meta-GGA functional TPSSh [64]. This DFT calculation was used as basis for many-body multiplet ligand field theory calculations. For this the DFT tight-binding Hamiltonian was rotated to basis of copper 3d, μ_3-F2s, 2p shells. The ligand shells were construed by block-band diagonalization of the DFT-Hamiltonian. The local Coulomb-interaction was expressed in terms of Slater-integrals, which were calculated using *FPLO* [75, 76] and *quanty* using the PWLDA92 functional. The Hubbard U_H was introduced as a free parameter to account for screening effects caused by the surrounding electrons. Charge-transfer excitations were implemented and characterized by the charge-transfer energy Δ_SH. Using this model full many-body calculations of the lowest lying spin-multiplet were conducted using *quanty* [77]. These revealed, that for the Cu-μ_3-F-Cu super-exchange path to be ferromagnetic, Coulomb-scattering and correlations are required on the μ_3-bridging fluorine. Turning these off yields strong antiferromagnetic coupling similar to the BS-DFT calculations. Varying the free parameters it was shown that increasing U_H stabilizes the low-spin eigenstates while increasing the charge-transfer energy stabilizes the high-spin states. The influence of U_H is contrary to what would be expected by the GKA-rules, suggesting that the inclusion of a third ion to the super-exchange path changes the simple picture assumed in the GKA-rules significantly. Features of the experimental data, such as the peak in χT and the change in slope of the ESR resonance branches could be reproduced qualitatively for $U_\mathrm{H} = 6\,\mathrm{eV}$ and $\Delta_\mathrm{CT} = 9\,\mathrm{eV}$. But no quantitative agreement with the experimental data could be achieved. This is most notable in the overestimation of g-factors and underestimation of anisotropic exchange with respect to the isotropic exchange. The lack of quantitative agreement can, at least, partially be attributed to the missing self-interaction correction, which could not yet be implemented successfully, due to an error in the code. It is additionally suggested, that improving the initial DFT calculation, by for example performing a DFT+U calculation, could improve the results as well.

Appendix A

Appendix

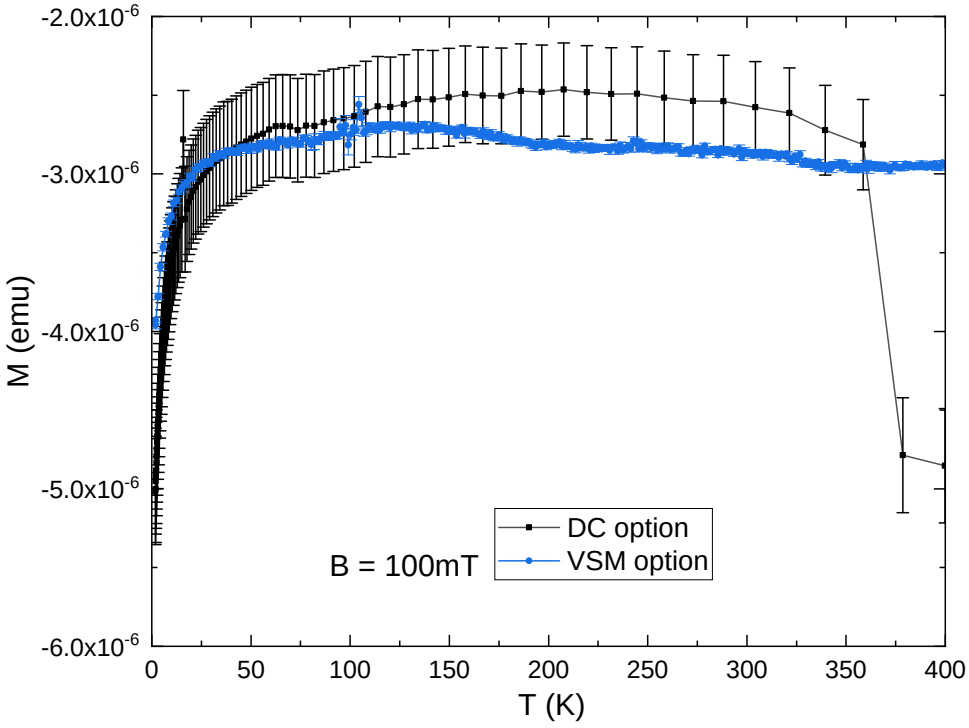


Figure A.1: Magnetization M at $B = 100\text{mT}$ vs temperature of an empty sample holder used for the MPMS measurements of CuΔ. Both DC and VSM options were used (see section 2.1). The measurement was performed by *A. Elghandour* [48].

Resonance feature	Lower limit (T)	Upper limit (T)
$\nu = 75.9\,\mathrm{GHz}$		
A	1.5954	1.9464
B	0.3542	0.5680
C	0.8122	1.0271
D	1.1190	1.2806
E	1.3520	1.4866
$\nu = 312.8\,\mathrm{GHz}$		
A	2.6689	3.1700
B	3.3918	3.8656
C	4.3000	4.4533
D	4.4533	5.0000
E	5.0940	5.6423
F	6.3894	7.0956

Table A.1: Integration limits for the determination of the intensities of the resonance features for the temperature sweeps at $\nu = 75.9\,\mathrm{GHz}$ and $\nu = 312.8\,\mathrm{GHz}$ for CoΔ.

Resonance feature	Lower limit (T)	Upper limit (T)
$\nu = 102.2\,\mathrm{GHz}$		
A	1.7110	1.8604
B	1.9802	2.0520
C	2.1512	2.2411
D	2.3492	2.4677
$\nu = 228.4\,\mathrm{GHz}$		
A	5.2517	5.3606
B	5.3610	5.5000
C	5.5651	5.7090
D	5.7593	5.8849
E	7.0236	7.1860
h_1	5.8100	6.1600
h_2	6.8366	7.1061
h_3	7.1410	7.3727
h_4	7.8170	8.1956

Table A.2: Integration limits for the determination of the intensities of the resonance features for the temperature sweeps at $\nu = 102.2\,\mathrm{GHz}$ and $\nu = 228.4\,\mathrm{GHz}$ for CuΔ.

Bibliography

[1] D. Gatteschi, R. Sessoli, and J. Villain, *Molecular nanomagnets*, vol. 5. Oxford University Press on Demand, 2006.

[2] J. J. Croat, J. F. Herbst, R. W. Lee, and F. E. Pinkerton, "High-energy product Nd-Fe-B permanent magnets," *Applied Physics Letters*, vol. 44, pp. 148–149, 01 1984.

[3] M. Holynska, *Single-molecule magnets: molecular architectures and building blocks for spintronics*. John Wiley & Sons, 2019.

[4] J. D. Widmer, R. Martin, and M. Kimiabeigi, "Electric vehicle traction motors without rare earth magnets," *Sustainable Materials and Technologies*, vol. 3, pp. 7–13, 2015.

[5] C. Gong, L. Li, Z. Li, H. Ji, A. Stern, Y. Xia, T. Cao, W. Bao, C. Wang, Y. Wang, *et al.*, "Discovery of intrinsic ferromagnetism in two-dimensional van der Waals crystals," *Nature*, vol. 546, no. 7657, pp. 265–269, 2017.

[6] J.-U. Lee, S. Lee, J. H. Ryoo, S. Kang, T. Y. Kim, P. Kim, C.-H. Park, J.-G. Park, and H. Cheong, "Ising-type magnetic ordering in atomically thin $FePS_3$," *Nano letters*, vol. 16, no. 12, pp. 7433–7438, 2016.

[7] M. Liu, Z. Ouyang, X. Liu, J. Cao, T. Xiao, Z. Xia, and Z. Wang, "Structure and Magnetism of an Ideal One-Dimensional Chain Antiferromagnet $[C_2NH_8]_3[Fe(SO_4)_3]$ with a Large Spin of S= 5/2," *Inorganic Chemistry*, vol. 61, no. 38, pp. 15045–15050, 2022.

[8] D. L. Quintero-Castro, G. J. Nilsen, K. Meier-Kirchner, A. Benitez-Castro, G. Guenther, T. Sakakibara, M. Tokunaga, C. Agu, I. Mandal, and A. A. Tsirlin, "One-dimensional magnetism in synthetic Paufferite, $\beta-VOSO_4$," *Phys. Rev. Mater.*, vol. 7, p. 045003, Apr 2023.

[9] T. Lis, "Preparation, structure, and magnetic properties of a dodecanuclear mixed-valence manganese carboxylate," *Acta Crystallographica Section B: Structural Crystallography and Crystal Chemistry*, vol. 36, no. 9, pp. 2042–2046, 1980.

[10] L. Mathivathanan, G. Rogez, N. Ben Amor, V. Robert, R. G. Raptis, and A. K. Boudalis, "Origin of Ferromagnetism and Magnetic Anisotropy in a Family of Copper(II) Triangles," *Chemistry - A European Journal*, vol. 26, no. 56, pp. 12769–12784, 2020.

[11] R. H. Holm and E. I. Solomon, "Preface: Biomimetic Inorganic Chemistry," *Chemical Reviews*, vol. 104, no. 2, pp. 347–348, 2004. PMID: 14871127.

[12] R. H. Holm, P. Kennepohl, and E. I. Solomon, "Structural and Functional Aspects of Metal Sites in Biology," *Chemical Reviews*, vol. 96, no. 7, pp. 2239–2314, 1996. PMID: 11848828.

[13] E. I. Solomon, P. Chen, M. Metz, S.-K. Lee, and A. E. Palmer, "Oxygen Binding, Activation, and Reduction to Water by Copper Proteins," *Angewandte Chemie International Edition*, vol. 40, no. 24, pp. 4570–4590, 2001.

[14] M. Trif, F. Troiani, D. Stepanenko, and D. Loss, "Spin-Electric Coupling in Molecular Magnets," *Phys. Rev. Lett.*, vol. 101, p. 217201, Nov 2008.

[15] M. Trif, F. Troiani, D. Stepanenko, and D. Loss, "Spin electric effects in molecular antiferromagnets," *Phys. Rev. B*, vol. 82, p. 045429, Jul 2010.

[16] A. K. Boudalis, J. Robert, and P. Turek, "First Demonstration of Magnetoelectric Coupling in a Polynuclear Molecular Nanomagnet: Single-Crystal EPR Studies of $[Fe_3O(O_2CPh)_6(py)_3]ClO_4{\cdot}py$ under Static Electric Fields," *Chemistry - A European Journal*, vol. 24, no. 56, pp. 14896–14900, 2018.

[17] F. Troiani, D. Stepanenko, and D. Loss, "Hyperfine-induced decoherence in triangular spin-cluster qubits," *Phys. Rev. B*, vol. 86, p. 161409, Oct 2012.

[18] B. Kintzel, M. Böhme, J. Liu, A. Burkhardt, J. Mrozek, A. Buchholz, A. Ardavan, and W. Plass, "Molecular electronic spin qubits from a spin-frustrated trinuclear copper complex," *Chemical communications*, vol. 54, no. 92, pp. 12934–12937, 2018.

[19] O. Kahn, "Competing spin interactions and degenerate frustration for discrete molecular species," *Chemical Physics Letters*, vol. 265, no. 1, pp. 109–114, 1997.

[20] J. Schnack, "Effects of frustration on magnetic molecules: a survey from Olivier Kahn until today," *Dalton Trans.*, vol. 39, pp. 4677–4686, 2010.

[21] M.-A. Bouammali, N. Suaud, N. Guihéry, and R. Maurice, "Antisymmetric exchange in a real copper triangular complex," *Inorganic Chemistry*, vol. 61, no. 31, pp. 12138–12148, 2022.

[22] A. Vassiliev *et al.*, "private communication," 2022.

[23] D. Kayumova, D. Tereshchenko, T. Shatalova, E. Lermontova, A. Boltalin, I. Morozov, I. Malkerova, and A. Alikhanyan, "Thermal Behavior of the Heteroligand (mu3-Fluoro)hexakis(mu2-trifluoroacetato)tris(pyridine)tricobaltate(II) Tetramethylammonium Complex $(NMe_4)[Co_3F(TFA)_6(Py)_3]$," *Russian Journal of Coordination Chemistry*, vol. 48, pp. 870–876, 12 2022.

[24] G. E. Pake, T. L. Estle, G. E. Pake, and T. L. Estle, *The physical principles of electron paramagnetic resonance*. Frontiers in physics, Reading, Mass. [u.a.]: Benjamin, 2. ed., completely rev., enl., and reset ed., 1973. First ed. published in 1962 under title: Paramagnetic resonance ; Includes bibliographical references.

[25] M. W. Haverkort, M. Zwierzycki, and O. K. Andersen, "Multiplet ligand-field theory using Wannier orbitals," *Phys. Rev. B*, vol. 85, p. 165113, Apr 2012.

[26] G. A. Bain and J. F. Berry, "Diamagnetic Corrections and Pascal's Constants," *Journal of chemical education*, vol. 85, no. 4, p. 532, 2008.

[27] M. Jonák, *Low-energy magnetic excitations and magnetisation in magnetoelectric antiferromagnets $MnTiO_3$ and $LiMnPO_4$ and in van-der-Waals ferromagnet CrI_3*. 2022.

[28] L. Spillecke, *High-frequency/high-field electron paramagnetic resonance investigations on metal-organic molecular compounds*. 2021. Dissertation enthält 1 Zeitschriftenaufsätzen.

[29] K. A. Earle, D. E. Budil, and J. H. Freed, "250-GHz EPR of nitroxides in the slow-motional regime: models of rotational diffusion," *Journal of physical chemistry (1952)*, vol. 97, no. 50, pp. 13289–13297, 1993.

[30] J. V. Paulin, A. Batagin-Neto, B. Naydenov, K. Lips, and C. F. O. Graeff, "High-field/high-frequency EPR spectroscopy on synthetic melanin: on the origin of carbon-centered radicals," *Mater. Adv.*, vol. 2, pp. 6297–6305, 2021.

[31] S. Koseki, N. Matsunaga, T. Asada, M. W. Schmidt, and M. S. Gordon, "Spin-Orbit Coupling Constants in Atoms and Ions of Transition Elements: Comparison of Effective Core Potentials, Model Core Potentials, and All-Electron Methods," *The journal of physical chemistry. A, Molecules, spectroscopy, kinetics, environment, and general theory*, vol. 123, no. 12, pp. 2325–2339, 2019.

[32] M. H. L. Pryce, "A Modified Perturbation Procedure for a Problem in Paramagnetism," *Proceedings of the Physical Society. Section A*, vol. 63, p. 25, jan 1950.

[33] X. Li, H. Yu, F. Lou, J. Feng, M.-H. Whangbo, and H. Xiang, "Spin Hamiltonians in Magnets: Theories and Computations," *Molecules*, vol. 26, no. 4, 2021.

[34] T. Moriya, "Anisotropic Superexchange Interaction and Weak Ferromagnetism," *Phys. Rev.*, vol. 120, pp. 91–98, Oct 1960.

[35] Y. Fujishiro, N. Kanazawa, and Y. Tokura, "Engineering skyrmions and emergent monopoles in topological spin crystals," *Applied Physics Letters*, vol. 116, no. 9, p. 090501, 2020.

[36] C. Rudowicz, "ChemInform Abstract: Higher-order Field-dependent Terms in Spin Hamiltonians for Transition Ions - Implications for High-magnetic Field and High-frequency EMR Measurements," *ChemInform*, vol. 45, 11 2014.

[37] C. Bloch, "Sur la théorie des perturbations des états liés," *Nuclear Physics*, vol. 6, pp. 329–347, 1958.

[38] L. F. Chibotaru and L. Ungur, "Ab initio calculation of anisotropic magnetic properties of complexes. I. Unique definition of pseudospin Hamiltonians and their derivation," *The Journal of Chemical Physics*, vol. 137, no. 6, p. 064112, 2012.

[39] G. H. Wannier, "Dynamics of band electrons in electric and magnetic fields," *Rev. Mod. Phys.*, vol. 34, pp. 645–655, Oct 1962.

[40] W. Kohn, "Analytic properties of bloch waves and wannier functions," *Phys. Rev.*, vol. 115, pp. 809–821, Aug 1959.

[41] D. Šabani, C. Bacaksiz, and M. V. Milošević, "Ab initio methodology for magnetic exchange parameters: Generic four-state energy mapping onto a Heisenberg spin Hamiltonian," *Phys. Rev. B*, vol. 102, p. 014457, Jul 2020.

[42] P. Hohenberg and W. Kohn, "Inhomogeneous Electron Gas," *Phys. Rev.*, vol. 136, pp. B864–B871, Nov 1964.

[43] W. Kohn and L. J. Sham, "Self-Consistent Equations Including Exchange and Correlation Effects," *Phys. Rev.*, vol. 140, pp. A1133–A1138, Nov 1965.

[44] F. Neese, "Prediction of molecular properties and molecular spectroscopy with density functional theory: From fundamental theory to exchange-coupling," *Coordination chemistry reviews*, vol. 253, no. 5, pp. 526–563, 2009.

[45] E. Pavarini, *The LDA+DMFT approach to strongly correlated materials : lecture notes of the autumn school 2011, hands-on LDA+DMFT ; autumn school organized by the DFG research unit 1346 dynamical mean-field approach with predictive power for strongly correlated materials at Forschungszentrum Jülich 4-7 October 2011.* Schriften des Forschungszentrums Jülich. Reihe modeling and simulation ;, Jülich: Forschungszentrum, Zentralbibliothek, 2011. englisch.

[46] I. V. Morozov, "private communication," 2022.

[47] C. F. Macrae, I. J. Bruno, J. A. Chisholm, P. R. Edgington, P. McCabe, E. Pidcock, L. Rodriguez-Monge, R. Taylor, J. van de Streek, and P. A. Wood, "*Mercury CSD 2.0* – new features for the visualization and investigation of crystal structures," *Journal of Applied Crystallography*, vol. 41, pp. 466–470, Apr 2008.

[48] A. Elghandour, "Static magnteization and susceptibility measurements on $NMe_4[Co_3(\mu_3\text{-}F)(TFA)_6(Py)_3]$ and $NMe_4[Cu_3(\mu_3\text{-}F)(TFA)_6(Py)_3]$: private communication," 2022.

[49] S. Siebeneichler, K. V. Dorn, A. Ovchinnikov, W. Papawassiliou, I. da Silva, V. Smetana, A. J. Pell, and A.-V. Mudring, "Frustration and 120Â° Magnetic Ordering in the Layered Triangular Antiferromagnets $AFe(PO_3F)_2$ (A = K, $(NH_4)_2Cl$, NH_4, Rb, and Cs)," *Chemistry of Materials*, vol. 34, no. 17, pp. 7982–7994, 2022.

[50] L. E. Svistov, A. I. Smirnov, L. A. Prozorova, O. A. Petrenko, A. Micheler, N. Büttgen, A. Y. Shapiro, and L. N. Demianets, "Magnetic phase diagram, critical behavior, and two-dimensional to three-dimensional crossover in the triangular lattice antiferromagnet $RbFe(MoO_4)_2$," *Phys. Rev. B*, vol. 74, p. 024412, Jul 2006.

[51] S. Blundell, *Magnetism in condensed matter.* Oxford master series in condensed matter physics, Oxford ; New York: Oxford University Press, 2001. Includes bibliographical references and index. - Description based on print version record.

[52] J. Krzystek, A. Ozarowski, and J. Telser, "Multi-frequency, high-field EPR as a powerful tool to accurately determine zero-field splitting in high-spin transition metal coordination complexes," *Coordination Chemistry Reviews*, vol. 250, no. 17, pp. 2308–2324, 2006. 20th International Conference on Coordination and Bioinorganic Chemistry.

[53] S. Stoll and A. Schweiger, "EasySpin, a comprehensive software package for spectral simulation and analysis in EPR," *Journal of Magnetic Resonance*, vol. 178, no. 1, pp. 42–55, 2006.

[54] P. Virtanen, R. Gommers, T. E. Oliphant, M. Haberland, T. Reddy, D. Cournapeau, E. Burovski, P. Peterson, W. Weckesser, J. Bright, S. J. van der Walt, M. Brett, J. Wilson, K. J. Millman, N. Mayorov, A. R. J. Nelson, E. Jones, R. Kern, E. Larson, C. J. Carey, İ. Polat, Y. Feng, E. W. Moore, J. VanderPlas, D. Laxalde, J. Perktold, R. Cimrman, I. Henriksen, E. A. Quintero, C. R. Harris, A. M. Archibald, A. H. Ribeiro, F. Pedregosa, P. van Mulbregt, and SciPy 1.0 Contributors, "SciPy 1.0: Fundamental Algorithms for Scientific Computing in Python," *Nature Methods*, vol. 17, pp. 261–272, 2020.

[55] R. Andrae, T. Schulze-Hartung, and P. Melchior, "Dos and don'ts of reduced chi-squared," 2010.

[56] C. R. Harris, K. J. Millman, S. J. van der Walt, R. Gommers, P. Virtanen, D. Cournapeau, E. Wieser, J. Taylor, S. Berg, N. J. Smith, R. Kern, M. Picus, S. Hoyer, M. H. van Kerkwijk, M. Brett, A. Haldane, J. F. del Río, M. Wiebe, P. Peterson, P. Gérard-Marchant, K. Sheppard, T. Reddy, W. Weckesser, H. Abbasi, C. Gohlke, and T. E. Oliphant, "Array programming with NumPy," *Nature*, vol. 585, pp. 357–362, Sept. 2020.

[57] W.-L. Feng, "Theoretical Investigation of the g Factors for Copper (II) Ion in an Orthorhombic Crystal and its Application to $(CuCl_4)^{2-}$ Cluster," *Zeitschrift für Naturforschung A*, vol. 65, no. 3, pp. 251–262, 2010.

[58] W. B. Lewis, J. Alei, Mohammed, and L. O. Morgan, "Magnetic Resonance Studies on Copper(II) Complex Ions in Solution. I. Temperature Dependences of the 17O NMR and Copper(II) EPR Linewidths of $Cu(H_2O)_6^{2+}$," *The Journal of Chemical Physics*, vol. 44, pp. 2409–2417, 05 2004.

[59] S. Ferrer, F. Lloret, E. Pardo, J. M. Clemente-Juan, M. Liu-GonzÃ¡lez, and S. GarcÃa-Granda, "Antisymmetric Exchange in Triangular Tricopper(II) Complexes: Correlation among Structural, Magnetic, and Electron Paramagnetic Resonance Parameters," *Inorganic Chemistry*, vol. 51, no. 2, pp. 985–1001, 2012. PMID: 22220521.

[60] F. Neese, "The ORCA program system," *WIREs Computational Molecular Science*, vol. 2, no. 1, pp. 73–78, 2012.

[61] J. P. Perdew and Y. Wang, "Accurate and simple analytic representation of the electron-gas correlation energy," *Phys. Rev. B*, vol. 45, pp. 13244–13249, Jun 1992.

[62] A. D. Becke, "Density-functional exchange-energy approximation with correct asymptotic behavior," *Phys. Rev. A*, vol. 38, pp. 3098–3100, Sep 1988.

[63] J. Tao, J. P. Perdew, V. N. Staroverov, and G. E. Scuseria, "Climbing the Density Functional Ladder: Nonempirical Meta–Generalized Gradient Approximation Designed for Molecules and Solids," *Phys. Rev. Lett.*, vol. 91, p. 146401, Sep 2003.

[64] V. N. Staroverov, G. E. Scuseria, J. Tao, and J. P. Perdew, "Comparative assessment of a new nonempirical density functional: Molecules and hydrogen-bonded complexes," *The Journal of Chemical Physics*, vol. 119, pp. 12129–12137, 12 2003.

[65] C. C. J. Roothaan, "Self-Consistent Field Theory for Open Shells of Electronic Systems," *Rev. Mod. Phys.*, vol. 32, pp. 179–185, Apr 1960.

[66] F. Neese, F. Wennmohs, *et al.*, *ORCA - An ab initio, DFT and semiempirical SCF-MO package - Manual for version 5.0.3.* Max-Planck-Institut für Kohlenforschung, 2022.

[67] G. Zhang and C. B. Musgrave, "Comparison of DFT Methods for Molecular Orbital Eigenvalue Calculations," *The Journal of Physical Chemistry A*, vol. 111, no. 8, pp. 1554–1561, 2007. PMID: 17279730.

[68] F. Weigend and R. Ahlrichs, "Balanced basis sets of split valence, triple zeta valence and quadruple zeta valence quality for H to Rn: Design and assessment of accuracy," *Phys. Chem. Chem. Phys.*, vol. 7, pp. 3297–3305, 2005.

[69] F. Neese and E. F. Valeev, "Revisiting the Atomic Natural Orbital Approach for Basis Sets: Robust Systematic Basis Sets for Explicitly Correlated and Conventional Correlated ab initio Methods," *Journal of Chemical Theory and Computation*, vol. 7, no. 1, pp. 33–43, 2011. PMID: 26606216.

[70] C. van Wüllen, "Broken Symmetry Approach to Density Functional Calculation of Magnetic Anisotropy or Zero Field Splittings for Multinuclear Complexes with Antiferromagnetic Coupling," *The Journal of Physical Chemistry A*, vol. 113, no. 43, pp. 11535–11540, 2009. PMID: 19708660.

[71] B. C. Carlson and J. M. Keller, "Orthogonalization Procedures and the Localization of Wannier Functions," *Phys. Rev.*, vol. 105, pp. 102–103, Jan 1957.

[72] I. Mayer, "On Löwdin's method of symmetric orthogonalization*," *International Journal of Quantum Chemistry*, vol. 90, no. 1, pp. 63–65, 2002.

[73] E. Schmidt, "Zur Theorie der linearen und nichtlinearen Integralgleichungen," *Mathematische Annalen*, vol. 63, no. 4, pp. 433–476, 1907.

[74] A. Shestakov, "Compact formula for Coulomb integrals of Slater orbitals," *Journal of Structural Chemistry*, vol. 33, no. 1, pp. 131–133, 1992.

[75] K. Koepernik and H. Eschrig, "Full-potential nonorthogonal local-orbital minimum-basis band-structure scheme," *Physical Review B*, vol. 59, no. 3, p. 1743, 1999.

[76] M. Richter, K. Koepernik, and H. Eschrig, "Full-potential local-orbital approach to the electronic structure of solids and molecules," in *Condensed Matter Physics In The Prime Of The 21st Century: Phenomena, Materials, Ideas, Methods*, pp. 271–291, World Scientific, 2008.

[77] Y. Lu, M. Höppner, O. Gunnarsson, and M. W. Haverkort, "Efficient real-frequency solver for dynamical mean-field theory," *Phys. Rev. B*, vol. 90, p. 085102, Aug 2014.

[78] J. Zaanen, G. A. Sawatzky, and J. W. Allen, "Band gaps and electronic structure of transition-metal compounds," *Phys. Rev. Lett.*, vol. 55, pp. 418–421, Jul 1985.

[79] A. Bocquet, T. Mizokawa, T. Saitoh, H. Namatame, and A. Fujimori, "Electronic structure of 3d-transition-metal compounds by analysis of the 2p core-level photoemission spectra," *Physical Review B*, vol. 46, no. 7, p. 3771, 1992.

[80] "Theory of Spin-Orbit Coupling in Atoms. II. Comparison of Theory with Experiment," *Proceedings of the Royal Society of London. Series A, Mathematical and Physical Sciences*, vol. 271, no. 1347, pp. 565–578, 1963.

[81] J. P. Perdew and A. Zunger, "Self-interaction correction to density-functional approximations for many-electron systems," *Phys. Rev. B*, vol. 23, pp. 5048–5079, May 1981.

[82] T. Tsuneda and K. Hirao, "Self-interaction corrections in density functional theory," *The Journal of Chemical Physics*, vol. 140, 03 2014. 18A513.

[83] J. B. Goodenough, "Theory of the Role of Covalence in the Perovskite-Type Manganites [La, M(II)]MnO_3," *Phys. Rev.*, vol. 100, pp. 564–573, Oct 1955.

[84] J. B. Goodenough, "An interpretation of the magnetic properties of the perovskite-type mixed crystals $La_{1-x}Sr_xCoO_3$-Î»," *Journal of Physics and Chemistry of Solids*, vol. 6, no. 2, pp. 287–297, 1958.

[85] J. Kanamori, "Superexchange interaction and symmetry properties of electron orbitals," *Journal of Physics and Chemistry of Solids*, vol. 10, no. 2, pp. 87–98, 1959.

[86] P. W. Anderson, "New Approach to the Theory of Superexchange Interactions," *Phys. Rev.*, vol. 115, pp. 2–13, Jul 1959.

[87] E. Pavarini, E. Koch, F. Anders, and a. (eds, *Correlated Electrons: From Models to Materials*. 09 2012.

[88] Z. Liu, X. Li, W. Zhu, Z. F. Wang, and J. Yang, "Theoretical proposal and material realization of ferromagnetic negative charge-transfer energy insulator," *Phys. Rev. B*, vol. 107, p. 014413, Jan 2023.

[89] M.-C. Wang and C.-R. Chang, "Goodenough-Kanamori-Anderson Rules in $CrI_3/MoTe_2/CrI_3$ Van der Waals Heterostructure," *Journal of The Electrochemical Society*, vol. 169, p. 053507, may 2022.

[90] A. Teja and P. Y. Koh, "Synthesis, properties, and applications of magnetic iron oxide nanoparticles," *Prog. Cryst. Growth Charact. Mater.*, vol. 55, pp. 22–45, 03 2009.

[91] M. Cococcioni and S. de Gironcoli, "Linear response approach to the calculation of the effective interaction parameters in the LDA + U method," *Phys. Rev. B*, vol. 71, p. 035105, Jan 2005.

[92] I. Timrov, N. Marzari, and M. Cococcioni, "Hubbard parameters from density-functional perturbation theory," *Phys. Rev. B*, vol. 98, p. 085127, Aug 2018.

[93] I. Timrov, N. Marzari, and M. Cococcioni, "Self-consistent Hubbard parameters from density-functional perturbation theory in the ultrasoft and projector-augmented wave formulations," *Phys. Rev. B*, vol. 103, p. 045141, Jan 2021.

[94] A. Živković, A. Roldan, and N. H. de Leeuw, "Density functional theory study explaining the underperformance of copper oxides as photovoltaic absorbers," *Phys. Rev. B*, vol. 99, p. 035154, Jan 2019.

[95] J. Olsen, "The CASSCF method: A perspective and commentary," *International Journal of Quantum Chemistry*, vol. 111, no. 13, pp. 3267–3272, 2011.

[96] S. Vancoillie, J. Chalupský, U. Ryde, E. I. Solomon, K. Pierloot, F. Neese, and L. Rulíšek, "Multireference Ab Initio Calculations of g tensors for Trinuclear Copper Clusters in Multicopper Oxidases," *The journal of physical chemistry. B*, vol. 114, no. 22, pp. 7692–7702, 2010.

A Note of Gratitude

First and foremost, I would like to thank my two supervisors Prof. Dr. Rüdiger Klingeler and Prof. Dr. Maurits W. Haverkort for granting me the opportunity to embark on this cooperative project in their respective research groups. Both created a working environments, that were very friendly and a joy to work in. The scientific discussion always helped to deepen my understanding of this branch of physics and introduced me to interesting concepts.

Special thanks goes to Dr. Changhyun Koo for introducing me to the HF-ESR setup and guiding me through the somewhat new experience of actually performing a proper experiment, as well as for proofreading parts of my thesis. Discussions with him about my data were always very helpful and enlightening.

Thirdly I would like to thank the group members of F25 for their active group life, such as a daily 5 p.m. bakery brake with lots of entertaining (sometimes even interesting) conversations and the odd cake. I would like to highlight Dr. Martin Jonak for proving many kind words and very nice discussions about god and the universe. Also a note of gratitude goes to Jan and Lukas for providing plenty entertainment during every kind of brake and "volunteering" to proofread my thesis. I also want to acknowledge, that they more or less graciously accepted a stray theoretician among their ranks.

Huge thanks also goes to the members of Maurits' group for the nice lunch brakes at D'Vinos and more or less regular game nights of the last months. Special thanks goes to Kai and Martin. Kai introduced me to *rubber duck debugging* and played a very attentive duck from time to time. Martin always provided very useful insights into more technical aspects of, for example, *quanty*.

I would also love to give a huge shout out to my friends and family, who always managed to cheer me up when things looked dire and I needed a diversion. Firstly I want to give a note of gratitude to Corinna, Luise and Yulian for the very enjoyable coffee brakes and funny stories about other research groups. Secondly I want to acknowledge my comrades at the THW for their spirit and just being the best. Working and joking with you always recharged my batteries when I was feeling down and my motivation was waning. I'd like to highlight Christian and Steini, as well as Jason, Paul and Anne for their friendship and banter. Lastly I thank my family for their continuous support and love in this (sometimes) challenging time.

Erklärung

Ich versichere, dass ich diese Arbeit selbstständig verfasst und keine anderen als die angegebenen Quellen und Hilfsmittel benutzt habe.

Heidelberg, den 28.06.2023, ...

Unterschrift